

SUPERMASSIVE BLACK HOLES AND THEIR HOST SPHEROIDS. I. DISASSEMBLING GALAXIES

G. A. D. SAVORGNA AND A. W. GRAHAM

Centre for Astrophysics and Supercomputing, Swinburne University of Technology, Hawthorn, Victoria 3122, Australia; gsavorgn@astro.swin.edu.au

Received 2015 July 16; accepted 2015 November 19; published 2015 MM DD

ABSTRACT

Several recent studies have performed galaxy decompositions to investigate correlations between the black hole mass and various properties of the host spheroid, but they have not converged on the same conclusions. This is because their models for the same galaxy were often significantly different and not consistent with each other in terms of fitted components. Using 3.6 μm *Spitzer* imagery, which is a superb tracer of the stellar mass (superior to the *K band*), we have performed state-of-the-art multicomponent decompositions for 66 galaxies with directly measured black hole masses. Our sample is the largest to date and, unlike previous studies, contains a large number (17) of spiral galaxies with low black hole masses. We paid careful attention to the image mosaicking, sky subtraction, and masking of contaminating sources. After a scrupulous inspection of the galaxy photometry (through isophotal analysis and unsharp masking) and—for the first time—2D kinematics, we were able to account for spheroids; large-scale, intermediate-scale, and nuclear disks; bars; rings; spiral arms; halos; extended or unresolved nuclear sources; and partially depleted cores. For each individual galaxy, we compared our best-fit model with previous studies, explained the discrepancies, and identified the optimal decomposition. Moreover, we have independently performed one-dimensional (1D) and two-dimensional (2D) decompositions and concluded that, at least when modeling large, nearby galaxies, 1D techniques have more advantages than 2D techniques. Finally, we developed a prescription to estimate the uncertainties on the 1D best-fit parameters for the 66 spheroids that takes into account systematic errors, unlike popular 2D codes that only consider statistical errors.

Key words: black hole physics – galaxies: bulges – galaxies: elliptical and lenticular, cD – galaxies: evolution – galaxies: structure

1. INTRODUCTION

Supermassive black holes and their host spheroids¹ have very different sizes. If the event horizon of the Galactic supermassive black hole was as big as a grain of sand in the Sahara Desert, then the black hole's gravitational sphere of influence would be as big as the international airport of Cairo, and the Galactic bulge would be as big as the Sahara Desert itself. It is thus surprising that the masses of supermassive black holes (M_{BH}) scale with a number of properties of their host spheroid, indicating the nongravitational origin of these correlations (e.g., Dressler 1989; Yee 1992; Kormendy & Richstone 1995; Laor et al. 1997; Magorrian et al. 1998; Ferrarese & Merritt 2000; Gebhardt et al. 2000; Graham et al. 2001; Marconi & Hunt 2003; Häring & Rix 2004; Graham & Scott 2015).

The tightness of (i.e., the small scatter about) the above observed black hole mass correlations has led to the idea that black holes and host spheroids have coevolved with some sort of self-regulated growth. Exploring the evolution of this growth with cosmic time could help identify the driving mechanisms of the black hole–spheroid coevolution. Observations at $z = 0$ set the local benchmark from which to measure this evolution. Any complete theory or model describing the coevolution of spheroids and black holes must incorporate all of the observed scaling relations, which also have to be consistent with each other. Modern hydrodynamical simulations, such as EAGLE (Schaye et al. 2015), calibrate the feedback efficiencies to match the $z = 0$ black hole mass–galaxy mass relation. The observed scaling relations can also be employed to predict the

masses of black holes in other galaxies, where a direct measure of M_{BH} would be extremely time-consuming or simply impossible owing to technological limitations. Moreover, many accurate M_{BH} predictions enable one to derive the local black hole mass function (e.g., Salucci et al. 1999; Graham et al. 2007; Shankar 2009, 2013; Fontanot et al. 2015) and space density (e.g., Graham & Driver 2007b; Comastri et al. 2015). All of these examples depend on the $z = 0$ relations, and as such the recalibration of the black hole mass–spheroid stellar mass ratio ($M_{\text{BH}}/M_{*,\text{sph}}$) in large spheroids, from 0.1% to 0.2% (e.g., Marconi & Hunt 2003; Häring & Rix 2004) to 0.49% (Graham & Scott 2015), has many substantial implications.

Since the early stellar dynamical detections of black holes were carried out in the 1980s (see the references in the reviews by Kormendy & Richstone 1995; Richstone et al. 1998; Graham 2015 for pioneering papers), the number of (direct) black hole mass measurements has increased with time and it has recently become a statistically meaningful sample with which one can study SMBH demographics. It is now generally accepted that supermassive black holes reside at the center of most, if not all, massive spheroids, either quiescent or active.

Massive, early-type (E, E/S0, S0) galaxies are often composite systems. The knowledge that many “elliptical” (E) galaxies were misclassified and actually contain embedded stellar disks dates back at least three decades (Capaccioli 1987; Carter 1987; Bender 1990; Rix & White 1990, 1992; Scorz & Bender 1990, 1995; Nieto et al. 1991). After examining long-slit and integral field unit spectroscopic observations of morphologically classified elliptical galaxies in the Fornax Cluster, D’Onofrio et al. (1995), Graham et al. (1998), and Scott et al. (2014) concluded that only three bright galaxies do not harbor a disk-like component. Larger surveys with integral

¹ By the term “spheroid” we mean either an elliptical galaxy or the bulge component of a disk galaxy, with no attempt at distinguishing between classical bulges and disk-like pseudobulges.

field spectrographs of early-type galaxies, such as the ATLAS^{3D} Project (Cappellari et al. 2011), have further advanced this view of “elliptical” galaxies being all but simple and featureless pressure-supported systems. Most of the morphologically classified elliptical galaxies in the ATLAS^{3D} sample are fast rotators (Emsellem et al. 2011). Krajnović et al. (2013) showed that “fast rotators” as a class are **disk galaxies** or at least disk-like galaxies. In their magnitude-limited survey, systems without any signature of disk-like components (neither in the kinematics nor in the photometry) dominate only the most massive end (with stellar masses beyond $10^{11.5} M_{\odot}$) of the distribution. Given the prevalence of disks, it is clearly important to perform spheroid/disk decompositions, if one is to properly explore the black **hole–spheroid** connection. Indeed, separating the disk light from that of the bulge has led to the discovery of the missing population of compact, massive spheroids in the local universe (Graham et al. 2015). If we are to properly understand the evolution of galaxies, we need to understand their components.

Measuring the photometric and structural properties of a galaxy’s spheroidal component requires the ability to separate it from the rest of the galaxy. Such galaxy decomposition involves a parametric analysis that allows one to fit the surface brightness distribution of galaxies using a combination of analytic functions (usually one function per galaxy component, such as spheroids, disks, bars, nuclei, etc.). The one-dimensional (1D) technique involves fitting isophotes to the galaxy image, extracting the **(1D)** surface brightness radial **profile**, and modeling it with a combination of analytic functions. With the two-dimensional (2D) technique, one fits analytic functions directly to the 2D images.

Over the past **8 yr**, five independent studies (Graham & Driver 2007a; Sani et al. 2011; Beifiori et al. 2012; Vika et al. 2012; Läsker et al. 2014a, 2014b) have attempted galaxy decomposition in order to derive the spheroid parameters and explore their relation with the black hole masses. Interestingly, the past studies used almost the same sample of galaxies, yet they claimed some contradictory conclusions. For example, one study (Graham & Driver 2007a) obtained a good $M_{\text{BH}} - n_{\text{sph}}$ correlation (the spheroid Sérsic index n_{sph} is a measure of the central radial concentration of stars; Trujillo et al. 2001), whereas the remaining four did not.² In addition, Läsker et al. (2014b) declared that M_{BH} correlates equally well with the total galaxy luminosity as it does with the spheroid luminosity, as opposed to Beifiori et al. (2012), who claimed that the spheroid mass is a better tracer of M_{BH} than the galaxy mass (see also Kormendy & Gebhardt 2001; Erwin & Gadotti 2012). The past studies did not converge to the same conclusions because their best-fit models for the same galaxy were often significantly different and not consistent with each other in terms of fitted components. Moreover, none of these studies attempted an individual galaxy-by-galaxy comparison of their models with the previous literature. We have now made this comparison and performed the optimal decompositions, using $3.6 \mu\text{m}$ *Spitzer* satellite imagery, which is an excellent proxy for the stellar mass, superior to the **K band** (Jun & Im 2008; Sheth et al. 2010). We will use these in a series of forthcoming papers to obtain improved black hole mass scaling relations

² Savorgnan et al. (2013) showed that, by rejecting the most discrepant Sérsic index measurements and averaging the remaining ones, a strong $M_{\text{BH}} - n_{\text{sph}}$ correlation was recovered.

using the largest sample (66) of galaxies to date with accurate spheroid properties.

This paper is structured as follows. Section 2 presents the galaxy sample and imaging **data set** used to conduct this study. Section 3 describes how we performed the galaxy decompositions, i.e., how we identified and modeled the **subcomponents** that constitute our galaxies. In Section 4 we outline the results from our analysis and discuss the error analysis. Section 5 summarizes our main conclusions. The individual galaxy decompositions are made available in the electronic version of this manuscript.

2. DATA

Our initial galaxy sample (see Table 1) consists of 75 objects for which a dynamical detection of the black hole mass had been reported in the literature at the time we started this project, and for which at least one $3.6 \mu\text{m}$ *Spitzer*/IRAC³ observation was publicly available. **Black** hole masses were drawn from the catalog of Graham & Scott (2013) for 70 galaxies, from Rusli et al. (2013b) for **four galaxies**, and from Greenhill et al. (2003) for **one** galaxy. As explained in Section 4, this initial sample was ultimately reduced to 66 galaxies for which useful spheroid parameters could be obtained.

2.1. Spitzer/IRAC Observations

2.1.1. Data Acquisition

For each of our 75 galaxies, we downloaded from the Spitzer Heritage Archive⁴ all the available $3.6 \mu\text{m}$ IRAC Astronomical Observation Requests (AORs). Each AOR is an individual *Spitzer* observation **sequence** and includes a number of data frames (the individual exposures) and the calibration data. The data frames were selected to be corrected **basic calibrated data** (cBCD), produced by the IRAC Level 1 pipeline. This automatic pipeline takes a single “raw” image, removes the scattered light, and performs dark subtraction, **flat-fielding correction**, and flux calibration (into units of MJy sr^{-1}). The final product (the BCD) is a flux-calibrated image **that** has had all the well-understood instrumental signatures removed. BCD frames are further processed through an “artifact correction” pipeline that mitigates the commonly found artifacts of stray light, saturation, “**muxbleed**,” and column **pulldown**.⁵ After the artifact correction has been applied, the BCD becomes a cBCD.

2.1.2. Mosaicking

We performed image mosaicking using the MOPEX package (Makovoz & Marleau 2005). This enabled the production of suitably **wide field-of-view** images for accurate sky background subtraction. Individual cBCD frames with exposure time of **1 s** were rejected. Permanent or **semipermanent** bad pixels, contained in a **semistatic** mask (the “pmask”), were ignored. Each AOR is associated **with** a specific pmask. Therefore, when multiple AORs were available for the same

³ IRAC is the InfraRed Array Camera **on board** the *Spitzer Space Telescope*.

⁴ <http://irsa.ipac.caltech.edu/applications/Spitzer/SHA/>

⁵ Stray light includes scattered light from stars outside the array **location**, as well as filter ghosts from bright stars. Multiplexer bleed, or “**muxbleed**,” can be generated by stars, hot pixels, and particle hits. It appears as a decaying trail of pixels, repeating every fourth column. “Column pulldown” is caused by a bright pixel that triggers a bias shift within its respective column, creating a lower background value throughout the entire column than in the surrounding columns.

Table 1
Galaxy Sample

Galaxy	Distance (Mpc)	M_{BH} ($10^8 M_{\odot}$)	Ref.	Core ((arcsec))	Ref.	Rot.	Vel. Map	1D Fit	2D Fit
(1)	(2)	(3)	(4)	(5)	(6)	(7)	(8)	(9)	(10)
Circinus	4.0	$0.017^{+0.004}_{-0.003}$	G+03	no?	no	no
IC 1459	28.4	24^{+10}_{-10}	GS13	yes (0.7)	R+13a	yes	yes
IC 2560	40.7	$0.044^{+0.044}_{-0.022}$	GS13	no?	yes	no
IC 4296	40.7	11^{+2}_{-2}	GS13	yes?	yes	yes
M31	0.7	$1.4^{+0.9}_{-0.3}$	GS13	no	yes	no
M32	0.8	$0.024^{+0.005}_{-0.005}$	GS13	no	no	no
M49	17.1	25^{+3}_{-1}	R+13b	yes (1.5)	DG13, R+13a	SLOW	A	yes	yes
M59	17.8	$3.9^{+0.4}_{-0.4}$	GS13	no	...	FAST	A	yes	no
M60	16.4	47^{+10}_{-10}	GS13	yes (2.7)	DG13, R+13a	FAST	A, S	no	no
M64	7.3	$0.016^{+0.004}_{-0.004}$	GS13	no?	yes	no
M77	15.2	$0.084^{+0.003}_{-0.003}$	GS13	no	no	no
M81	3.8	$0.74^{+0.21}_{-0.11}$	GS13	no	yes	no
M84	17.9	$9.0^{+0.9}_{-0.8}$	GS13	yes (1.9)	F+06	SLOW	A, S	yes	yes
M87	15.6	$58.0^{+3.5}_{-3.5}$	GS13	yes (7.2)	F+06	SLOW	A, S	yes	yes
M89	14.9	$4.7^{+0.5}_{-0.5}$	GS13	yes (0.4)	DG13, R+13a	SLOW	A	yes	no
M94	4.4	$0.060^{+0.014}_{-0.014}$	GS13	no?	yes	no
M96	10.1	$0.073^{+0.015}_{-0.015}$	GS13	no	yes	yes
M104	9.5	$6.4^{+0.4}_{-0.4}$	GS13	yes	J+11	yes	no
M105	10.3	4^{+1}_{-1}	GS13	yes (1.1)	DG13, R+13a	FAST	A	yes	yes
M106	7.2	$0.39^{+0.01}_{-0.01}$	GS13	no	yes	no
NGC 0253	3.5	$0.10^{+0.10}_{-0.05}$	GS13	no	no	no
NGC 0524	23.3	$8.3^{+2.7}_{-1.3}$	GS13	yes (0.2)	R+11	FAST	A	yes	no
NGC 0821	23.4	$0.39^{+0.26}_{-0.09}$	GS13	no	...	FAST	A, S	yes	yes
NGC 1023	11.1	$0.42^{+0.04}_{-0.04}$	GS13	no	...	FAST	A, S	yes	yes
NGC 1300	20.7	$0.73^{+0.69}_{-0.35}$	GS13	no	yes	no
NGC 1316	18.6	$1.50^{+0.75}_{-0.80}$	GS13	no	...	FAST	...	yes	no
NGC 1332	22.3	14^{+2}_{-2}	GS13	no	yes	no
NGC 1374	19.2	$5.8^{+0.5}_{-0.5}$	R+13b	no?	...	FAST	A	yes	yes
NGC 1399	19.4	$4.7^{+0.6}_{-0.6}$	GS13	yes (2.4)	DG13, R+13a	SLOW	A	yes	no
NGC 2273	28.5	$0.083^{+0.004}_{-0.004}$	GS13	no	yes	no
NGC 2549	12.3	$0.14^{+0.02}_{-0.13}$	GS13	no	...	FAST	A	yes	yes
NGC 2778	22.3	$0.15^{+0.09}_{-0.10}$	GS13	no	...	FAST	A	yes	no
NGC 2787	7.3	$0.40^{+0.04}_{-0.05}$	GS13	no	yes	no
NGC 2974	20.9	$1.7^{+0.2}_{-0.2}$	GS13	no	...	FAST	A, S	yes	yes
NGC 3079	20.7	$0.024^{+0.024}_{-0.012}$	GS13	no?	yes	no
NGC 3091	51.2	36^{+1}_{-2}	R+13b	yes (0.6)	R+13a	yes	yes
NGC 3115	9.4	$8.8^{+10.0}_{-2.7}$	GS13	no	yes	no
NGC 3227	20.3	$0.14^{+0.10}_{-0.06}$	GS13	no	yes	no
NGC 3245	20.3	$2.0^{+0.5}_{-0.5}$	GS13	no	...	FAST	A	yes	yes
NGC 3377	10.9	$0.77^{+0.04}_{-0.06}$	GS13	no	...	FAST	A, S	yes	yes
NGC 3384	11.3	$0.17^{+0.01}_{-0.02}$	GS13	no	...	FAST	A	yes	no
NGC 3393	55.2	$0.34^{+0.02}_{-0.02}$	GS13	no	yes	yes
NGC 3414	24.5	$2.4^{+0.3}_{-0.3}$	GS13	no	...	SLOW	A	yes	no
NGC 3489	11.7	$0.058^{+0.008}_{-0.008}$	GS13	no	...	FAST	A	yes	yes
NGC 3585	19.5	$3.1^{+1.4}_{-0.6}$	GS13	no	yes	no
NGC 3607	22.2	$1.3^{+0.5}_{-0.5}$	GS13	no	...	FAST	A	yes	yes
NGC 3608	22.3	$2.0^{+1.1}_{-0.6}$	GS13	yes (0.2)	DG13, R+13a	SLOW	A, S	yes	yes
NGC 3842	98.4	97^{+30}_{-26}	GS13	yes (0.7)	DG13, R+13a	yes	no
NGC 3998	13.7	$8.1^{+2.0}_{-1.9}$	GS13	no	...	FAST	A	yes	no
NGC 4026	13.2	$1.8^{+0.6}_{-0.3}$	GS13	no	...	FAST	A	yes	no
NGC 4151	20.0	$0.65^{+0.07}_{-0.07}$	GS13	no	yes	no
NGC 4261	30.8	5^{+1}_{-1}	GS13	yes (1.6)	R+11	SLOW	A	yes	yes
NGC 4291	25.5	$3.3^{+0.9}_{-2.5}$	GS13	yes (0.3)	DG13, R+13a	yes	yes
NGC 4342	23.0	$4.5^{+2.3}_{-1.5}$	GS13	no	...	FAST	A	no	no
NGC 4388	17.0	$0.075^{+0.002}_{-0.002}$	GS13	no?	yes	no
NGC 4459	15.7	$0.68^{+0.13}_{-0.13}$	GS13	no	...	FAST	A	yes	no

Table 1
(Continued)

Galaxy	Distance (Mpc)	M_{BH} ($10^8 M_{\odot}$)	Ref.	Core ((arcsec))	Ref.	Rot.	Vel. Map	1D Fit	2D Fit
(1)	(2)	(3)	(4)	(5)	(6)	(7)	(8)	(9)	(10)
NGC 4473	15.3	$1.2^{+0.4}_{-0.9}$	GS13	no	...	FAST	A, S	yes	yes
NGC 4486A	17.0	$0.13^{+0.08}_{-0.08}$	GS13	no	...	FAST	A	no	no
NGC 4564	14.6	$0.60^{+0.03}_{-0.09}$	GS13	no	...	FAST	A	yes	no
NGC 4596	17.0	$0.79^{+0.38}_{-0.33}$	GS13	no	...	FAST	A	yes	no
NGC 4697	11.4	$1.8^{+0.2}_{-0.1}$	GS13	no	...	FAST	A, S	yes	yes
NGC 4889	103.2	210^{+160}_{-160}	GS13	yes (1.7)	F+97	yes	yes
NGC 4945	3.8	$0.014^{+0.014}_{-0.007}$	GS13	no?	yes	yes
NGC 5077	41.2	$7.4^{+4.7}_{-3.0}$	GS13	yes (0.3)	T+04	yes	yes
NGC 5128	3.8	$0.45^{+0.17}_{-0.10}$	GS13	no?	yes	no
NGC 5576	24.8	$1.6^{+0.3}_{-0.4}$	GS13	no	...	SLOW	A	yes	yes
NGC 5813	31.3	$6.8^{+0.7}_{-0.7}$	GS13	yes (0.4)	DG13, R+13a	SLOW	A	no	no
NGC 5845	25.2	$2.6^{+0.4}_{-1.5}$	GS13	no	...	FAST	A	yes	yes
NGC 5846	24.2	11^{+1}_{-1}	GS13	yes	F+97	SLOW	A, S	yes	yes
NGC 6251	104.6	5^{+2}_{-2}	GS13	yes?	yes	yes
NGC 7052	66.4	$3.7^{+2.6}_{-1.5}$	GS13	yes (0.8)	Q+00	yes	yes
NGC 7582	22.0	$0.55^{+0.26}_{-0.19}$	GS13	no	no	no
NGC 7619	51.5	25^{+8}_{-3}	R+13b	yes ^a (0.5)	DG13, R+13a	yes	no
NGC 7768	112.8	13^{+5}_{-4}	GS13	yes	G+94	yes	no
UGC 03789	48.4	$0.108^{+0.005}_{-0.005}$	GS13	no?	yes	no

Notes. Column (1): galaxy name. Column (2): distance. Column (3): black hole mass. Column (4): reference of the black hole mass reported here (G+03—Greenhill et al. 2003; GS13—Graham & Scott 2013; R+13b—Rusli et al. 2013b). Column (5): presence of a partially depleted core. The question mark is used when the classification has come from the velocity dispersion criteria mentioned in Section 2.2.3. The value of the core break radius is reported in parentheses when available. Column (6): reference of the identification of a partially depleted core (G+94—Grillmair et al. 1994; F+97—Forbes et al. 1997; Q+00—Quillen et al. 2000; T+04—Trujillo et al. 2004; F+06—Ferrarese et al. 2006; J+11—Jardel et al. 2011; R+11—Richings et al. 2011; DG13—Dullo & Graham 2013; R+13a—Rusli et al. 2013a). Column (7): kinematical classification (fast/slow rotator). Column (8): availability of velocity map (A—ATLAS^{3D}; S—SLUGGS). Column (9): completion of 1D fit. Column (10): completion of 2D fit.

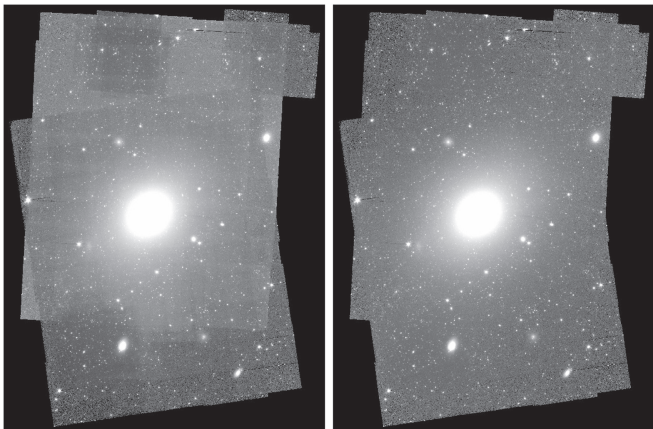


Figure 1. Example of the *overlap* correction. The image mosaic of the galaxy M49 was obtained by co-adding frames coming from eight different AORs. The evident patchiness (left image) was removed (right image) using the *overlap* module.

galaxy, we merged the different pmasks. Cosmic-ray rejection was performed with the dual outlier and multiframe techniques. The pixel size of the mosaic was set to be the same as the input cBCD frames ($1.^{\prime\prime}22 \times 1.^{\prime\prime}22$). For $3.6 \mu\text{m}$ observations with this pixel scale, the photometric zero-point magnitude is $m_{\text{zp}} = 17.26$ mag. The orientation of the mosaic was set to the average rotation angle of the input cBCD frames. Individual cBCD frames were combined together into a single mosaic with the default linear interpolation algorithm.

^a NGC 7619 may contain an embedded disk rather than possessing a partially depleted core.

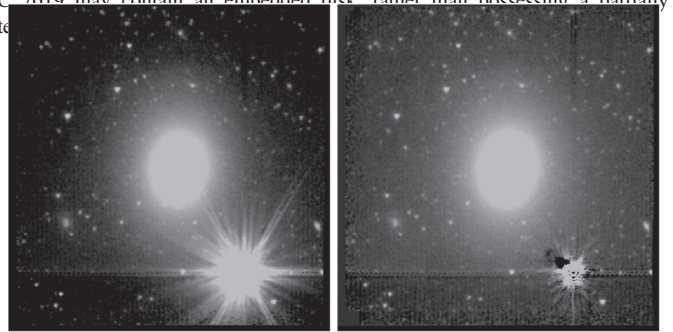


Figure 2. Example of aesthetic correction. The images show the mosaic of the galaxy NGC 4459 before (left) and after (right) the partial removal of a bright saturated star.

2.1.3. Overlap Correction

Before generating a mosaic, MOPEX can perform background matching among the individual frames by using the *overlap* module. This module calculates and applies an additive correction to the individual frames, producing a consistent background across the mosaicked image. According to the *Spitzer Data Analysis Cookbook*,⁶ the use of the *overlap* module is not particularly recommended for $3.6 \mu\text{m}$ observations. However, after a visual inspection of the mosaics

⁶ http://irsa.ipac.caltech.edu/data/SPITZER/docs/dataanalysis/tools/cookbook/Spitzer_Data_Cookbook.pdf

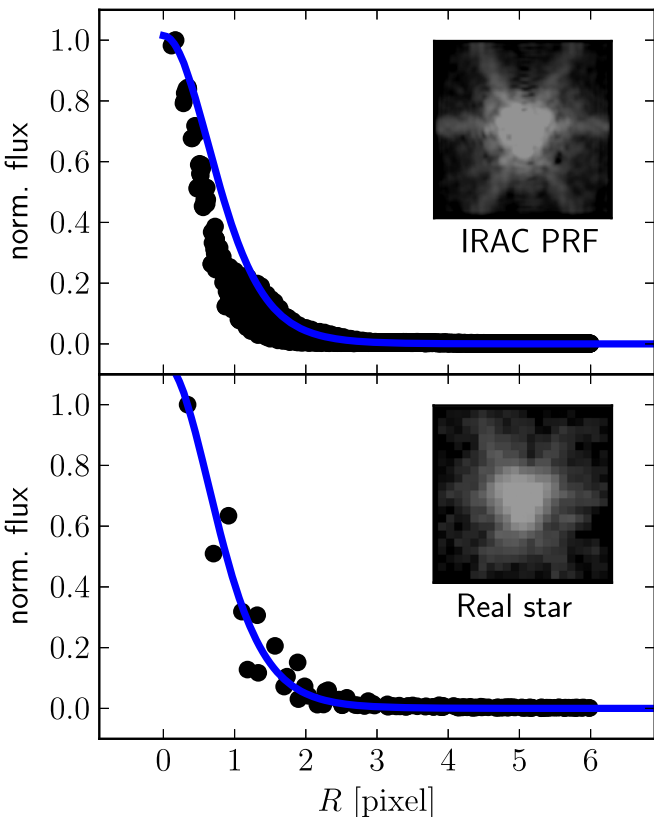


Figure 3. Normalized flux vs. radial distance from the image centroid of an observed point source (bottom panel) and of the IRAC instrument PRF (top panel). The normalized flux is given in arbitrary units, and the radial distance is in units of pixel size of the IRAC detector (1 pixel = $1''\!22$). The blue solid line shows our 1D Moffat PSF model, which has been normalized to intersect the data point with the largest flux. The FWHM of the IRAC PRF is clearly smaller than that of a “real” star. The inserts display the images of the observed point source and the IRAC PRF.

obtained without activating the *overlap* module, we found that all the mosaics obtained from multiple AORs were affected by patchiness, owing to bias fluctuations in the CCD array. For this reason, we regenerated the multiple-AOR mosaics by activating the *overlap* correction, which successfully removed the “chessboard” pattern (see Figure 1 for an example).

2.1.4. Sigma Mosaics

For each individual cBCD frame, the IRAC Level 1 pipeline calculates the uncertainty associated with each pixel and produces an uncertainty frame (or sigma frame). The initial uncertainty is estimated as the Poisson noise in electrons plus the readout noise added in quadrature ($\sigma^2 = \sigma_{\text{readoutnoise}}^2 + \sigma_{\text{Poisson}}^2$). This initial sigma frame is carried through the pipeline, and additional uncertainties (e.g., dark current and flat field uncertainties) are added in quadrature when appropriate. When MOPEX generates an image mosaic, it also produces the associated sigma mosaic by interpolating the individual uncertainty frames and co-adding them, following the standard assumption of additive variances.

⁷ IRAF is the Image Reduction and Analysis Facility, distributed by the National Optical Astronomy Observatory, which is operated by the Association of Universities for Research in Astronomy (AURA) under cooperative agreement with the National Science Foundation.

2.1.5. Sky Subtraction

Sky subtraction was performed manually on the image mosaics using the tasks `marksky` and `skyfit` of the IRAF⁷ package `GALPHOT`.⁸ The task `skyfit` also provided an estimate of the sky rms (rms_{sky}).

2.1.6. Additional Aesthetic Corrections

The image mosaics of four galaxies (NGC 0821, NGC 2974, NGC 4291, NGC 4459) were found to be affected by bright, highly saturated stars lying close to the target galaxies. These stars were modeled and subtracted using the software Galfit (Peng et al. 2010) and the extended IRAC point response function (PRF) image at $3.6\,\mu\text{m}$. This helped remove the extended wings and spikes of the saturated stars (see Figure 2 for an example).

2.1.7. Image Masking

Galactic stars and any other objects different from the target galaxy were masked through a two-step procedure. First, we created an initial mask using the IRAF task `objmasks` that identifies objects by threshold sigma detection. Then, we refined each mask by hand, using the software SAOImage DS9⁹ in conjunction with the IRAF task `mskregions`. We identified and carefully masked not only contaminating sources located in the field of the image mosaic but also objects overlapping with the target galaxy, such as foreground stars, background galaxies, globular clusters, and red giant stars.

2.1.8. 1D Point-spread Function (PSF)

A universal,¹⁰ average, 1D PSF was characterized using the IRAF task `imexamine`. A nonlinear least-squares Moffat (1969) profile¹¹ of fixed center and zero background was fit to the (background-subtracted) pixels of 20 bright stars, belonging to different image mosaics. The best-fit parameters of the 20 stars were then averaged together. Doing so, we obtained $(\alpha, \beta) = (2.''38, 4.39)$.

2.1.9. 2D PSF

The IRAC support team provides users with a 2D instrument PRF at $3.6\,\mu\text{m}$. However, while this helped remove the extended wings of saturated stars (see Section 2.1.6), we found

⁸ GALPHOT was developed in the IRAF—STSDAS environment mainly by W. Freudling, J. Salzer, and M. P. Haynes (Haynes et al. 1999).

⁹ SAOImage DS9 development has been made possible by funding from the Chandra X-ray Science Center (CXC) and the High Energy Astrophysics Science Archive Center (HEASARC).

¹⁰ Across all mosaics, the variation of the Moffat FWHM is $\pm 0.''1$, and the variation of the Moffat β is ± 2.0 . The use of a universal PSF is justified for the following reasons: (i) the PSF convolution is more sensitive to the value of the FWHM than β , i.e., having a 50% variation in β is not an issue as long as the variation in FWHM is small; (ii) the use of a non-signal-to-noise-weighted fitting scheme minimizes biases from a nonaccurate PSF description; (iii) not all mosaics have enough stars suitable for the PSF characterization: rather than having an individual PSF for each mosaic (which would have been based on only one to two stars for some mosaics), we preferred the use of a universal PSF.

¹¹ The Moffat (1969) profile has the following form:

$$\mu = \mu_0 - 2.5 \log \left[1 + \left(\frac{R}{\alpha} \right)^2 \right]^{-\beta}, \quad (1)$$

where R is the projected radius, μ_0 is the central surface brightness, and α and β regulate the width and the shape of the profile.

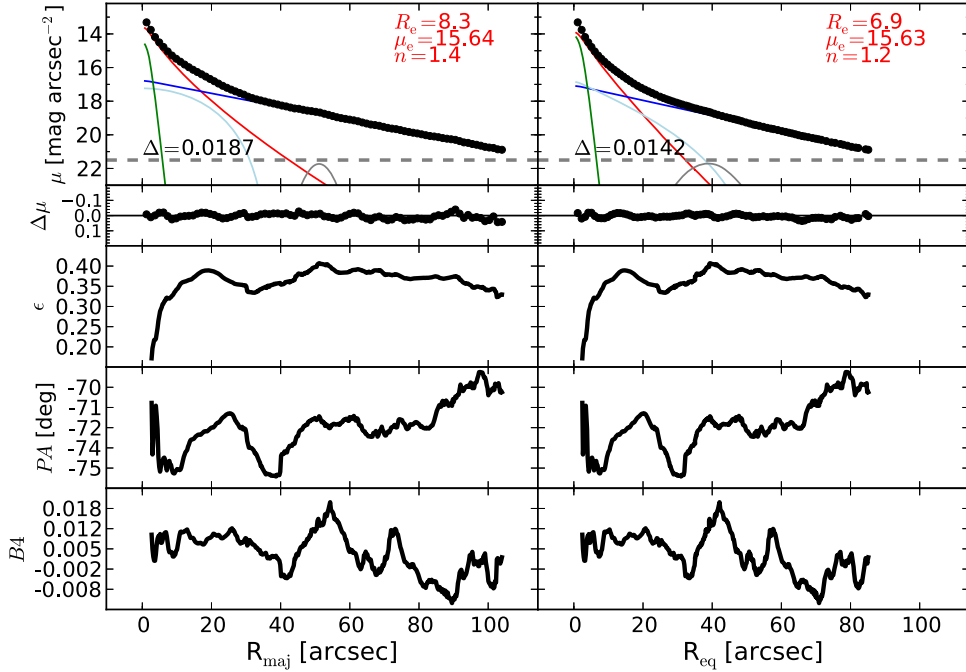


Figure 4. Best-fit model and isophotal parameters for the galaxy NGC 2974. The left panels refer to the major-axis R_{maj} , while the right panels refer to the equivalent-axis R_{eq} , i.e., the geometric mean of the major (a) and minor (b) axis ($R_{\text{eq}} = \sqrt{ab}$). The top panels display the galaxy surface brightness radial profiles obtained with a linear sampling. The black points are the observed data. The colored lines represent the individual (PSF-convolved) model components: red = Sérsic (bulge), dark blue = exponential (disk), green = Gaussian (AGN), cyan = Ferrer (bar), gray = Gaussian ring (ring). The best-fit parameters for the Sérsic bulge model are inset. The total (PSF-convolved) model is shown with a black dashed line, but it is hard to distinguish because it almost perfectly matches the data, hence the residual profile is additionally shown as $\Delta\mu$ in the second row. The horizontal gray dashed line corresponds to an intensity equal to three times the rms of the sky background fluctuations ($3 \times \text{rms}_{\text{sky}}$). Δ denotes the rms scatter of the fit in units of mag arcsec $^{-2}$. The lower six panels show the ellipticity (ϵ), position angle (PA), and fourth harmonic (B_4) radial profiles. Such profiles are available online for all other galaxies successfully modeled in 1D (see Table 2).

this PRF to be inadequate for the purposes of our modeling. In fact, the FWHM of the IRAC instrument PRF ($\sim 1''.8$), as measured by the IRAF task `imexamine`, is systematically smaller than the average FWHM of “real” stars ($\sim 2''.0$). Figure 3 illustrates this issue. We also tested the IRAC PRF by providing it as the input PSF for Galfit and fitting a number of stars in different image mosaics. A visual inspection of the fit residuals confirmed that the IRAC instrument PRF is narrower than “real” point sources. For this reason, we constructed our 2D PSF according to the following method (as directed by C. Peng 2015, private communication).

We provided the IRAC instrument PRF as the input PSF for Galfit and simultaneously fit seven bright stars (belonging to different mosaics), modeling the stars with Moffat profiles and constraining all the profiles to have the same (α, β), position angle, and axis ratio. The 2D PSF image was then obtained by taking the best-fit Moffat model—the same best-fit model for all seven stars, by construction—and convolving it with the IRAC instrument PRF. The advantage of this method is to obtain a 2D PSF that is wider than the instrument PRF but maintains the asymmetric features of the instrument PRF (e.g., wings and spikes). We then tested this 2D PSF on a number of stars (these stars were different from the seven stars employed to build the 2D PSF image) and verified that it correctly reproduces the shape of “real” point sources.

2.2. Additional Data

2.2.1. Kinematics

A kinematical classification (slow/fast rotator) is available for 34 of our 75 galaxies from the ATLAS^{3D} survey (Emsellem

et al. 2011) and for three additional galaxies from Scott et al. (2014). This classification (Table 1, column (7)) concerns the kinematic properties of galaxies within the spectroscopic instrument’s field of view, but does not contain additional information—crucial for our analysis—about kinematic substructures, such as embedded disks or kinematically decoupled components, which can require separate modeling. For this reason, we also visually inspected the velocity fields of our galaxies, when available from the literature. Velocity maps were taken from the ATLAS^{3D} survey for 34 galaxies (observed with SAURON by Krajnović et al. 2011), from Scott et al. (2014) for 2 galaxies (observed with WiFeS), and from the SLUGGS survey for 12 galaxies (observed with DEIMOS by Arnold et al. 2014). While the fields of view of SAURON ($33'' \times 41''$) and WiFeS ($25'' \times 38''$) reach to about one galaxy effective radius (for our local galaxies), observations taken with DEIMOS can probe the galaxy kinematics well beyond two effective radii.

2.2.2. Active Galactic Nuclei (AGNs) and Nuclear Dust

The X-ray, UV, and optical radiation emitted by the accretion disks of AGNs can stimulate infrared thermal emission from circumnuclear dust, if present. This means that if a galaxy hosts an optical AGN and a certain amount of nuclear dust, we may detect some nonstellar nuclear emission at $3.6 \mu\text{m}$. It is therefore important to identify which of our galaxies have both an optical AGN and circumnuclear dust. To help with this task, we searched NED¹² for the individual

¹² NED is the NASA/IPAC Extragalactic Database.

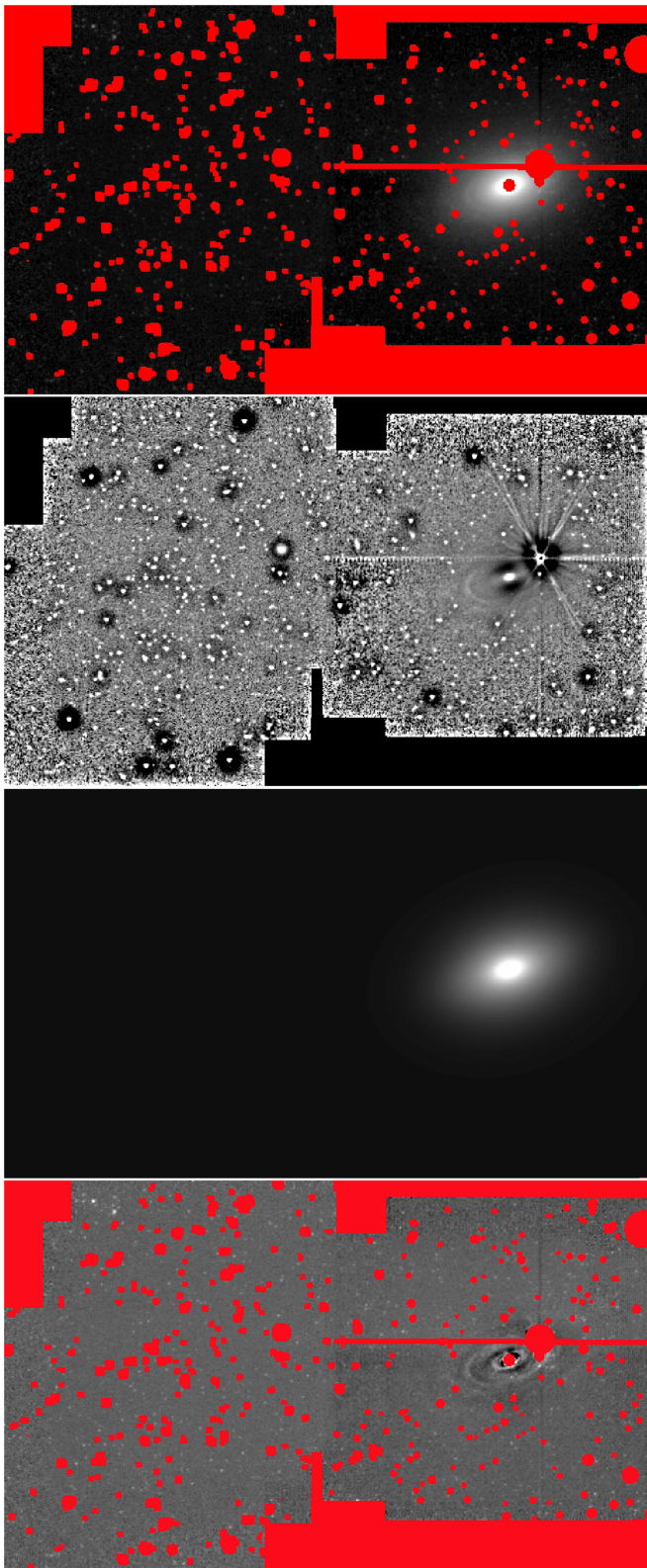


Figure 5. Image of the galaxy NGC 2974 with its mask (top panel, on a logarithmic scale), unsharp mask (second panel, on a linear scale), best-fit 2D model (third panel, on a logarithmic scale), and residual image after the subtraction of the 2D model (bottom panel, on a linear scale; the residual patterns correspond to differences between the data and the model of less than 6%). The left-hand side of the mosaic allowed an accurate determination of the sky background level.

galaxies and their associated literature. Unsurprisingly, dusty AGNs were more frequently found in late-type spiral galaxies and modeled by us with either a point source or a PSF-convolved Gaussian.

2.2.3. Sérsic/Core-Sérsic Classification

Core-Sérsic galaxies (Graham and Guzmán 2003; Graham et al. 2003; Trujillo et al. 2004) are galaxies (or spheroids) with partially depleted cores, i.e., a central deficit of light relative to the inward extrapolation of their outer Sérsic light profile. Such deficits were first noted and researched by King & Minkowski (1966). Sérsic galaxies, instead, do not exhibit such central stellar deficits. Partially depleted cores, as measured from high-resolution observations, have typical sizes of a few tens of parsecs (Rusli et al. 2013a; Dullo & Graham 2014). The majority are thus unresolved in our image mosaics. We masked these unresolved cores (identified in high-resolution images; - see Table 1) by excluding the surface brightness profile within 3 PSF's FWHM from the galaxy center. In the case of cores with sizes exceeding the PSF's FWHM, we excluded the data points within the size of the core plus 3 PSF's FWHM. The Sérsic/core-Sérsic classification presented in this work (Table 1, column (5)) comes from the compilation of Savorgnan & Graham (2015b), who identified partially depleted cores according to the same criteria used by Graham & Scott (2013). When no high-resolution image analysis was available from the literature, they inferred the presence of a partially depleted core based on the stellar velocity dispersion, σ : a galaxy is classified as core-Sérsic if $\sigma > 270 \text{ km s}^{-1}$, or as Sérsic if $\sigma < 166 \text{ km s}^{-1}$. This resulted in us assigning cores to just two galaxies using this alternative method when no high-resolution image was available.

3. ANALYSIS

3.1. Isophotal Analysis

We performed an isophotal analysis of our galaxies using the IRAF task `ellipse` (Jedrzejewski 1987), which fits elliptical isophotes to galaxy images. The center of the isophotes was held fixed, while the ellipticity (ϵ), the position angle (P.A.), and the amplitude of the fourth harmonic¹³ (B_4) were allowed to vary with radius. The step in semimajor axis length between successive ellipses was first set to increase linearly, and then geometrically in our second run.¹⁴ As a result, for each galaxy we produced respectively a “linearly sampled” and a “logarithmically sampled” surface brightness profile along the major axis. Major-axis surface brightness profiles were additionally converted into the equivalent axis, i.e., the geometric mean of the major (a) and minor (b) axis ($R_{\text{eq}} = \sqrt{ab}$), equivalent to the circularized radius. This resulted in four profiles per galaxy. Isophotes corresponding to an intensity less than three times the rms of the sky background fluctuations ($3 \times \text{rms}_{\text{sky}}$) were ignored. Some surface brightness profiles were truncated at our discretion before the $3 \times \text{rms}_{\text{sky}}$ limit, according to specific technical reasons (e.g., contamination from light of a neighboring galaxy, disturbed morphology in

¹³ The amplitude of the fourth harmonic deviations from perfect ellipses (B_4) parameterizes the diskyness ($B_4 > 0$) or boxyness ($B_4 < 0$) of the isophotes.

¹⁴ In the case of linear steps, the semimajor axis length for the next ellipse was calculated by adding 1 pixel to the current length. In the case of geometric steps, the semimajor axis length for the next ellipse was calculated as 1.1 times the current length.

Table 2
Results of Galaxy Decompositions

Galaxy (1)	1D Major Axis				1D Equivalent Axis				2D			
	R_e (2)	μ_e (3)	n (4)	R_e (5)	μ_e (6)	n (7)	m_{sph} (8)	m_{gal} (9)	Q.F. (10)	R_e (11)	n (12)	m_{sph} (13)
Circinus
IC 1459	63.1	18.49	6.6	57.3	18.59	7.0	6.11	6.11	1	87.5	8.3	6.04
IC 2560	6.1	16.58	0.8	4.5	16.48	0.6	10.77	8.29	2
IC 4296	65.9	19.32	5.8	68.1	19.48	6.2	6.70	6.70	1	82.3	6.6	6.66
M104	11.0	14.63	5.8	19.6	15.78	3.7	5.98	4.68	2
M105	57.2	17.93	5.2	50.9	17.84	5.3	5.77	5.77	2	73.6	7.0	5.62
M106	15.3	16.11	2.0	8.3	15.57	1.2	8.18	5.24	1
M31	418.6	16.80	2.2	173.6	15.63	1.3	1.61	-0.33	1
M32
M49	190.2	19.33	6.6	135.3	18.83	5.4	4.63	4.63	1	151.9	5.5	4.64
M59	48.0	18.02	5.5	90.9	19.67	8.8	6.07	5.98	1
M60
M64	3.8	13.38	0.8	4.3	13.78	1.4	7.78	5.08	1
M77
M81	31.0	15.22	1.7	33.2	15.55	2.1	4.89	3.47	3
M84	101.6	19.01	7.8	129.8	19.57	7.9	5.25	5.25	2	181.8	8.4	5.20
M87	203.0	19.87	10.0	87.1	18.26	5.9	4.97	4.97	2	88.3	4.3	5.11
M89	29.0	17.14	4.6	28.2	17.15	5.1	6.38	6.12	2
M94	11.4	13.73	0.9	8.4	13.50	1.1	6.14	4.86	1
M96	7.5	14.63	1.5	5.3	14.28	1.3	7.87	5.82	1	8.3	2.0	7.36
NGC 0253
NGC 0524	6.0	15.24	1.1	5.8	15.21	1.1	8.65	6.91	1
NGC 0821	36.5	18.40	5.3	18.9	17.83	6.1	7.85	7.59	3	33.8	2.5	7.78
NGC 1023	9.2	14.96	2.1	7.4	14.79	2.0	7.41	6.03	1	6.6	2.3	7.49
NGC 1300	9.9	17.62	3.8	8.1	17.41	3.6	9.52	7.42	2
NGC 1316	21.5	15.55	2.0	15.9	15.43	1.8	6.46	4.87	2
NGC 1332	34.7	17.44	5.1	18.0	16.47	3.7	6.85	6.79	3
NGC 1374	25.6	18.06	3.7	24.8	18.11	4.1	7.74	7.72	1	25.2	3.7	7.81
NGC 1399	405.2	21.80	10.0	338.1	21.53	10.0	5.01	4.98	1
NGC 2273	1.6	13.36	2.1	1.9	13.83	2.7	9.27	8.06	2
NGC 2549	6.1	15.57	2.3	3.1	14.54	1.5	9.20	7.85	1	5.6	2.1	8.76
NGC 2778	2.3	15.61	1.3	2.2	15.46	1.2	10.94	9.30	2
NGC 2787	4.8	14.86	1.1	3.3	14.62	1.3	9.21	7.04	2
NGC 2974	8.3	15.64	1.4	6.9	15.63	1.2	8.65	7.44	2	10.6	1.3	8.39
NGC 3079	6.8	14.47	1.3	4.3	14.48	1.1	8.57	7.13	2
NGC 3091	100.5	20.43	7.6	51.2	19.47	6.6	7.27	7.27	1	67.1	6.7	7.26
NGC 3115	43.6	16.67	4.4	34.4	16.85	5.1	5.65	5.47	1
NGC 3227	8.1	16.56	1.7	4.6	15.83	1.1	9.77	7.28	2
NGC 3245	4.4	14.96	2.9	2.4	14.00	1.7	9.11	7.66	1	1.9	1.8	9.19
NGC 3377	61.8	19.16	7.7	91.7	20.33	9.2	6.69	6.62	2	71.8	3.7	7.21
NGC 3384	5.5	14.21	1.6	5.6	14.56	1.8	7.83	6.52	1
NGC 3393	1.4	14.03	3.4	1.4	14.15	2.6	10.23	8.42	2	1.2	1.9	10.45
NGC 3414	28.0	18.10	4.8	25.5	18.08	4.5	7.60	7.53	1
NGC 3489	2.2	13.47	1.5	1.7	13.25	1.3	9.21	7.27	2	1.7	2.1	9.04
NGC 3585	105.0	19.13	5.2	86.3	19.24	6.3	5.93	5.90	2
NGC 3607	69.3	19.00	5.5	65.5	19.01	5.6	6.37	6.29	2	60.0	5.3	6.40
NGC 3608	47.5	18.93	5.2	43.4	19.00	5.7	7.25	7.25	2	62.0	7.0	7.15
NGC 3842	100.7	21.43	8.1	73.6	21.07	8.2	7.97	7.92	1
NGC 3998	5.8	15.15	1.2	4.8	14.63	1.3	8.37	7.15	3
NGC 4026	3.4	15.52	2.4	6.3	16.09	2.1	9.02	7.44	3
NGC 4151	7.6	15.50	1.4	6.8	15.26	1.9	8.10	7.06	2
NGC 4261	52.6	18.58	4.7	47.3	18.53	4.3	6.72	6.68	2	50.4	4.4	6.73
NGC 4291	15.0	17.14	4.2	15.4	17.51	5.9	7.99	7.99	2	20.8	7.7	7.91
NGC 4342
NGC 4388	4.6	15.89	0.6	4.2	15.86	1.3	9.89	7.66	3
NGC 4459	18.4	16.69	3.1	13.0	16.23	2.6	7.50	6.97	2
NGC 4473	45.9	17.93	2.3	36.9	18.10	2.9	7.04	6.82	2	49.8	3.0	7.03
NGC 4486A
NGC 4564	5.0	15.23	2.6	6.0	15.65	3.0	8.52	7.83	1
NGC 4596	6.6	15.93	2.7	9.0	16.44	3.0	8.43	6.98	1
NGC 4697	239.3	20.62	7.2	226.4	20.90	6.7	5.47	5.34	3	121.4	5.0	5.72
NGC 4889	119.7	21.01	8.1	60.8	20.11	6.8	7.53	7.53	1	104.3	7.8	7.43

Table 2
(Continued)

Galaxy (1)	1D Major Axis			1D Equivalent Axis			2D					
	R_e (2)	μ_e (3)	n (4)	R_e (5)	μ_e (6)	n (7)	m_{sph} (8)	m_{gal} (9)	Q.F. (10)	R_e (11)	n (12)	m_{sph} (13)
NGC 4945	13.9	14.95	1.4	9.5	14.78	1.7	6.94	4.11	2	16.2	0.8	7.07
NGC 5077	23.5	17.67	4.2	23.0	18.01	5.7	7.62	7.62	1	30.5	6.8	7.57
NGC 5128	61.3	15.73	1.2	60.8	16.01	2.2	4.01	2.93	3
NGC 5576	61.5	19.41	3.3	49.3	19.34	3.7	7.53	7.53	1	45.9	8.3	7.19
NGC 5813
NGC 5845	3.6	14.79	2.5	3.1	14.64	2.3	9.05	8.91	3	2.8	2.4	9.09
NGC 5846	105.1	19.67	6.4	83.4	19.28	5.7	6.10	6.10	2	85.1	5.2	6.14
NGC 6251	41.7	19.82	6.8	30.1	19.31	5.6	8.35	8.35	1	39.3	7.1	8.27
NGC 7052	59.4	19.38	4.2	37.0	19.19	5.6	7.79	7.79	1	36.2	4.0	8.09
NGC 7582
NGC 7619	63.2	19.53	5.3	58.0	19.55	5.2	7.21	7.15	2
NGC 7768	92.9	21.37	8.4	42.1	20.15	6.7	8.36	8.36	2
UGC 03789	1.8	15.26	1.9	2.4	15.39	1.4	10.65	9.22	3	-

Note. Column (1): galaxy name. Columns (2)–(4): effective radius (in units of arcsec), surface brightness at the effective radius (in units of mag arcsec⁻²), and Sérsic index for 1D fits along the major axis. Columns (5)–(9): effective radius (in units of arcsec), surface brightness at the effective radius (in units of mag arcsec⁻²), Sérsic index, spheroid apparent magnitude (in units of mag), and galaxy apparent magnitude (in units of mag) for 1D fits along the equivalent axis. Column (10): quality flag of the 1D fits (see Section 4.2). Columns (11)–(13): effective radius (in units of arcsec), Sérsic index, and spheroid apparent magnitude (in units of mag) for 2D fits.

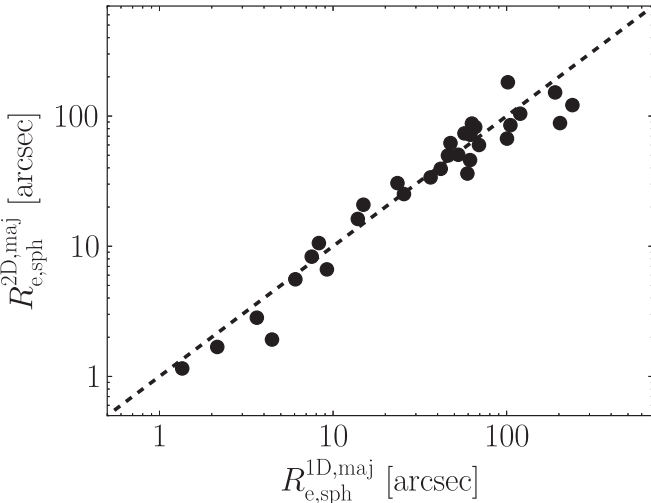


Figure 6. 2D vs. 1D major-axis measurements of the spheroid effective radii. The dashed line displays the 1:1 relation.

the galaxy outskirts, etc.). In particular, we did not attempt to fit bends or truncations of large-scale disks (e.g., Erwin et al. 2005, 2008, 2012; Gutiérrez et al. 2011; Comerón et al. 2012; Muñoz-Mateos et al. 2013; Kim et al. 2014), but instead truncated the surface brightness profiles before the occurrence of such features. Individual cases are discussed in Section 5.1.

3.2. Unsharp Masking

Unsharp masking is an image-sharpening technique that is useful to reveal asymmetric structures in galaxies, such as bars or (inclined) embedded disks. First, the original galaxy image was smoothed with a Gaussian filter. Then, the original image was divided by the smoothed one. The result of such an operation is the “unsharp mask.” The asymmetric features revealed by this technique have sizes comparable to the FWHM of the Gaussian kernel used for the smoothing. Therefore, for each galaxy, we produced a set of different unsharp masks by varying the FWHM of the filter, to identify

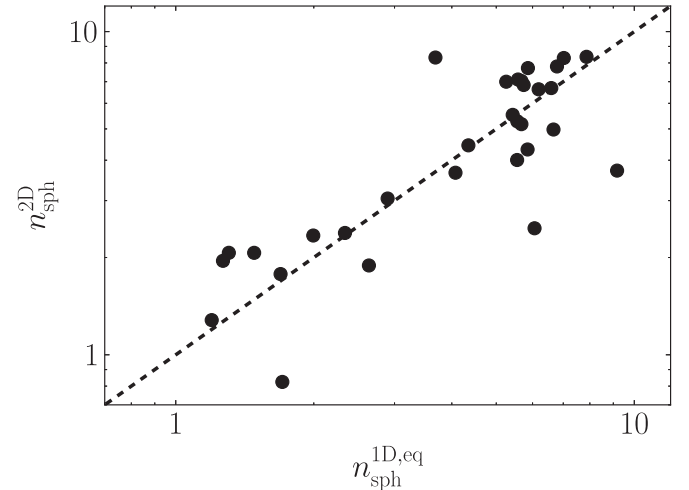


Figure 7. 2D measurements of the spheroid Sérsic indices roughly approximate the 1D equivalent-axis measurements. The dashed line displays the 1:1 relation. The four most obvious outliers are NGC 821, NGC 3377, NGC 4945, and NGC 5576. Their individual cases are discussed in the Appendix.

all the asymmetric features that could bias the fitting process and may therefore need to be considered during the galaxy modeling phase. This information was used in combination with kinematic and AGN information discussed in Section 2.2.

3.3. 1D Fitting Routine

The decomposition of the surface brightness profiles was performed with software written by G. Savorgnan. This software can fit an observed surface brightness profile with any linear combination of a set of analytical functions (Sérsic, exponential, Gaussian, Moffat, Ferrer, symmetric Gaussian ring, etc.; see the Appendix for a description of the analytical form of these profiles). At each iteration, the model is numerically convolved with a Moffat filter, to account for PSF effects, and then matched to the data. The minimization routine is based on the Levenberg–Marquardt algorithm. During the fit, we deliberately did not make use of any

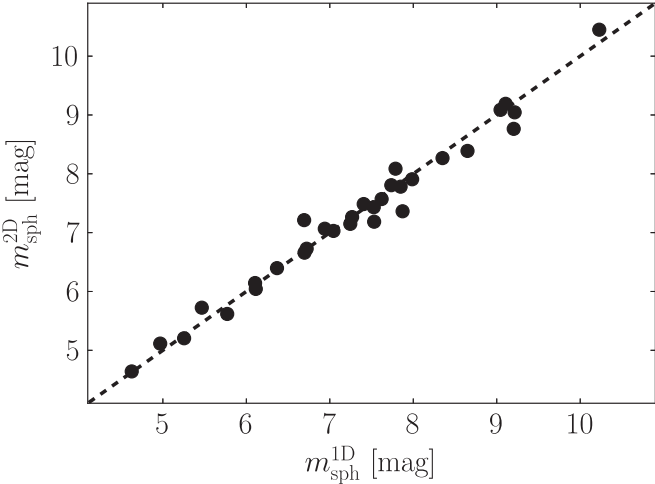


Figure 8. 2D vs. 1D measurements of the $3.6\ \mu\text{m}$ spheroid magnitudes. The dashed line displays the 1:1 relation.

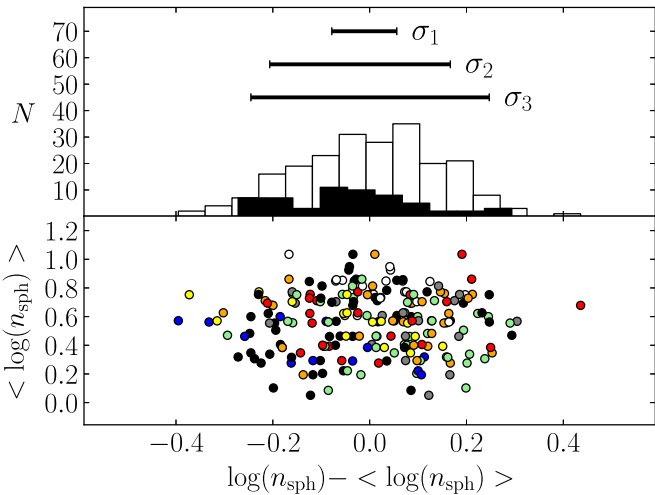


Figure 9. Bottom panel: 58 galaxies for which at least one measurement of the spheroid Sérsic index n_{sph} is available from the literature (Table 3), in addition to that measured by us. The average (logarithmic) value ($\langle \log(n_{\text{sph}}) \rangle$) is plotted against the difference between (the logarithm of) the individual measurements of a galaxy and the average (logarithmic) value for that same galaxy. Each data point corresponds to an individual measurement from Graham & Driver (2007a; red points), Laurikainen et al. (2010; blue points), Sani et al. (2011; green points), Vika et al. (2012; yellow points), Beifiori et al. (2012; gray points), Rusli (2013a; white points), and Läsker et al. (2014a; orange points). Black points are measurements obtained from the 1D fits presented in this work (using linearly sampled surface brightness profiles, along the major axis). In the top panel, the white histogram shows the distribution of $\log(n_{\text{sph}}) - \langle \log(n_{\text{sph}}) \rangle$ for all measurements, whereas the black histogram refers only to the measurements obtained by us. The (asymmetric) error bars σ_1 , σ_2 , and σ_3 enclose 38%, 78%, and 92% of the black histogram, respectively, corresponding to our quality flags 1, 2, and 3 given in Table 2 (see Section 4.2 for details). We consider these to be absolute upper limits to the uncertainty on our parameters given the care we have taken to minimize sources of systematic errors.

weighting scheme on the data points that constitute the surface brightness profile, although the use of a linearly and logarithmically sampled profile effectively represents a different weighting scheme. The all too often overlooked flaw with signal-to-noise ratio (S/N) based weighting schemes is that they immediately become biased weighting schemes when additional components are present but not modeled. For

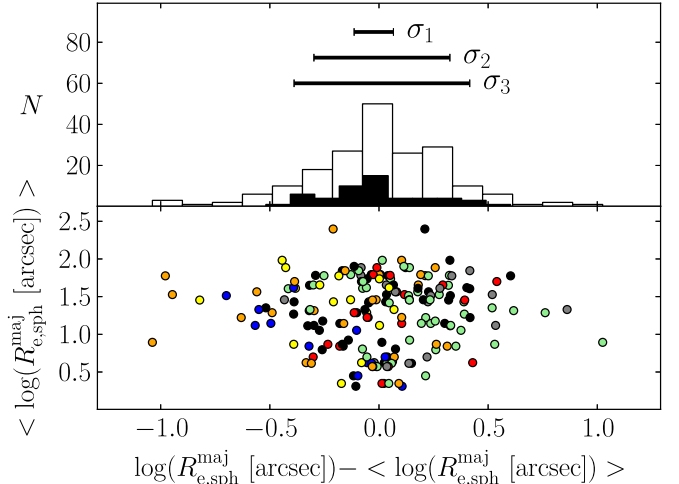


Figure 10. Bottom panel: 52 galaxies for which at least one measurement of the spheroid major-axis effective radius $R_{\text{e}}^{\text{maj}}$ is available from the literature (Table 3), in addition to that measured by us. The average (logarithmic) value ($\langle \log(R_{\text{e}}^{\text{maj}}) \rangle$) is plotted against the difference between (the logarithm of) the individual measurements of a galaxy and the average (logarithmic) value for that same galaxy. See Figure 9 for color description and explanation of the top panel.

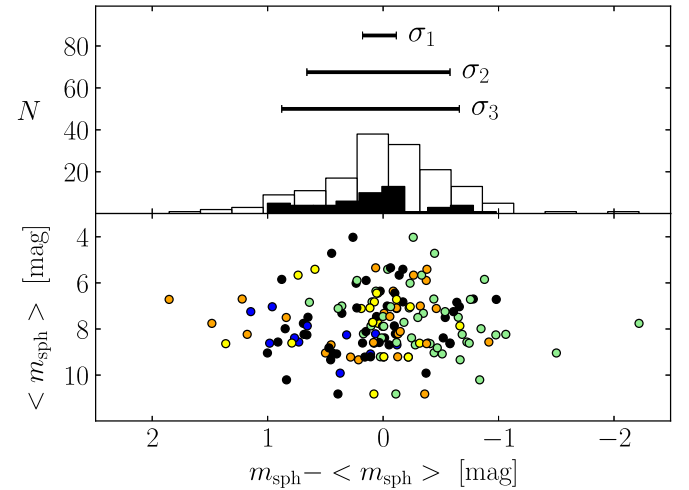


Figure 11. Bottom panel: 51 galaxies for which at least one measurement of the spheroid apparent magnitude m_{sph} —either in the K band or at $3.6\ \mu\text{m}$ —is available from the literature (Table 3), in addition to that measured by us. The $3.6\ \mu\text{m}$ magnitudes were converted into K -band magnitudes (see Section 4.2 for details). The average value ($\langle m_{\text{sph}} \rangle$) is plotted against the difference between the individual measurements of a galaxy and the average value for that same galaxy. See Figure 9 for color description and explanation of the top panel.

example, fitting only a Sérsic model to what is actually a nucleated elliptical galaxy immediately voids a S/N-based weighting scheme and results in Sérsic parameters that describe the spheroid less accurately than had no S/N-based weighting been used. While we have paid careful attention to the components in each galaxy, this is an issue that warrants the nonapplication of S/N-based weighting schemes. Overlooked partially depleted cores, or an incorrect PSF, can of course also result in S/N-weighted fitting schemes performing poorly because of the emphasis they place on matching the model to the inner data.

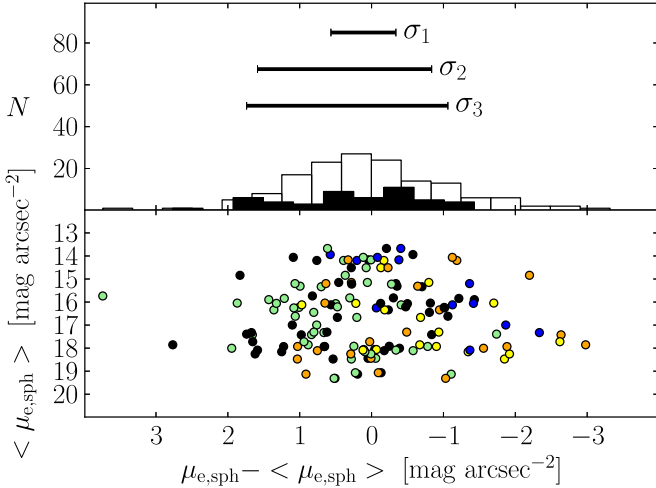


Figure 12. Bottom panel: 49 galaxies for which at least one measurement of the spheroid effective surface brightness $\mu_{e,sph}$ —either in the K band or at $3.6\ \mu m$ —is available from the literature (Table 3), in addition to that measured by us. The K -band magnitudes were converted into $3.6\ \mu m$ magnitudes (see Section 4.2 for details). The average value $\langle \mu_{e,sph} \rangle$ from all fits to a galaxy, not to be confused with the mean effective surface brightness within $R_{e,sph}$, is plotted against the difference between the individual measurements of a galaxy and the average value for that same galaxy. See Figure 9 for color description and explanation of the top panel.

Table 3
Summary of Previous Investigations of Black Hole Mass Scaling Relations

	GD07	S+11	V+12	B+12	L+14	This Work
Galaxies with successful fit	27	57	25	19	35	66
Wavelength	R -band	$3.6\ \mu m$	K -band	i -band	K -band	$3.6\ \mu m$
Decomposition	1D	2D	2D	2D	2D	1D & 2D
Nuclear components	masked	modeled	modeled	not treated	modeled	modeled/masked
Partially depleted cores	masked	masked	masked	not treated	masked	masked
Bars	excluded	modeled	modeled	excluded	modeled	modeled
Other components	no	no	no	no	yes	yes
Kinematics	no	no	no	no	no	yes

Note. GD07—Graham & Driver (2007a); S+11—Sani et al. (2011); V+12—Vika et al. (2012); B+12—Beifiori et al. (2012); L+14—Läsker et al. (2014a).

Table 4

Best-fit Parameters for the Spheroidal Component of IC 1459

Work	Model	$R_{e,sph}$ (arcsec)	n_{sph}
1D maj.	S-bul + m-c	63.1	6.6
1D equation	S-bul + m-c	57.3	7.0
2D	S-bul + m-c	87.5	8.3
S+11 2D	S-bul + G-n	61.1	6.0
R+13 1D equation	core-Sérsic	45.4	7.6
L+14 2D	S-bul + m-c	62.4	8.3

Note. Our results are shown in the upper portion of the table. See Section 5.1 for the legend key to the other authors listed in the lower portion of the table. See Table 2 for our associated surface brightnesses and magnitudes.

3.4. Smoothing Technique

Some nearby galaxies in our sample have very large apparent sizes, and for them we obtained surface brightness profiles more extended than 8 arcmin. This means that their outermost (significant) isophote corresponds to a projected galactic radius R of more than 240 times the FWHM of the instrumental PSF. Such a level of spatial resolution is

Table 5
Best-fit Parameters for the Spheroidal Component of IC 2560

Work	Model	$R_{e,sph}$ (arcsec)	n_{sph}
1D maj.	S-bul + e-d + F-bar + G-n	6.1	0.8
1D equation	S-bul + e-d + F-bar + G-n	4.5	0.6
S+11 2D	S-bul + e-d + G-n	27.5	2.0

Note. In their model, S+11 did not account for the bar component and thus overestimated the effective radius and the Sérsic index of the bulge.

Table 6
Best-fit Parameters for the Spheroidal Component of IC 4296

Work	Model	$R_{e,sph}$ (arcsec)	n_{sph}
1D maj.	S-bul + m-c	65.9	5.8
1D equation	S-bul + m-c	68.1	6.2
2D	S-bul + m-c	82.3	6.6
S+11 2D	S-bul + G-n	33.6	4.0
L+14 2D	S-bul + m-c	97.8	8.2

Note. S+11 obtained a small effective radius and Sérsic index because they fit a nuclear component rather than masking the core.

Table 7
Best-fit Parameters for the Spheroidal Component of M31

Work	Model	$R_{e,sph}$ (arcsec)	n_{sph}
1D maj.	S-bul + e-d + F-bar	418.6	2.2
1D equation	S-bul + e-d + F-bar	173.6	1.3

Table 8
Best-fit Parameters for the Spheroidal Component of M49

Work	Model	$R_{e,sph}$ (arcsec)	n_{sph}
1D maj.	S-bul + m-c	190.2	6.6
1D equation	S-bul + m-c	135.3	5.4
2D	S-bul + m-c	151.9	5.5
R+13 1D equation	core-Sérsic	199.0	5.6

Note. The equivalent-axis effective radius estimated by R+13 is larger than that measured by us. Since their circularized light profile is almost three times more extended than ours, it is possible that their best-fit model required a larger R_e to account for the galaxy intracluster halo light.

Table 9
Best-fit Parameters for the Spheroidal Component of M59

Work	Model	$R_{\text{e,sph}}$ (arcsec)	n_{sph}
1D maj.	S-bul + m-n + e-id	48.0	5.5
1D equation	S-bul + m-n + e-id	90.9	8.8
S+11 2D	S-bul	70.1	5.0
V+12 2D	S-bul + m-c	54.7	5.7

Table 10
Best-fit Parameters for the Spheroidal Component of M64

Work	Model	$R_{\text{e,sph}}$ (arcsec)	n_{sph}
1D maj.	S-bul + e-d + F-bar + S-id	3.8	0.8
1D equation	S-bul + e-d + F-bar + S-id	4.3	1.4
B+12 2D	S-bul + e-d	5.0	1.5

Table 11
Best-fit Parameters for the Spheroidal Component of M81

Work	Model	$R_{\text{e,sph}}$ (arcsec)	n_{sph}
1D maj.	S-bul + e-d	31.0	1.7
1D equation	S-bul + e-d	33.2	2.1
GD07 1D maj.	S-bul + e-d	68.1	3.3
S+11 2D	S-bul + e-d + G-n	127.3	3.0
B+12 2D	S-bul + e-d	50.0	2.6

Note. GD07 and B+12 obtained estimates of the effective radius larger than ours by a factor of two. This is not particularly surprising, given the complicated surface brightness distribution of this galaxy. The large measurement of the effective radius reported by S+11 is the most discrepant, but the reasons for this are unclear.

Table 12
Best-fit Parameters for the Spheroidal Component of M84

Work	Model	$R_{\text{e,sph}}$ (arcsec)	n_{sph}
1D maj.	S-bul + m-c	101.6	7.8
1D equation	S-bul + m-c	129.8	7.9
2D	S-bul + m-c	181.8	8.4
GD07 1D maj.	S-bul	75.1	5.6
S+11 2D	S-bul + G-n	105.9	7.0
V+12 2D	S-bul + m-c	28.7	3.5
B+12 2D	S-bul	63.6	4.1
R+13 1D equation	core-Sérsic	126.2	7.1
L+14 2D	S-bul + m-c	139.0	8.3

Note. B+12 did not mask the core and thus underestimated the effective radius and the Sérsic index. V+12 used the same model as R+13, L+14, and us, but the smaller radial extent of their data led them to underestimate the effective radius and the Sérsic index.

unnecessary for the purposes of our analysis, and, especially in the case of a clumpy star-forming galaxy, it results in a “noisy” surface brightness profile. Moreover, in the case of a linearly sampled light profile, it significantly prolongs the computational time of the fitting routine (because, at each iteration, the PSF convolution is performed numerically on a large array). To overcome this problem, we introduced a method to which we refer as the “smoothing technique.” This method was applied to the galaxies M31, M81, NGC 4945, and NGC 5128. For each

Table 13
Best-fit Parameters for the Spheroidal Component of M87

Work	Model	$R_{\text{e,sph}}$ (arcsec)	n_{sph}
1D maj.	S-bul + m-c	203.9	10.0
1D equation	S-bul + m-c	87.1	5.9
2D	S-bul + m-c	88.3	4.3
GD07 1D maj.	S-bul	...	6.9
S+11 2D	S-bul + G-n	99.5	4.0
V+12 2D	S-bul + m-c	34.6	2.4
R+13 1D equation	core-Sérsic	180.9	8.9
L+14 2D	S-bul + m-c	122.0	5.6

Note. The equivalent-axis fit of R+13 returns the largest values for $R_{\text{e,sph}}$ and n_{sph} . As in the case of M49, since their circularized light profile is almost three times more extended than ours, it is possible that their best-fit model required a larger R_{e} to account for the extra intracluster halo light. V+12 obtained the smallest estimates of $R_{\text{e,sph}}$ and n_{sph} because of the small radial extent of their data.

Table 14
Best-fit Parameters for the Spheroidal Component of M89

Work	Model	$R_{\text{e,sph}}$ (arcsec)	n_{sph}
1D maj.	S-bul + e-halo	29.0	4.6
1D equation	S-bul + e-halo	28.2	5.1
S+11 2D	S-bul + e-d	24.3	4.0
V+12 2D	S-bul	16.7	3.6
B+12 2D	S-bul	45.2	4.3
R+13 1D equation	S-bul + S-halo	19.8	3.8

Table 15
Best-fit Parameters for the Spheroidal Component of M94

Work	Model	$R_{\text{e,sph}}$ (arcsec)	n_{sph}
1D maj.	S-bul + e-d + F-bar	11.4	0.9
1D equation	S-bul + e-d + F-bar	8.4	1.1

Table 16
Best-fit Parameters for the Spheroidal Component of M96

Work	Model	$R_{\text{e,sph}}$ (arcsec)	n_{sph}
1D maj.	S-bul + e-d + F-bar + S-id	7.5	1.5
1D equation	S-bul + e-d + F-bar + S-id	5.3	1.3
2D	S-bul + e-d + G-bar + G-id	8.3	2.0
S+11 2D	S-bul + e-d + G-bar	45.6	1.0

Note. The bulge effective radius obtained by S+11 largely exceeds our estimates because their galaxy decomposition does not account for the inner component embedded in the bulge ($R_{\text{maj}} \lesssim 25''$).

of these galaxies, we took the image mosaic and convolved it with a Gaussian filter whose FWHM was larger than the FWHM of the instrumental PSF. We then ran ellipse on the convolved image and extracted “linearly sampled” and “logarithmically sampled” surface brightness profiles. For the “linearly sampled” profiles, we set the radial step between contiguous isophotes to be comparable to the FWHM of the smoothing Gaussian filter. Doing so, we reduced the number of fitted isophotes and also produced smoother surface brightness

Table 17
Best-fit Parameters for the Spheroidal Component of M104

Work	Model	$R_{\text{e,sph}}$ (arcsec)	n_{sph}
1D maj.	S-bul + e-d + F-bar + m-c	11.0	5.8
1D equation	S-bul + e-d + F-bar + m-c	19.6	3.7
S+11 2D	S-bul + e-d + G-bar + G-n	66.1	1.5

Note. The bulge Sérsic index obtained by S+11 is smaller than our estimates because they fit an additional nuclear component.

Table 18
Best-fit Parameters for the Spheroidal Component of M105

Work	Model	$R_{\text{e,sph}}$ (arcsec)	n_{sph}
1D maj.	S-bul + m-c	57.2	5.2
1D equation	S-bul + m-c	50.9	5.3
2D	S-bul + m-c	73.6	7.0
GD07 1D maj.	S-bul	58.3	4.3
S+11 2D	S-bul	46.0	5.0
R+13 1D equation	core-Sérsic	55.1	5.8
L+14 2D	S-bul + m-c	96.3	9.3

Note. L+14 obtained the largest values of $R_{\text{e,sph}}$ and n_{sph} , possibly owing to incorrect sky subtraction (see the “upturn” of the three outermost data points in their Figure 21).

Table 19
Best-fit Parameters for the Spheroidal Component of M106

Work	Model	$R_{\text{e,sph}}$ (arcsec)	n_{sph}
1D maj.	S-bul + e-d	15.3	2.0
1D equation	S-bul + e-d	8.3	1.2
GD07 1D maj.	S-bul + e-d	14.9	2.0
S+11 2D	S-bul + e-d + G-n	111.7	2.0
V+12 2D (1)	S-bul + e-d + PSF-n	17.0	3.5
V+12 2D (2)	S-bul + e-d + PSF-n + S-bar	6.3	2.2
L+14 2D	S-bul + e-d + PSF-n + e-id + S-bar + spiral arms	6.3	3.3

Note. The bulge effective radius obtained by S+11 largely exceeds all the other estimates, behavior noted also in NGC 3031.

Table 20
Best-fit Parameters for the Spheroidal Component of NGC 0524

Work	Model	$R_{\text{e,sph}}$ (arcsec)	n_{sph}
1D maj.	S-bul + e-d + G-r	6.0	1.1
1D equation	S-bul + e-d + G-r	5.8	1.1
L+10 2D	S-bul + e-d + 2 F-l	8.9	2.7
S+11 2D	S-bul + e-d	26.8	3.0

Note. S+11 obtained the largest value of the effective radius because their two-component model does not account for the ring. Both L+10 and S+11 estimated a Sérsic index of ~ 3 , three times larger than the value obtained by us.

profiles. Before the software fit a smoothed light profile, the model to be fit was convolved twice: the first time to account for PSF effects, and the second time to account for the artificial Gaussian smoothing applied to the image mosaic.

Table 21
Best-fit Parameters for the Spheroidal Component of NGC 0821

Work	Model	$R_{\text{e,sph}}$ (arcsec)	n_{sph}
1D maj.	S-bul + e-id + PSF-n	36.8	5.4
1D equation	S-bul + e-id + PSF-n	20.7	6.0
2D	S-bul + e-id + m-n	33.8	2.5
GD07 1D maj.	S-bul	44.1	4.0
S+11 2D	S-bul	63.6	7.0
B+12 2D	S-bul	111.3	7.7
L+14 2D	S-bul + e-d + S-halo	3.8	3.1

Note. L+14 obtained a tiny estimate of the spheroid effective radius and a small Sérsic index because they failed to identify the extent of the intermediate-scale disk. Inaccurate sky subtraction could be the reason why B+12 obtained a large estimate of the effective radius. We could not obtain a successful 2D model that included a nuclear component; therefore, we opted for masking the nuclear region of the galaxy. This resulted in a significantly lower Sérsic index, which we consider underestimated.

Table 22
Best-fit Parameters for the Spheroidal Component of NGC 1023

Work	Model	$R_{\text{e,sph}}$ (arcsec)	n_{sph}
1D maj.	S-bul + e-d + F-bar	9.2	2.1
1D equation	S-bul + e-d + F-bar	7.4	2.0
2D	S-bul + e-d + G-bar	6.6	2.3
GD07 1D maj.	S-bul + e-d	17.7	2.0
S+11 2D	S-bul + e-d + G-bar	24.0	3.0
L+14 2D	S-bul + e-d + S-bar	9.6	3.1

Note. S+11 obtained the largest value of the bulge effective radius, although they accounted for the bar in their model.

Table 23
Best-fit Parameters for the Spheroidal Component of NGC 1300

Work	Model	$R_{\text{e,sph}}$ (arcsec)	n_{sph}
1D maj.	S-bul + e-(d+bar) + S-id	9.9	3.8
1D equation	S-bul + e-(d+bar) + S-id	8.1	3.6
S+11 2D	S-bul + e-d	85.4	3.0
L+14 2D	S-bul + e-d + PSF-n + e-id + S-bar + spiral arms	10.4	4.3

Note. S+11 dramatically overestimated the bulge effective radius mainly because their model does not account for the large-scale bar.

Table 24
Best-fit Parameters for the Spheroidal Component of NGC 1316

Work	Model	$R_{\text{e,sph}}$ (arcsec)	n_{sph}
1D maj.	S-bul + e-d + F-bar + 2 G-r + G-n	21.5	2.0
1D equation	S-bul + e-d + F-bar + 2 G-r + G-n	15.9	1.8
S+11 2D	S-bul + e-d + G-n	93.0	5.0

Note. S+11 overestimated the bulge effective radius and Sérsic index because their model does not take into account the bar.

3.5. Identifying and Modeling Subcomponents

In this section we give a general overview of the guidelines that we followed to identify and model the subcomponents that

Table 25

Best-fit Parameters for the Spheroidal Component of NGC 1332

Work	Model	$R_{\text{e,sph}}$ (arcsec)	n_{sph}
1D maj.	S-bul + S-id + m-c	34.7	5.1
1D equation	S-bul + S-id + m-c	18.0	3.7

Table 26

Best-fit Parameters for the Spheroidal Component of NGC 1374

Work	Model	$R_{\text{e,sph}}$ (arcsec)	n_{sph}
1D maj.	S-bul + G-n	25.6	3.7
1D equation	S-bul + G-n	24.8	4.1
2D	S-bul + m-n	25.2	3.7

Table 27

Best-fit Parameters for the Spheroidal Component of NGC 1399

Work	Model	$R_{\text{e,sph}}$ (arcsec)	n_{sph}
1D maj.	S-bul + m-c + e-id	405.2	10.0
1D equation	S-bul + m-c + e-id	338.1	10.0
GD07 1D maj.	S-bul	...	16.8
R+13 1D equation	core-Sérsic + (S+e)-halo	36.2	7.4
L+14 2D	S-bul + m-c	154.0	11.1

Note. R+13 used a combination of a Sérsic + exponential profile to model the galaxy's halo and obtained the smallest estimate of the effective radius, one that is at odds with the fact that central cluster galaxies typically have large sizes.

Table 28

Best-fit Parameters for the Spheroidal Component of NGC 2273

Work	Model	$R_{\text{e,sph}}$ (arcsec)	n_{sph}
1D maj.	S-bul + e-d + F-bar	1.6	2.1
1D equation	S-bul + e-d + F-bar	1.9	2.7
L+10 2D	S-bul + e-d + F-bar	2.6	1.8

Table 29

Best-fit Parameters for the Spheroidal Component of NGC 2549

Work	Model	$R_{\text{e,sph}}$ (arcsec)	n_{sph}
1D maj.	S-bul + e-d + F-bar + F-id	6.1	2.3
1D equation	S-bul + e-d + F-bar + F-id	3.1	1.5
2D	S-bul + e-d + G-bar + G-id	5.6	2.1
S+11 2D	S-bul + e-d	11.6	7.0

Note. The model of S+11 does not account for the large-scale bar and therefore largely overestimates the bulge Sérsic index.

constitute our galaxies. However, given the level of accuracy and detail to which each galaxy decomposition has been performed in our analysis, it is hard to encompass all aspects of this matter in a few paragraphs. The modeling of each galaxy represented a particular and original problem, and we remand the reader to Section 5.1, where we provide individual descriptions of the galaxies that we analyzed.

Table 30

Best-fit Parameters for the Spheroidal Component of NGC 2778

Work	Model	$R_{\text{e,sph}}$ (arcsec)	n_{sph}
1D maj.	S-bul + e-d + F-bar + PSF-n	2.3	1.3
1D equation	S-bul + e-d + F-bar + PSF-n	2.2	1.2
GD07 1D maj.	S-bul + e-d	2.3	1.6
S+11 2D	S-bul + e-d	2.5	2.5
V+12 2D	S-bul + e-d	1.5	2.7
L+14 2D	S-bul + e-d + S-bar	2.8	4.0

Table 31

Best-fit Parameters for the Spheroidal Component of NGC 2787

Work	Model	$R_{\text{e,sph}}$ (arcsec)	n_{sph}
1D maj.	S-bul + e-d + F-bar + F-id + PSF-nucleus	4.8	1.1
1D equation	S-bul + e-d + F-bar + F-id + PSF-nucleus	3.3	1.3
GD07 1D maj.	S-bul + e-d	4.6	2.0
L+10 2D	S-bul + e-d + F-bar + F-l	4.0	1.3
S+11 2D	S-bul + e-d + G-bar + G-n	15.7	3.0
L+14 2D	S-bul + trunc. e-d + trunc. S-bar + S-id + PSF-n	14.3	2.8

Note. S+11 found larger estimates of the effective radius and Sérsic index because they did not account for the inner disk. L+14 also reported a larger effective radius and Sérsic index because they employed a truncated exponential disk and truncated Sérsic bar in their galaxy model.

Table 32

Best-fit Parameters for the Spheroidal Component of NGC 2974

Work	Model	$R_{\text{e,sph}}$ (arcsec)	n_{sph}
1D maj.	S-bul + e-d + F-bar + G-n + G-r	8.3	1.4
1D equation	S-bul + e-d + F-bar + G-n + G-r	6.9	1.2
2D	S-bul + e-d + G-bar + m-n	10.6	1.3
S+11 2D	S-bul + G-n	27.2	3.0

Note. The model of S+11 does not account for the large-scale disk and thus overestimates the bulge effective radius and Sérsic index.

Table 33

Best-fit Parameters for the Spheroidal Component of NGC 2974

Work	Model	$R_{\text{e,sph}}$ (arcsec)	n_{sph}
1D maj.	S-bul + F-(bar+d) + G-n	6.8	1.3
1D equation	S-bul + F-(bar+d) + G-n	4.3	1.1
S+11 2D	S-bul + e-d + G-bar + G-n	74.1	2.0

Note. It is not clear why S+11 obtained a dramatically larger bulge effective radius.

As stressed in Section 1, our investigation is primarily focused on the central spheroidal components of galaxies. The objects in our sample are either early-type galaxies (**elliptical +lenticular**) or “early-type spiral” galaxies (i.e., the morphological classification of our spiral galaxies is within **Sa–Sc**, with the only exception of NGC 4945, which is classified as **Scd**); therefore—by definition—they all have a bulge/spheroidal component, unlike “late-type spiral” galaxies that can be

Table 34

Best-fit Parameters for the Spheroidal Component of NGC 3091

Work	Model	$R_{\text{e,sph}}$ (arcsec)	n_{sph}
1D maj.	S-bul + m-c	100.5	7.6
1D equation	S-bul + m-c	51.2	6.6
2D	S-bul + m-c	67.1	6.7
R+13 1D Equation	core-Sérsic	91.0	9.3

Table 35

Best-fit Parameters for the Spheroidal Component of NGC 3115

Work	Model	$R_{\text{e,sph}}$ (arcsec)	n_{sph}
1D maj.	S-bul + e-d + G-r	43.6	4.4
1D equation	S-bul + e-d + G-r	34.4	5.1
S+11 2D	S-bul + e-d	27.1	3.0
L+14 2D	S-bul + e-d + S-halo	3.9	3.0

Note. L+14 used a model with a bulge encased in a larger disk and attributed the excess of light at large radii to a halo. In doing so, they obviously obtained a smaller bulge effective radius.

Table 36

Best-fit Parameters for the Spheroidal Component of NGC 3227

Work	Model	$R_{\text{e,sph}}$ (arcsec)	n_{sph}
1D maj.	S-bul + e-d + F-bar + G-n	8.1	1.7
1D equation	S-bul + e-d + [F-bar] + G-n	4.6	1.1
L+10 2D	S-bul + e-d + F-bar	1.8	2.2
S+11 2D	S-bul + e-d	82.9	4.0
L+14 2D	S-bul + e-d + S-bar	0.7	4.1

Note. The models of L+10 and L+14 do not account for the bright nuclear component and thus underestimate the bulge effective radius and overestimate the bulge Sérsic index. The bulge effective radius obtained by S+11 is larger because they did not model the bar.

Table 37

Best-fit Parameters for the Spheroidal Component of NGC 3245

Work	Model	$R_{\text{e,sph}}$ (arcsec)	n_{sph}
1D maj.	S-bul + e-d + F-id	4.4	2.9
1D equation	S-bul + e-d + F-id	2.4	1.7
2D	S-bul + e-d + G-id	1.9	1.8
GD07 1D maj.	S-bul + e-d	11.3	4.3
L+10 2D	S-bul + e-(d+l) + F-id	4.0	2.4
S+11 2D	S-bul + e-d	4.6	2.5
V+12 2D	S-bul + e-d	3.5	2.6
B+12 2D	S-bul + e-d	4.0	1.6
L+14 2D	S-bul + e-d + S-bar	2.0	1.6

bulgeless (e.g., NGC 300). We modeled spheroids/bulges with a Sérsic profile, without attempting to distinguish between classical and pseudobulges.

Disk were usually fit with the exponential model, although in the case of highly inclined or edge-on systems we preferred using an $n < 1$ Sérsic function. Pastrav et al. (2013a, 2013b) showed that, owing to projection effects, their simulated images of inclined galaxy disks are better fit by a Sérsic

Table 38

Best-fit Parameters for the Spheroidal Component of NGC 3377

Work	Model	$R_{\text{e,sph}}$ (arcsec)	n_{sph}
1D maj.	S-bul + 2 e-id	61.8	7.7
1D equation	S-bul + 2 e-id	91.7	9.2
2D	S-bul + e-id + m-n	71.8	3.7
GD07 1D maj.	S-bul	44.1	3.0
S+11 2D	S-bul	55.2	6.0
B+12 2D	S-bul	43.5	3.5
L+14 2D	S-bul + e-id + e-d + S-halo	10.1	6.0

Note. L+14 obtained the smallest estimate of the effective radius because they oversubtracted a halo. In our 2D fit, we were not successful in modeling the nuclear disk and opted for masking the nuclear region of the galaxy. Such a 2D model resulted in a significantly lower Sérsic index, which we trust being underestimated.

Table 39

Best-fit Parameters for the Spheroidal Component of NGC 3384

Work	Model	$R_{\text{e,sph}}$ (arcsec)	n_{sph}
1D maj.	S-bul + e-d + F-bar + m-n	5.5	1.6
1D equation	S-bul + e-d + F-bar + m-n	5.6	1.8
GD07 1D maj.	S-bul + e-d	2.5	1.7
L+10 2D	S-bul + e-d + 2 F-bar	4.0	1.5
S+11 2D	S-bul + e-d + G-bar	4.4	2.5
B+12 2D	S-bul + e-d	8.3	2.3
L+14 2D	S-bul + e-d + 2 S-id + S-bar	5.9	2.5

Table 40

Best-fit Parameters for the Spheroidal Component of NGC 3393

Work	Model	$R_{\text{e,sph}}$ (arcsec)	n_{sph}
1D maj.	S-bul + e-d + F-bar	1.4	3.4
1D equation	S-bul + e-d + F-bar	1.4	2.6
2D	S-bul + e-d + G-bar	1.2	1.9

Table 41

Best-fit Parameters for the Spheroidal Component of NGC 3414

Work	Model	$R_{\text{e,sph}}$ (arcsec)	n_{sph}
1D maj.	S-bul + e-id + G-r	28.0	4.8
1D equation	S-bul + e-id + G-r	25.5	4.5
L+10 2D	S-bul + e-d + F-bar	5.0	2.6

Note. L+10 used a model with a large-scale exponential disk; thus, they obtained a smaller bulge effective radius and Sérsic index.

Table 42

Best-fit Parameters for the Spheroidal Component of NGC 3489

Work	Model	$R_{\text{e,sph}}$ (arcsec)	n_{sph}
1D maj.	S-bul + e-d + F-bar	2.2	1.5
1D equation	S-bul + e-d + F-bar	1.7	1.3
2D	S-bul + e-d + G-bar	1.7	2.1
L+10 2D	S-bul + e-d + F-bar	2.0	2.1
S+11 2D	S-bul + e-d	4.6	1.5

Table 43

Work	Model	$R_{\text{e,sph}}$ (arcsec)	n_{sph}
1D maj.	S-bul + e-id	105.0	5.2
1D equation	S-bul + e-id	86.3	6.3
S+11 2D	S-bul + e-d	15.5	2.5

Note. S+11 2D obtained smaller estimates of the effective radius and Sérsic index because they included a large-scale disk in their model.

Table 44

Work	Model	$R_{\text{e,sph}}$ (arcsec)	n_{sph}
1D maj.	S-bul + e-id	69.3	5.5
1D equation	S-bul + e-id	65.5	5.6
2D	S-bul + e-id	60.0	5.3
L+10 2D	S-bul + e-d	6.5	1.5
S+11 2D	S-bul + G-n	44.6	5.0
B+12 2D	S-bul	56.3	4.7

Note. L+10 obtained the smallest estimates of the effective radius and Sérsic index because they included a large-scale disk in their model.

Table 45

Work	Model	$R_{\text{e,sph}}$ (arcsec)	n_{sph}
1D maj.	S-bul	47.5	5.2
1D equation	S-bul	43.4	5.7
2D	S-bul	62.0	7.0
S+11 2D	S-bul	56.4	6.0
B+12 2D	S-bul	182.2	9.0
R+13 1D equation	core-Sérsic	56.9	6.3
L+14 2D	S-bul	48.9	6.6

Note. B+12 obtained the largest estimates of the effective radius and Sérsic index, possibly owing to incorrect sky subtraction.

Table 46

Work	Model	$R_{\text{e,sph}}$ (arcsec)	n_{sph}
1D maj.	S-bul + F-l + m-c	100.7	8.1
1D equation	S-bul + F-l + m-c	73.6	8.2
R+13 1D equation	core-Sérsic	58.8	6.3

function with $n < 1$ than by a pure exponential model. The inclined, embedded disks of some “elliptical” galaxies were described with Ferrer functions, rather than an $n < 1$ Sérsic function. This choice was partly motivated by the fact that a Sérsic + Ferrer model is less degenerate than a Sérsic + Sérsic model, since the Sérsic profile can assume any concave ($n > 1$) or convex ($n < 1$) curvature, whereas the Ferrer profile can only have a negative curvature as required for an inclined disk.

The presence of large-scale disks, such as those of lenticular and spiral galaxies, was known a priori from the galaxy

Table 47

Best-fit Parameters for the Spheroidal Component of NGC 3998

Work	Model	$R_{\text{e,sph}}$ (arcsec)	n_{sph}
1D maj.	S-bul + e-d + F-bar + F-l + G-n + G-r	5.8	1.2
1D equation	S-bul + e-d + F-bar + F-l + G-n + G-r	4.8	1.3
L+10 2D	S-bul + e-d + F-bar + F-l	5.0	2.0
S+11 2D	S-bul + e-d + G-bar + G-n	4.7	1.5
B+12 2D	S-bul + e-d	5.7	2.3
L+14 2D	S-bul + trunc. e-d + PSF-n + S-bar + S-id	2.0	1.1

Table 48

Best-fit Parameters for the Spheroidal Component of NGC 4026

Work	Model	$R_{\text{e,sph}}$ (arcsec)	n_{sph}
1D maj.	S-bul + e-d + F-bar + S-id	3.4	2.4
1D equation	S-bul + e-d + F-bar + S-id	6.3	2.1
S+11 2D	S-bul + e-d	11.4	3.5

Note. S+11 obtained larger estimates of the bulge effective radius and Sérsic index because they did not model the bar.

Table 49

Best-fit Parameters for the Spheroidal Component of NGC 4151

Work	Model	$R_{\text{e,sph}}$ (arcsec)	n_{sph}
1D maj.	S-bul + e-d + S-bar [+ m-n]	7.6	1.4
1D equation	S-bul + e-d + S-bar [+ m-n]	6.8	1.9
S+11 2D	S-bul + e-d + G-n	5.4	3.5

Table 50

Best-fit Parameters for the Spheroidal Component of NGC 4261

Work	Model	$R_{\text{e,sph}}$ (arcsec)	n_{sph}
1D maj.	S-bul + m-c + F-id	52.6	4.7
1D equation	S-bul + m-c + F-id	47.3	4.3
2D	S-bul + m-c + e-id	50.4	4.4
GD07 1D maj.	S-bul	88.6	7.3
S+11 2D	S-bul + e-d + G-n	22.6	4.0
V+12 2D	S-bul + m-c	24.2	3.5
B+12 2D	S-bul	48.8	4.3
R+13 1D equation	core-Sérsic	77.1	6.3
L+14 2D	S-bul + m-c	68.4	6.5

Note. S+11 found the smallest estimate of the effective radius because they added a large-scale disk to their model. V+12 obtained a small estimate of the effective radius because of the limited radial extent of their data.

Table 51

Best-fit Parameters for the Spheroidal Component of NGC 4291

Work	Model	$R_{\text{e,sph}}$ (arcsec)	n_{sph}
1D maj.	S-bul + m-c	15.0	4.2
1D equation	S-bul + m-c	15.4	5.9
2D	S-bul + m-c	20.8	7.7
GD07 1D maj.	S-bul	14.8	4.0
R+13 1D equation	core-Sérsic	15.3	5.6
L+14 2D	S-bul + m-c	21.3	8.6

Table 52

Best-fit Parameters for the Spheroidal Component of NGC 4388

Work	Model	$R_{\text{e,sph}}$ (arcsec)	n_{sph}
1D maj.	S-bul + e-d + F-bar + G-n	4.6	0.6
1D equation	S-bul + e-d + F-bar + G-n	4.2	1.3

Table 53

Best-fit Parameters for the Spheroidal Component of NGC 4459

Work	Model	$R_{\text{e,sph}}$ (arcsec)	n_{sph}
1D maj.	S-bul + e-d + G-n	18.4	3.1
1D equation	S-bul + e-d + G-n	13.0	2.6
L+10 2D	S-bul + e-d + F-l	7.0	3.0
S+11 2D	S-bul + e-d	10.3	2.5
V+12 2D	S-bul + M-n	25.0	3.9
B+12 2D	S-bul	155.2	7.4

Note. B+12 did not model the large-scale disk and thus overestimated the bulge effective radius and Sérsic index.

Table 54

Best-fit Parameters for the Spheroidal Component of NGC 4473

Work	Model	$R_{\text{e,sph}}$ (arcsec)	n_{sph}
1D maj.	S-bul + e-id + G-n	45.9	2.3
1D equation	S-bul + e-id + G-n	36.9	2.9
GD07 1D maj.	S-bul	39.6	2.7
S+11 2D	S-bul	49.3	7.0
V+12 2D	S-bul + m-c	21.3	4.3
B+12 2D	S-bul + e-d	10.6	2.2
L+14 2D	S-bul	27.9	5.1

Note. B+12 obtained the smallest estimates of the effective radius and Sérsic index because they included a large-scale disk in their model.

Table 55

Best-fit Parameters for the Spheroidal Component of NGC 4564

Work	Model	$R_{\text{e,sph}}$ (arcsec)	n_{sph}
1D maj.	S-bul + e-d + F-l	5.0	2.6
1D equation	S-bul + e-d + F-l	6.0	3.0
GD07 1D maj.	S-bul + e-d	4.3	3.2
S+11 2D	S-bul + e-d	25.0	7.0
V+12 2D	S-bul + e-d	3.0	3.7

Note. The most *discrepant* results are obtained by S+11, although they used the same model as GD07 and V+12.

morphological classification (as listed on NED), although some of them were *reclassified* by us as having intermediate-scale embedded disks. These were identified in a number of different ways. If highly inclined, they can obviously be spotted from the galaxy image or the unsharp mask. Local maxima in the ellipticity and fourth harmonic profiles can provide footprints of less obvious embedded disks. In particular, the ellipticity profile helps distinguish embedded disks from large-scale disks. Galaxy disks typically have fixed ellipticity, reflecting their inclination to our line of sight. On the other hand, spheroids can have their ellipticities varying with radius, but

Table 56

Best-fit Parameters for the Spheroidal Component of NGC 4596

Work	Model	$R_{\text{e,sph}}$ (arcsec)	n_{sph}
1D maj.	S-bul + e-d + F-bar + G-r + S-id	6.6	2.7
1D equation	S-bul + e-d + F-bar + G-r + S-id	9.0	3.0
L+10 2D	S-bul + e-d + F-bar + F-l	2.8	1.4
S+11 2D	S-bul + e-d + G-bar	28.0	3.0
V+12 2D	S-bul + e-d + S-bar	13.2	3.6
B+12 2D	S-bul + e-d	44.9	4.4

Note. B+12 fit neither the bar nor the inner disk and obtained the largest estimates of the bulge effective radius and Sérsic index. The models of S+11 and V+12 do not account for the inner disk and thus result in larger estimates of the bulge effective radius.

Table 57

Best-fit Parameters for the Spheroidal Component of NGC 4697

Work	Model	$R_{\text{e,sph}}$ (arcsec)	n_{sph}
1D maj.	S-bul + 2 S-id	239.3	7.2
1D equation	S-bul + 2 S-id	226.4	6.7
2D	S-bul + e-id	121.4	5.0
GD07 1D maj.	S-bul	—	4.0
S+11 2D	S-bul	100.5	5.0
V+12 (1) 2D	S-bul	39.1	3.8
V+12 (2) 2D	S-bul + e-d	10.0	2.9
L+14 2D	S-bul + e-d + PSF-n + S-halo	6.3	2.1

Note. In both their models, V+12 underestimated the effective radius and the Sérsic index because of the small radial range of their data. In an effort to model the curved light profile, L+14 included a large-scale disk plus a halo and thus underestimated the spheroid effective radius and the Sérsic index.

Table 58

Best-fit Parameters for the Spheroidal Component of NGC 4889

Work	Model	$R_{\text{e,sph}}$ (arcsec)	n_{sph}
1D maj.	S-bul + m-c	119.7	8.1
1D equation	S-bul + m-c	60.8	6.8
2D	S-bul + m-c	104.3	7.8
R+13 1D equation	core-Sérsic	169.2	9.8

Table 59

Best-fit Parameters for the Spheroidal Component of NGC 4945

Work	Model	$R_{\text{e,sph}}$ (arcsec)	n_{sph}
1D maj.	S-bul + e-d	13.9	1.4
1D equation	S-bul + e-d	9.5	1.7
2D	S-bul + e-d	16.2	0.8

they are usually rounder than inclined disks; thus, their average ellipticities are lower than those of inclined disks. If the ellipticity profile of a galaxy increases with radius, this can be ascribed to an inclined disk that becomes progressively more important over the spheroid, whereas a radial decrease of ellipticity signifies the opposite case. Therefore, in a situation where a disk is identified from the galaxy image, but its extent

Table 60

Best-fit Parameters for the Spheroidal Component of NGC 5077

Work	Model	$R_{\text{e,sph}}$ (arcsec)	n_{sph}
1D maj.	S-bul + m-c	23.5	4.2
1D equation	S-bul + m-c	23.0	5.7
2D	S-bul + m-c	30.5	6.8
S+11 2D	S-bul + G-n	29.2	6.0

Table 61

Best-fit Parameters for the Spheroidal Component of NGC 5128

Work	Model	$R_{\text{e,sph}}$ (arcsec)	n_{sph}
1D maj.	S-bul + e-halo + G-n	61.3	1.2
1D equation	S-bul + e-halo + G-n	60.8	2.2
S+11 2D	S-bul + e-d + G-n	103.6	3.5

Table 62

Best-fit Parameters for the Spheroidal Component of NGC 5576

Work	Model	$R_{\text{e,sph}}$ (arcsec)	n_{sph}
1D maj.	S-bul	61.5	3.3
1D equation	S-bul	49.3	3.7
2D	S-bul	45.9	8.3
S+11 2D	S-bul	34.3	7.0
V+12 2D	S-bul	16.9	5.1
B+12 2D	S-bul	77.6	8.7

Note. The results obtained by **S+11** and **B+12** agree best with the results from our 2D model, in which we did not mask the inner region of the galaxy. The small radial extent of the data used by **V+12** led them to underestimate the effective radius.

Table 63

Best-fit Parameters for the Spheroidal Component of NGC 5845

Work	Model	$R_{\text{e,sph}}$ (arcsec)	n_{sph}
1D maj.	S-bul + e-d	3.6	2.5
1D equation	S-bul + e-d	3.1	2.3
2D	S-bul + e-d	2.8	2.4
GD07 1D maj.	S-bul	4.1	3.2
S+11 2D	S-bul	3.7	3.0
V+12 2D	S-bul	3.5	2.6
B+12 2D	S-bul	4.1	3.5
L+14 2D	S-bul	3.5	2.8

(large or intermediate scale) is ambiguous, the shape of the ellipticity profile can be decisive. Another way to establish the presence of an embedded disk is to look at the velocity map of a galaxy, following the approach of Arnold et al. (2014). A local angular momentum decrease with increasing radius is indicative of an intermediate-scale disk that fades toward larger radii. Savorgnan & Graham (2015a) extensively discuss the topic of galaxies with intermediate-scale disks and show that, when these disks are misclassified and modeled as large-scale disks, the luminosity of the spheroidal component is underestimated, which makes these galaxies falsely appear as

Table 64

Best-fit Parameters for the Spheroidal Component of NGC 5846

Work	Model	$R_{\text{e,sph}}$ (arcsec)	n_{sph}
1D maj.	S-bul + m-c	105.1	6.4
1D equation	S-bul + m-c	83.4	5.7
2D	S-bul + m-c	85.1	5.2
S+11 2D	S-bul	36.4	3.0
V+12 2D	S-bul + m-c	46.3	3.7
R+13 1D equation	core-Sérsic	113.2	5.3

Note. **S+11** did not mask the core and thus underestimated the effective radius and Sérsic index.

Table 65

Best-fit Parameters for the Spheroidal Component of NGC 6251

Work	Model	$R_{\text{e,sph}}$ (arcsec)	n_{sph}
1D maj.	S-bul + m-c	41.7	6.8
1D equation	S-bul + m-c	30.1	5.6
2D	S-bul + m-c	39.3	7.1
GD07 1D maj.	S-bul	173.9	11.8
S+11 2D	S-bul + G-n	42.4	7.0
L+14 2D	S-bul	20.6	5.0

Note. It is not clear why GD07 obtained the largest estimates of the effective radius and Sérsic index (possibly the AGN was bright in their R-band image and added to the central cusp).

Table 66

Best-fit Parameters for the Spheroidal Component of NGC 7052

Work	Model	$R_{\text{e,sph}}$ (arcsec)	n_{sph}
1D maj.	S-bul + m-c	59.4	4.2
1D equation	S-bul + m-c	37.0	5.6
2D	S-bul + m-c	36.2	4.0
GD07 1D maj.	S-bul	70.4	4.6
S+11 2D	S-bul	39.3	5.0
V+12 2D	S-bul + e-d	4.3	1.8
L+14 2D	S-bul	26.6	4.2

Note. The model of **V+12** 2D includes an artificial large-scale disk and thus results in the lowest estimates of the effective radius and Sérsic index.

Table 67

Best-fit Parameters for the Spheroidal Component of NGC 7619

Work	Model	$R_{\text{e,sph}}$ (arcsec)	n_{sph}
1D maj.	S-bul + e-id	63.2	5.3
1D equation	S-bul + e-id	58.0	5.2
R+13 1D equation	core-Sérsic	100.1	9.3

extreme outliers in the black hole mass–spheroid stellar mass diagram.

Bars are usually recognizable from galaxy images and unsharp masks, although local maxima/minima or abrupt changes in the radial profiles of the isophotal parameters can provide additional evidence for less obvious bars. As noted, we were able to successfully fit bars with a Ferrer function (NGC

Table 68
Best-fit Parameters for the Spheroidal Component of NGC 7768

Work	Model	$R_{\text{e,sph}}$ (arcsec)	n_{sph}
1D maj.	S-bul + m-c	92.9	8.4
1D equation	S-bul + m-c	42.1	6.7
R+13 1D equation	core-Sérsic	46.1	6.2

Table 69
Best-fit Parameters for the Spheroidal Component of UGC 03789

Work	Model	$R_{\text{e,sph}}$ (arcsec)	n_{sph}
1D maj.	S-bul + e-d + F-bar + G-r	1.8	1.9
1D equation	S-bul + e-d + F-bar + G-r	2.4	1.4

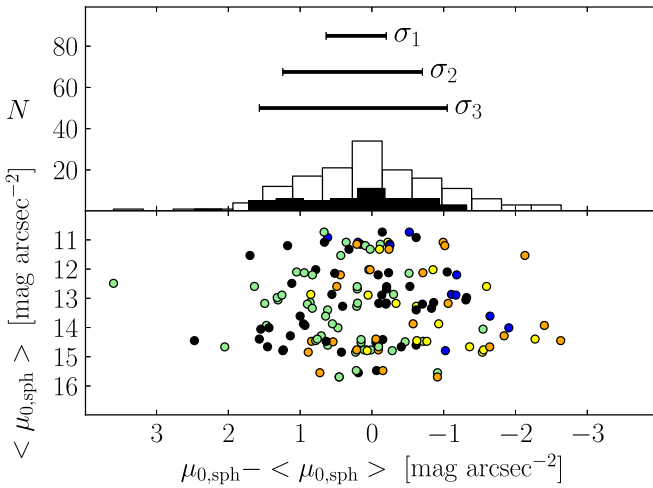


Figure 13. Bottom panel: 49 galaxies for which at least one measurement of the spheroid central surface brightness $\mu_{0,\text{sph}}$ —either in the K band or at $3.6 \mu\text{m}$ —is available from the literature (Table 3), in addition to that measured by us. The K -band magnitudes were converted into $3.6 \mu\text{m}$ magnitudes (see Section 4.2 for details). The average value $\langle \mu_{0,\text{sph}} \rangle$ is plotted against the difference between the individual measurements of a galaxy and the average value for that same galaxy. See Figure 9 for color description and explanation of the top panel.

4151 is the only case for which we described the bar with an $n \sim 0.2$ Sérsic model). Disk-like components embedded in the bulges of spiral galaxies were described with an $n \lesssim 1$ Sérsic model or, in a few cases, with a Ferrer function.¹⁵ This approach is similar to that of Laurikainen et al. (2010), who fit bars with a Ferrer function and inner disks with a Sérsic model. Given that our galaxy sample lacks “late-type spiral” galaxies, it is not surprising (Gadotti & de Souza 2006) that we did not find bars with exponential profiles (e.g., Elmegreen & Elmegreen 1985; Gadotti 2008; Kim et al. 2015). The bars in our sample were found to have rather flat inner profiles, as is commonly found for bars in “early-type spiral” galaxies (Gadotti & de Souza 2006).

The presence of a nuclear component—either resolved or unresolved—was generally expected in (but not restricted to) galaxies that host an optical AGN and circumnuclear dust.

¹⁵ One advantage of choosing a Ferrer function over a Sérsic profile to fit a disk-like component embedded in the bulge is to reduce degeneracies with the Sérsic profile that describes the bulge.

Nuclear stellar disks and nuclear star clusters fall into the category of nuclear components too, but their identification can be more subtle than for AGNs. Nuclear clusters have typical sizes of a few parsecs; therefore, for the majority of our galaxies they are unresolved in *Spitzer*/IRAC $3.6 \mu\text{m}$ observations. If an identification from high-resolution observations was available from the literature, we relied on that; otherwise, we concluded that a galaxy was nucleated from an excess of nuclear light in the residuals of the fit.¹⁶ Unresolved nuclear components were fit with our optimal Moffat PSF, whereas resolved nuclear components were modeled with (PSF-convolved) narrow Gaussian functions (for a discussion of the importance of fitting nuclear components, see Wadadekar et al. 1999; Ravindranath et al. 2001; Peng et al. 2002; Gadotti 2008). Rings were identified from galaxy images and unsharp masks and modeled with symmetric Gaussian ring profiles (e.g., Sheth et al. 2010; Kim et al. 2014).

As an illustration, we consider the galaxy NGC 2974, a spiral galaxy that has been misclassified as an elliptical galaxy in the RC3 catalog (de Vaucouleurs et al. 1991). This galaxy hosts a Seyfert AGN (Véron-Cetty & Véron 2006) and filamentary dust in its center (Tran et al. 2001). NGC 2974 is classified as a fast rotator by the ATLAS^{3D} survey, and indeed the velocity map obtained by the SLUGGS survey shows that the galaxy kinematics is rotation dominated well beyond three effective radii ($R > 150''$), as expected from a large-scale disk. From an inspection of the unsharp mask, we identified a ring at $R \sim 50''$, which might be a residual of two tightly wound spiral arms, and an elongated bar-like component within $R \lesssim 30''$, which is in addition to the more spherical bulge and produces a peak in the ellipticity and position angle profiles at $R \sim 20''$. Our 1D galaxy decomposition for NGC 2974 (Figure 4) consists of a Sérsic bulge, an exponential large-scale disk, a Ferrer bar, a Gaussian nuclear component (AGN), and a Gaussian ring. Although the ring is extremely faint, it is important to account for it in the galaxy decomposition. A model without the ring component results in a “steeper” exponential profile for the disk (i.e., the exponential model has a smaller scale length and a brighter central surface brightness) and produces bad residual structures within $R \lesssim 40''$. Our best-fit model returns a $3.6 \mu\text{m}$ bulge major-axis effective radius $R_{\text{e,sph}}^{\text{maj}} = 8.3$ arcsec, equivalent-axis Sérsic index $n_{\text{sph}}^{\text{eq}} = 1.2$, and apparent magnitude $m_{\text{sph}} = 8.65$ mag. Sani et al. (2011) modeled NGC 2974 with a Sérsic bulge and a Gaussian nuclear component (AGN), but did not account for the large-scale disk. From their best-fit 2D model, they obtained a three times larger $3.6 \mu\text{m}$ bulge major-axis effective radius ($R_{\text{e,sph}}^{\text{maj}} = 27.2$ arcsec), a 2.5 times larger Sérsic index ($n_{\text{sph}} = 3$), and a significantly brighter apparent magnitude ($m_{\text{sph}} = 7.28$ mag).

3.6. 2D Fits

2D decompositions were carried out using the software IMFIT (Erwin 2015). For each galaxy, we built a 2D model that was consistent with the corresponding 1D model in terms of

¹⁶ This conclusion was drawn after going through the following steps. First we identified all the subcomponents of a galaxy (assuming that the galaxy was not nucleated), built a model accordingly, and fit it to the data. If the residuals of the fit showed a nuclear light excess, we repeated the fit by excluding the data points within the nuclear region. Only after checking that the outcome of the last fit was consistent with a fit that included a small nuclear component did we infer the presence of a stellar nuclear component.

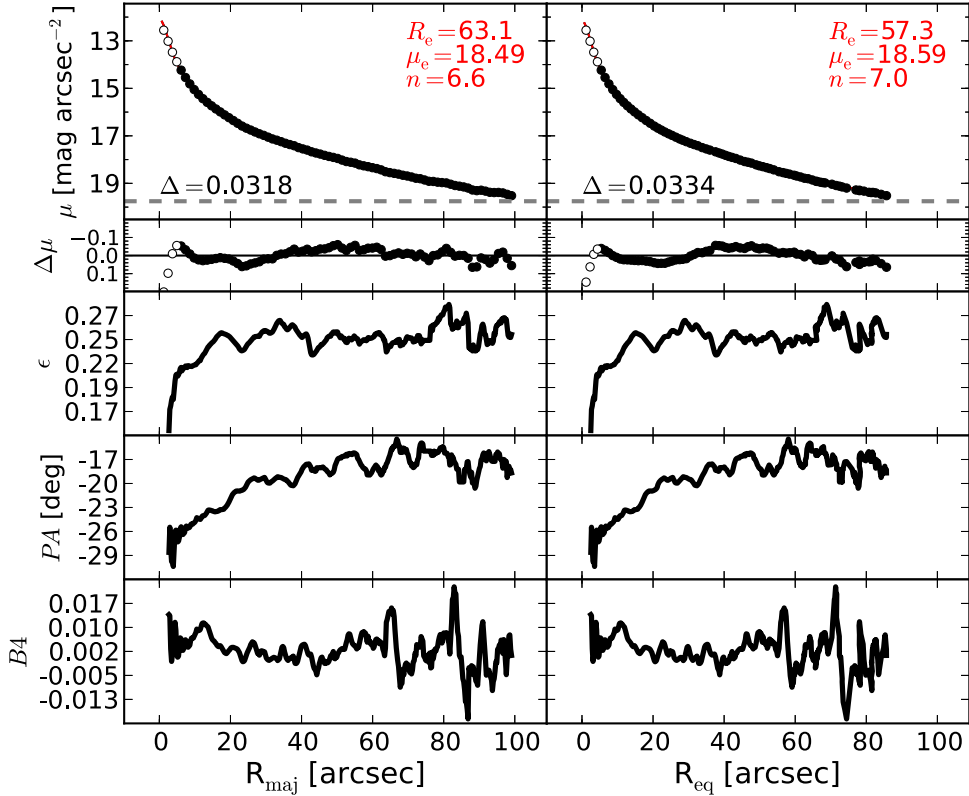


Figure 14. IC 1459: an elliptical galaxy with a fast counterrotating stellar component (Franx & Illingworth 1988; Cappellari et al. 2002), nuclear dust, and indications of a nuclear stellar disk (Forbes et al. 1994). The kinematically decoupled component cannot be identified as a separate structure in photometric observations. This galaxy also has an unresolved partially depleted core (Rusli et al. 2013a). Our isophotal analysis confirms a simple morphology for IC 1459, with no evident embedded components. After masking the innermost $6''$, we fit this galaxy with a Sérsic profile.

number and type of components. The only difference between our 1D and 2D models pertains to the description of bars: because the Ferrer profile is not made available in IMFIT, bars were fit with a 2D Gaussian function.

The 2D decomposition of NGC 2974 is presented in Figure 5. The galaxy was modeled with a Sérsic bulge, an exponential disk, and a Gaussian bar. The nuclear component was masked, and the ring was not modeled.¹⁷ Our best-fit 2D model returns a bulge major-axis effective radius $R_{\text{e,sph}}^{\text{maj}} = 10.5$ arcsec, a bulge Sérsic index $n_{\text{sph}} = 1.3$, and a $3.6 \mu\text{m}$ bulge apparent magnitude $m_{\text{sph}} = 8.39$ mag, in fairly good agreement with our 1D decomposition. Fits and descriptions for the other galaxies are available online.

4. RESULTS

For each galaxy, after we identified its various components and built a model accordingly, we simultaneously performed a set of four 1D fits. All four fits use a Moffat-convolved model. Two fits use the major-axis surface brightness profile, and the remaining two use the equivalent-axis surface brightness profile. For each of these pairs, we use a logarithmically sampled surface brightness profile and a linearly sampled surface brightness profile. Because our fitting routine intentionally does not employ an error-weighting scheme on the data

points that constitute the surface brightness profile, a fit to a logarithmically sampled profile puts more weight on the inner region of the galaxy and poorly constrains the outskirts. On the other hand, a fit to a linearly sampled surface brightness profile equally treats inner and outer regions, but is more susceptible to sky-background subtraction issues.

We found that the fits are, in general, more sensitive to the choice of the initial parameters when using logarithmically sampled profiles than linearly sampled profiles. In addition, a visual examination of the residuals revealed that the quality of the fit within one galaxy effective radius is superior when tighter constraints are put on the galaxy outskirts. In other words, the better quality of the residuals led us to prefer the fits that use linearly sampled surface brightness profiles, although the results were usually very similar, as might be expected.

Among the initial sample of 75 galaxies, we did not attempt to model three galaxies: M32, NGC 4486A, and the Circinus galaxy. The first two have been stripped by their massive companions and thus have uncertain morphology. The Circinus galaxy lies at only 4° from the Galactic plane; therefore, its image mosaic is contaminated by a large number of foreground stars. Of the remaining 72 galaxies, we obtained satisfactory 1D decompositions for 66, whereas the models of 6 galaxies were judged not reliable and were thus excluded. We also performed reliable 2D decompositions for 31 galaxies.

A galaxy-by-galaxy comparison between our best-fit models and those from the previous literature helped identify the optimal decompositions and past problems. We compared our best-fit models with those of Graham & Driver (2007a), Sani et al. (2011), Beifiori et al. (2012), Vika et al. (2012), and Läsker et al.

¹⁷ We built the 2D model first including and then omitting a Gaussian ring component, but both models converged to the same solution, i.e., the fit “ignored” the presence of the faint ring. This did not happen in the 1D decomposition because of the different weighting scheme used by the fitting routines.

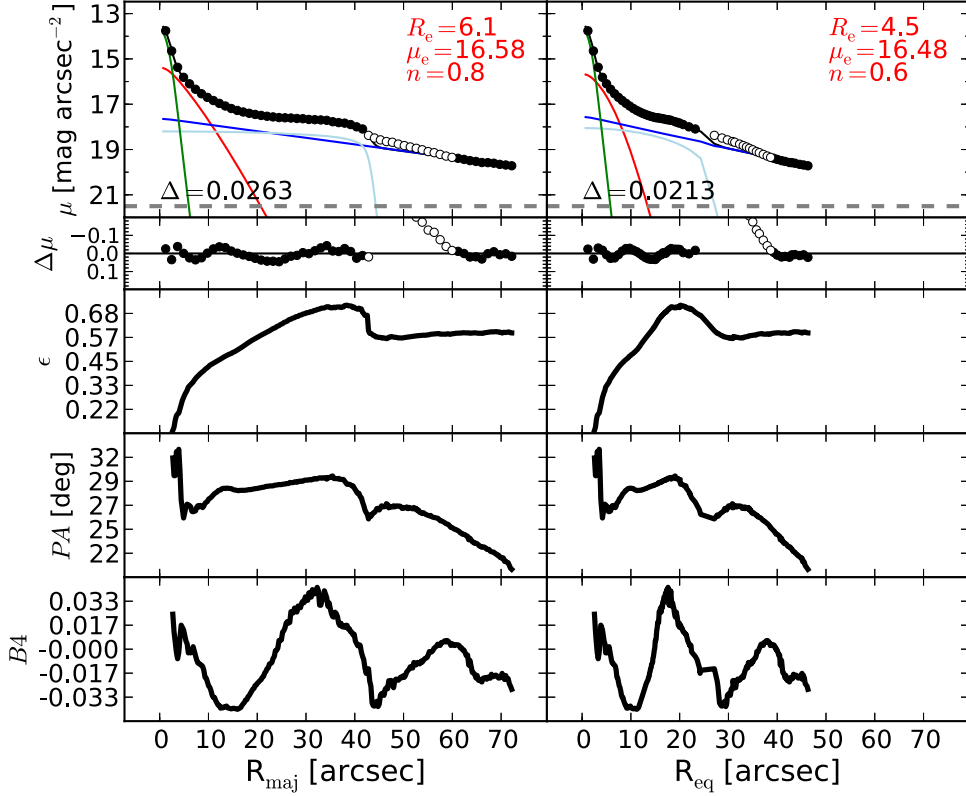


Figure 15. IC 2560: a barred spiral galaxy with a Seyfert AGN (Véron-Cetty & Véron 2006) and dust within the central $2''$.5 (Martini et al. 2003). A visual inspection of the image of IC 2560 reveals a boxy bulge and a large-scale bar that extends out to $R_{\text{maj}} \lesssim 43''$. The disk appears to be slightly lopsided along the direction of the bar, owing to two nonsymmetric ansae, but it becomes symmetric beyond $R_{\text{maj}} \gtrsim 60''$. This is why the surface brightness profile deviates from a perfect exponential in the radial range $42'' \lesssim R_{\text{maj}} \lesssim 60''$, which is excluded from the fit. Motivated by the presence of a strong optical AGN and dust in the nucleus (which adds rather than obscures at $3.6 \mu\text{m}$), we account for an excess of nonstellar light by adding a central Gaussian component to the model.

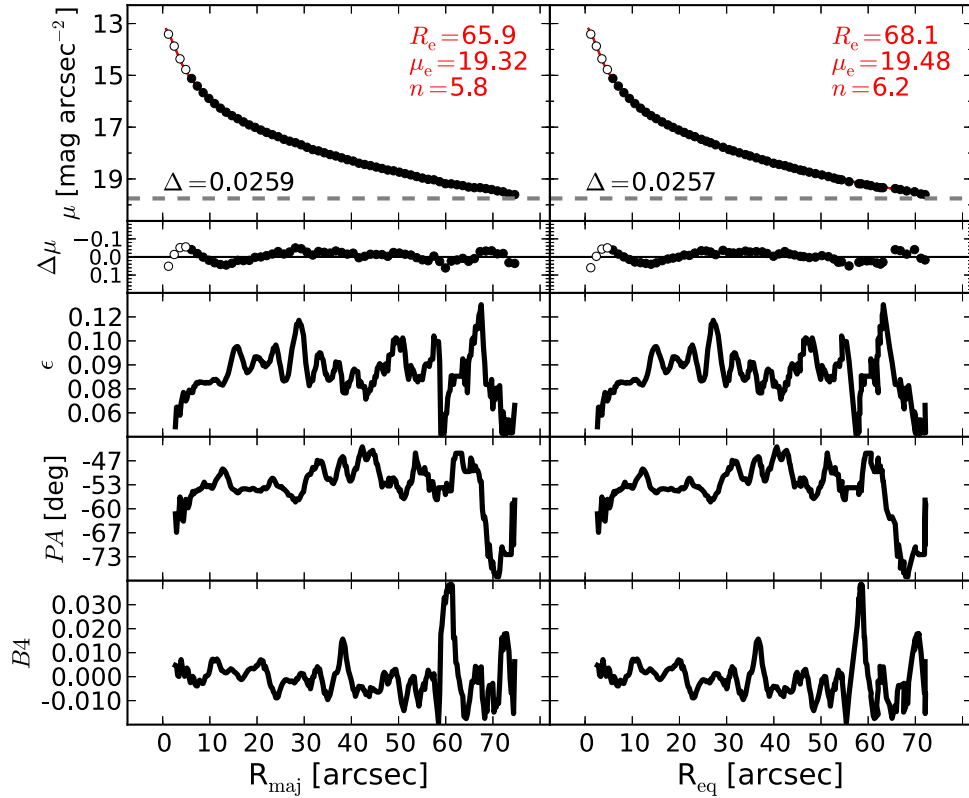


Figure 16. IC 4296: an elliptical galaxy. Owing to its high stellar velocity dispersion, this galaxy is expected to host a partially depleted core. After masking the innermost $6''$.1, we find that a single Sérsic profile provides a good description of this galaxy.

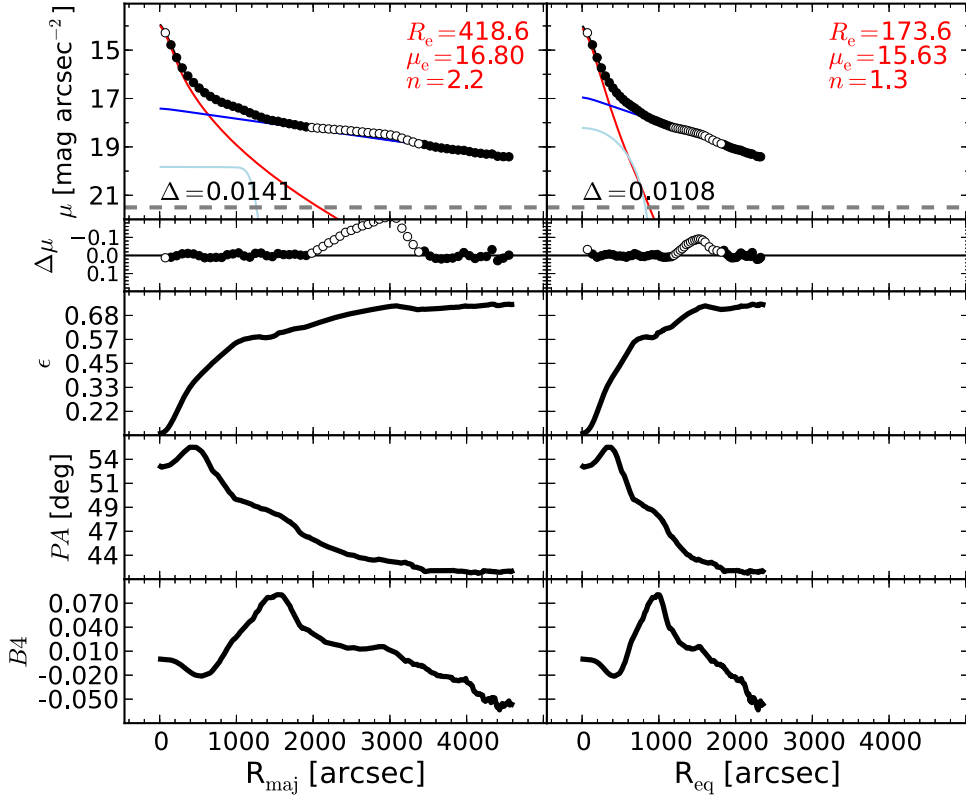


Figure 17. M31 (Andromeda galaxy): a spiral galaxy. Although for decades this galaxy had been classified as an unbarred spiral, recent works have revealed the presence of a bar (Athanassoula & Beaton 2006; Beaton et al. 2007; Morrison et al. 2011), seen as the plateau at $800'' \lesssim R_{\text{maj}} \lesssim 1000''$. M31 also features a broad ring-like structure at $R_{\text{maj}} \sim 50'$ (Athanassoula & Beaton 2006). We applied the *smoothing* technique described in Section 3.4 to the analysis of M31. The region $2000'' \lesssim R_{\text{maj}} \lesssim 3400''$, where the *pseudoring* is observed, is excluded from the fit. A Sérsic + exponential fit is not adequate to describe the light profile of M31, as the residuals of such a fit display a structure in correspondence of the bar ($R_{\text{maj}} \lesssim 1500''$). The addition of a Ferrer function to account for the bar notably improves the fit.

(2014a). We also considered the best-fit models of Laurikainen et al. (2010) and Rusli et al. (2013a) because, although they did not specifically deal with black hole—galaxy scaling relations, their galaxy samples significantly overlap with ours.

Table 2 lists the results from both the 1D and 2D fits.

4.1. 1D versus 2D Decompositions

Here we explore how 1D and 2D decompositions compare with each other. Readers not interested in our practical knowledge, having dealt with 1D and 2D techniques of galaxy modeling at the same time, can skip to Section 4.2. We summarize our experience in the following points:

1. A visual inspection of galaxy images and their unsharp masks is often not sufficient to accurately identify all of a galaxy’s components. Weak bars and some embedded disks can easily be missed. Other (inclined) embedded disks can be confused with large-scale disks. In this regard, the 1D isophotal analysis is extremely helpful. Local minima/maxima or abrupt changes in the ellipticity, position angle, and fourth harmonic profiles contain precious information about a galaxy’s constituents.
2. The ellipticity and position angle of triaxial spheroids can vary with radius. The analytic functions used by 2D decomposition codes to fit galaxy components have fixed ellipticity and position angle; thus, they cannot account for these radial gradients. This problem is overcome with 1D decomposition techniques because the ellipticity and

additionally the deviations from elliptical isophotes are efficiently included in the equivalent-axis fit (see the Appendix of Ciambur 2015).

3. The interpretation of the residual surface brightness profile is often crucial to identify the optimal decomposition for a galaxy. In our experience, we found that interpreting 1D residuals was easier and more productive than 2D residuals.

Although we attempted 2D modeling for the 72 galaxies in our sample, more than half of the 2D decompositions were not successful or did not converge to a meaningful solution. This should serve as a tip to users of 2D fitting codes. When physically meaningful spheroid parameters are required, the output may not be reliable and should be inspected. For the 31 galaxies that had successful 2D decompositions, we compare with their 1D parameters in Figures 6–8. The agreement between 1D and 2D effective radii and magnitudes is remarkable, whereas a larger amount of scatter in the Sérsic indices can be caused by the fact that 2D measurements do not exactly correspond to 1D equivalent-axis measurements. No systematic effects are observed in any of these three plots, which indicates that 1D and 2D techniques of galaxy modeling—when performed on the same galaxy—can give consistent results.

In conclusion, since we found that the best-fit parameters do not depend on the decomposition method (1D or 2D) used, and given that we obtained more successful 1D decompositions than 2D, we will base our analysis on the results from the 1D fits.

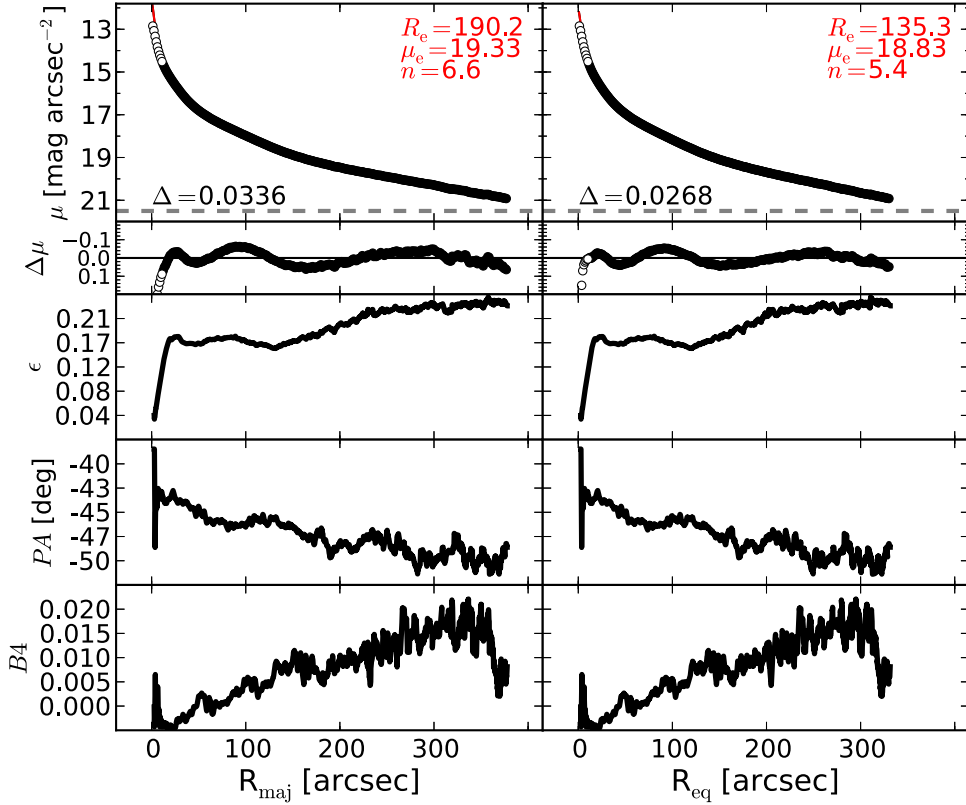


Figure 18. M49: the brightest member of the Virgo Cluster, a giant elliptical galaxy with a slightly resolved partially depleted core (Rusli et al. 2013a). The data within the innermost 12'' are excluded from the fit. We fit M49 with a single Sérsic profile.

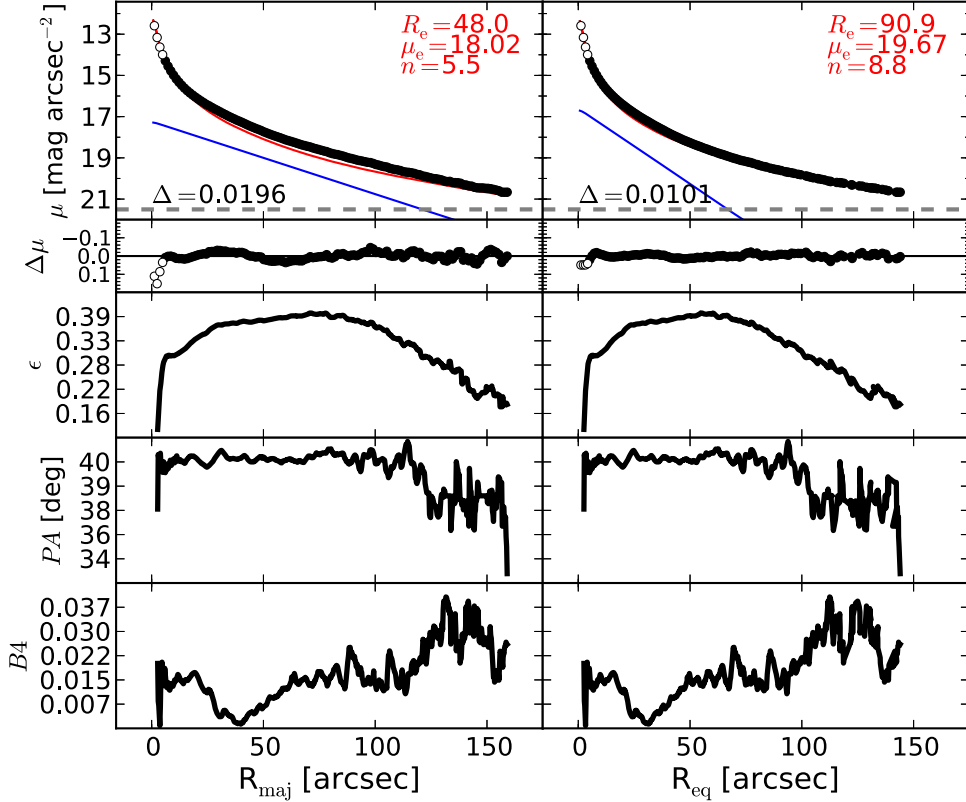


Figure 19. M59: an elliptical galaxy with an edge-on, intermediate-scale embedded disk (Scorza & Bender 1995) and a thin, faint nuclear stellar disk (Ferrarese et al. 2006; Ledo et al. 2010). The intermediate-scale embedded disk is clearly visible in our unsharp mask image (not shown), and the velocity map (ATLAS^{3D}) confirms the presence of this rapidly rotating component, which is modeled with an exponential function. We choose not to account for the nuclear stellar disk by excluding the innermost 6.''1 from the fit.

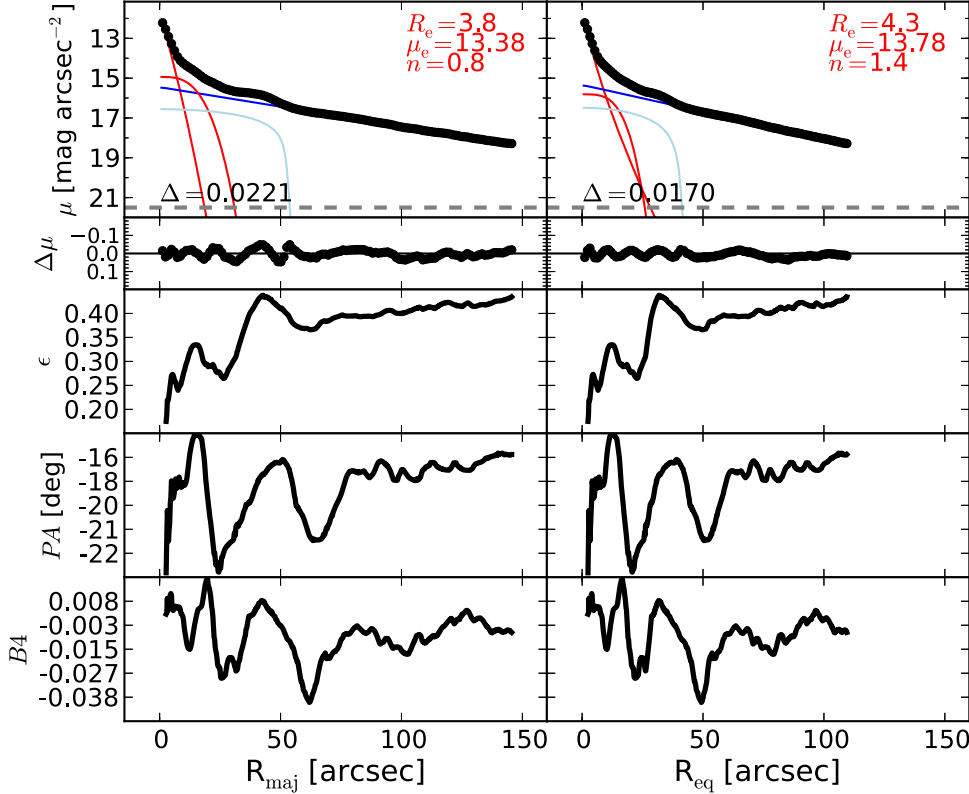


Figure 20. M64: a dusty spiral galaxy with a Seyfert AGN (Véron-Cetty & Véron 2006). A large-scale bar ($R_{\text{maj}} \lesssim 50''$) can be identified in the unsharp mask and produces corresponding peaks in the ellipticity, PA, and $B4$ profiles. This is modeled with a Ferrer function. Additional peaks in the ellipticity, PA, and $B4$ profiles at $R_{\text{maj}} \sim 15''$ signal the presence of an embedded disky component, which we describe with a low- n Sérsic function. Although the galaxy is dusty and hosts an AGN, we do not observe any nuclear excess of light in the fit residuals, and therefore we found it unnecessary to add a nuclear component to our model.

4.2. Parameter Uncertainty

Estimating the uncertainties associated with the best-fit parameters of our 1D galaxy decompositions is not straightforward. Monte Carlo simulations could be used for this purpose, but they would take into account only random errors and not unknown systematic errors. Systematic errors include incorrect sky subtraction, inaccurate masking of contaminating sources, imprecise description of the PSF, erroneous choice of model components (for example, when failing to identify a galaxy **subcomponent** and thus omitting it in the model, or when describing a galaxy **subcomponent** with an inadequate function), the radial extent of the surface brightness **profile**, and its sampling. These factors are not included in popular 2D fitting **codes**, which report only the random errors associated with their fitted parameters. Moreover, when performing **multi-component** decomposition of **high-S/N** images of **nearby**—and **therefore well-resolved**—galaxies, errors are dominated by systematics rather than Poisson noise. For this reason, we decided to estimate the uncertainties of the spheroid best-fit parameters with a method that took into account systematic errors.

4.2.1. Goodness of the Spheroid Modeling

For each of our fits, we calculated the associated **rms** scatter using

$$\Delta = \sqrt{\frac{\sum_{i=0}^N (\mu_i^{\text{obs}} - \mu_i^{\text{mod}})^2}{N_{\text{dof}}}}, \quad (2)$$

where N_{dof} is the number of **degrees of freedom**, μ_i^{obs} is the observed surface **brightness**, and μ_i^{mod} is the model surface brightness at each data point i . Although useful to evaluate the overall quality of a galaxy decomposition, the **rms** scatter alone cannot be used to assess the goodness of the fit for the spheroidal component only, unless the galaxy is a pure spheroid and has consequently been modeled with a single Sérsic profile. To illustrate this point with an example, one can imagine a situation in which a galaxy is thought to be made of a small bulge and a much more extended disk. This galaxy is decomposed with a Sérsic + exponential model. The exponential function provides an excellent description of the light profile of the disk, whereas the Sérsic function does not do the same for the bulge. The residuals of the fit will then be flat and close to zero at large radii, where the emission of the disk dominates over that of the bulge, while they will display significant departures at small radii, in correspondence with the poorly fit spheroidal component. In the case of linear sampling, because the part of the surface brightness profile pertaining to the disk may contain more data points than the part pertaining to the bulge, the global **rms** scatter will be relatively small, but it obviously will not reflect the accuracy of the fit to the spheroidal component only.

A simple but powerful way to get a feeling of how precisely the global model and its spheroidal component have fared is to look at the major- and equivalent-axis fits of each galaxy and visually inspect the structures of the residual surface brightness profile (i.e., the second row in Figure 4) within ~ 1 –2 spheroid

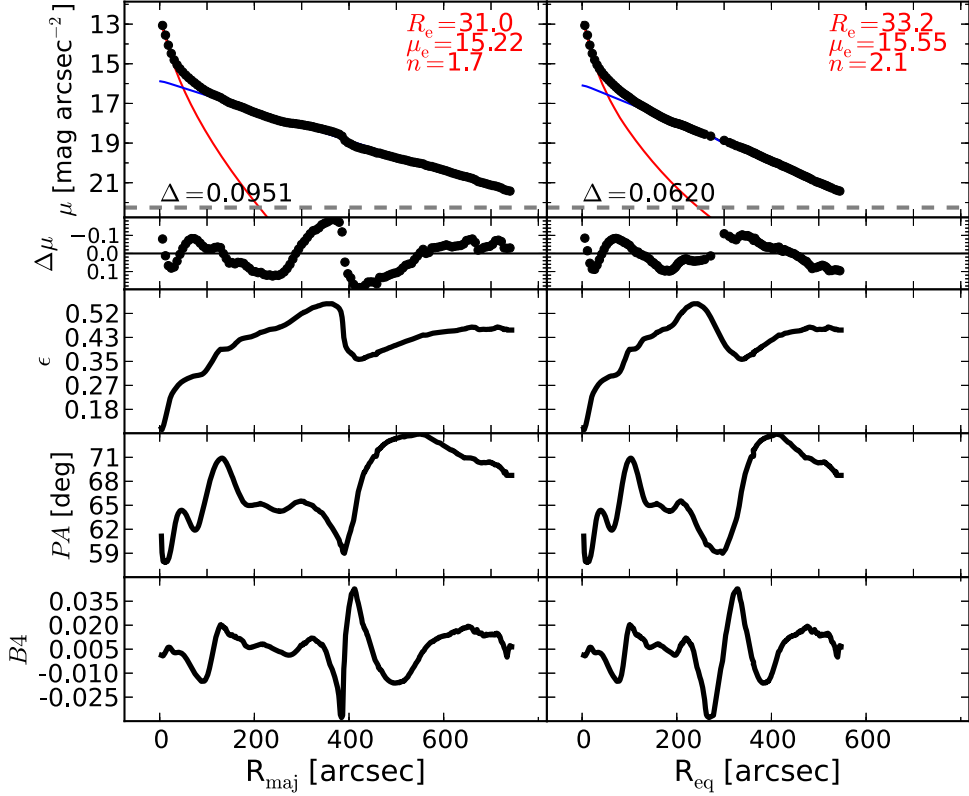


Figure 21. M81: an early-type spiral galaxy. This galaxy features a nuclear bar at $R_{\text{maj}} \lesssim 17''$ and a large-scale bar at $R_{\text{maj}} \lesssim 130''$ (Elmegreen et al. 1995; Gutiérrez et al. 2011; Erwin & Debattista 2013). We applied the smoothing technique described in Section 3.4 to the analysis of M81. The bars are not particularly evident in the galaxy image or in the unsharp mask. The bump at $R_{\text{maj}} \lesssim 400''$ is due to spiral arms. Attempts to account for the bars in the fit were unsuccessful. For this reason, we use a simple Sérsic + exponential model.

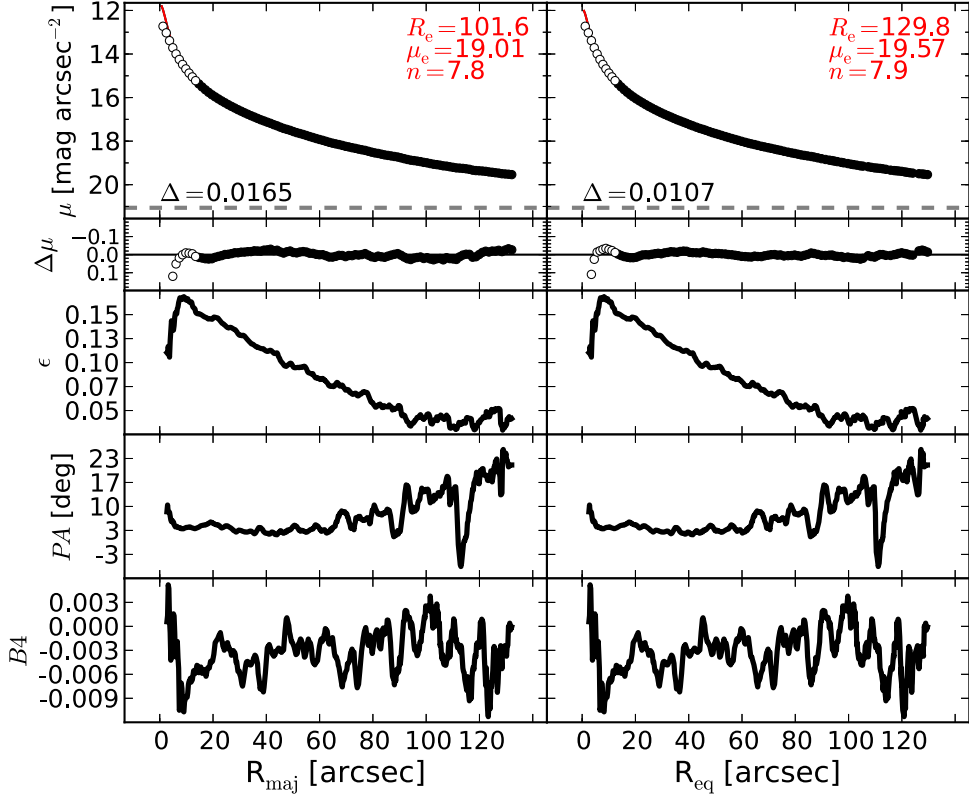


Figure 22. M84: an elliptical galaxy with a slightly resolved partially depleted core (Rusli et al. 2013a). The unsharp mask reveals a faint inner component ($R_{\text{maj}} \lesssim 12''$). We exclude the data within $R_{\text{maj}} < 13.8''$ and model the galaxy with a Sérsic profile.

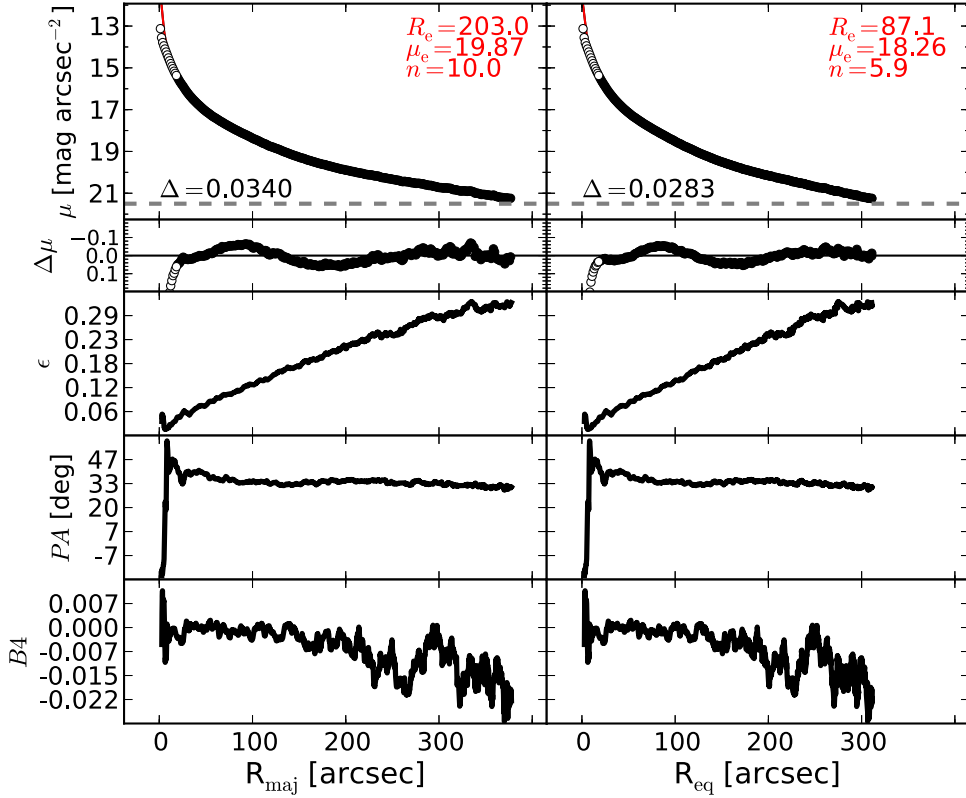


Figure 23. M87: a giant elliptical galaxy belonging to the Virgo Cluster. This galaxy has a large ($>7''$), partially depleted core (Ferrarese et al. 2006). The morphology of M87 is similar to that of M49. The innermost $18.5''$ are excluded, and a Sérsic model is used to fit M87. We note that the effective radius obtained from our 1D major-axis fit is more than a factor of two larger than that obtained from our 2D fit. This is due to the fact that the 2D model has fixed ellipticity and cannot account for the strong ellipticity gradient of the galaxy, which serves as a warning to some 2D fits in the literature.

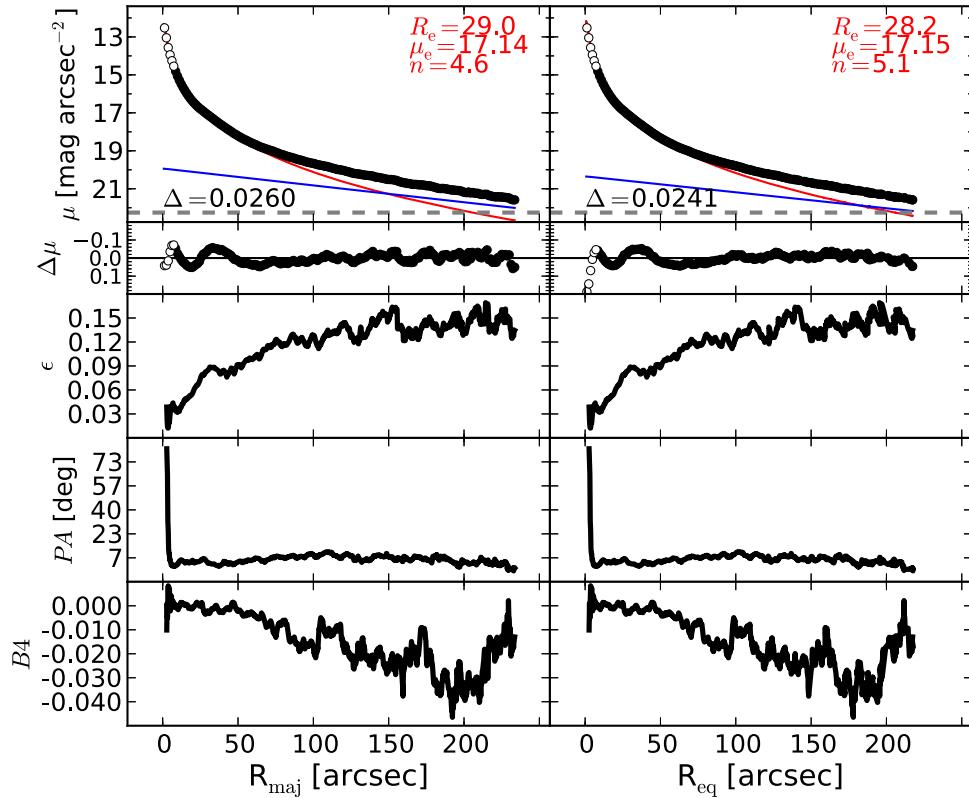


Figure 24. M89: an elliptical galaxy with an unresolved partially depleted core (Rusli et al. 2013a). The galaxy halo dominates the light at large radii, where the isophotes are significantly more elliptical than in the inner part of the galaxy. The halo is modeled with an exponential function.

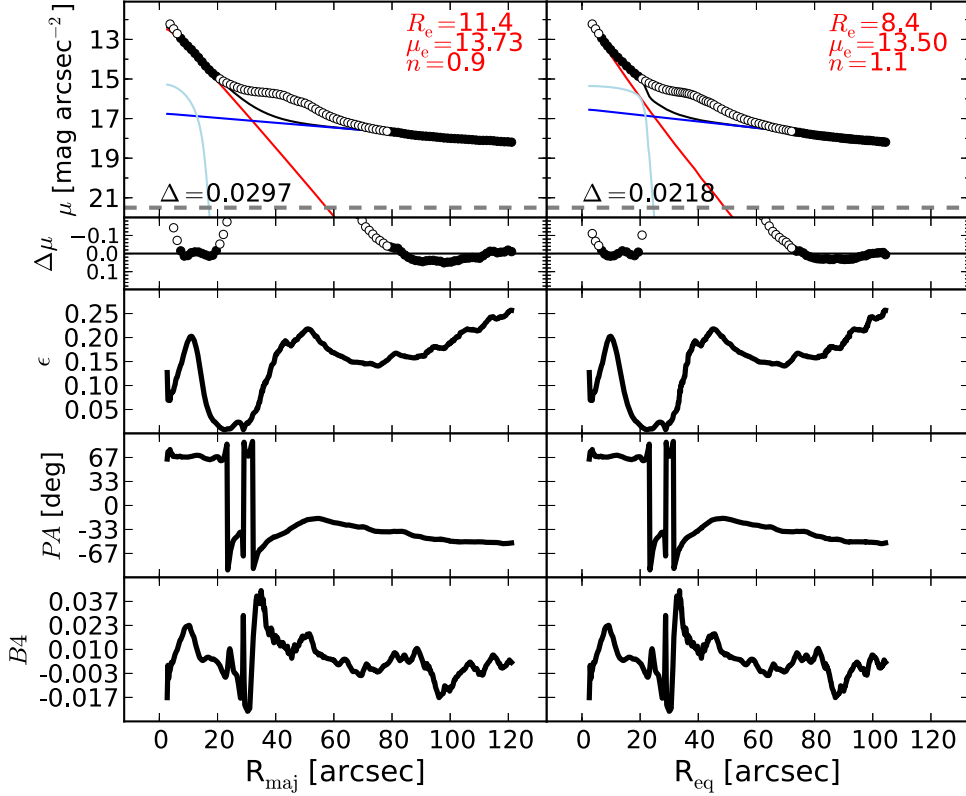


Figure 25. M94: a face-on spiral galaxy, with a Seyfert AGN (Véron-Cetty & Véron 2006) and circumnuclear dust (Elmegreen et al. 2002; Peebles & Martini 2006). This galaxy has a ring-like structure at $R_{\text{maj}} \sim 50''$ (Muñoz-Tunón et al. 1989). The ellipticity and $B4$ profiles display a local maximum at $R_{\text{maj}} \sim 10''$, indicating the presence of a disky component embedded in the bulge, as already noted by Fisher & Drory (2010). We model this component with a Ferrer function. We exclude the data within the innermost $6''/7'$, owing to the AGN contribution. Attempts to model the ring were unsuccessful, resulting in a degenerate model; therefore, we exclude the data in the range $20'' \lesssim R_{\text{maj}} \lesssim 80''$.

effective radii. We did this using a grade from 1 to 3, assigned according to the following criteria:

1. A grade of 1 was given to the best fits, i.e., fits that do not exhibit any of the problems listed below.
2. A grade of 2 was issued in the following cases: the residuals in correspondence with the radial extent of the spheroidal component are not randomly distributed around zero, being symptomatic of a Sérsic model having a curvature (regulated by the Sérsic index n) that does not quite match the real “shape” of the spheroid; when we identified but were not able to model a galaxy subcomponent with the same accuracy dedicated to the other components; in the case of apparent inconsistencies between the model and the observed galaxy properties (e.g., an embedded disk modeled with an exponential function, whose scale length does not quite match the size of the disk as expected from the ellipticity profile or the velocity map); and when the Sérsic model used to describe the spheroidal component has a size—as measured by the effective radius—comparable to a few times the FWHM of the PSF. Galaxies in this category are reasonably well fit despite these issues.
3. A grade of 3 was assigned to the poorer and more anomalous fits, or those affected by an obvious degeneracy between the spheroid Sérsic profile and the remaining model components (e.g., when the spheroid Sérsic index varies by as much as 50% among the four different realizations of the fit, or when the output of

the fit strongly depends on the choice of the initial parameters).

As a result, we classified 27 galaxies (38% of the 72 galaxies for which we attempted a 1D decomposition) with grade 1, 29 galaxies (40%) with grade 2, and 10 galaxies (14%) with grade 3. Six galaxies could not be modeled. We report the assigned grades in Table 2 (column 10).

4.2.2. Uncertainties on n_{sph}

In Figure 9, for 58 galaxies, we compare the measurements of the spheroid Sérsic index obtained by different authors with those obtained by us. For each galaxy, we computed the average value $\langle \log(n_{\text{sph}}) \rangle$ of the available measurements, and we plot it against the scatter of the individual measurements around each spheroid’s $\langle \log(n_{\text{sph}}) \rangle$. The measurements are heterogeneous, in the sense that they were obtained from 1D or 2D decompositions of data in different wavelengths, and they refer either to the major axis, the equivalent axis, or some 2D average. In Figure 9, the black histogram shows the distribution of the scatter around $\langle \log(n_{\text{sph}}) \rangle$ for our measurements; 38% of this distribution lies within $-\sigma_1^- = -0.08$ dex and $+\sigma_1^+ = +0.06$ dex, 78% lies within $-\sigma_2^- = -0.21$ dex and $+\sigma_2^+ = +0.17$ dex, and 92% lies within $-\sigma_3^- = -0.25$ dex and $+\sigma_3^+ = +0.25$ dex. We elect to use $\pm\sigma_1^\pm$, $\pm\sigma_2^\pm$, and $\pm\sigma_3^\pm$ as 1σ uncertainties for our measurements of $\log(n_{\text{sph}})$ obtained from “grade 1,” “grade 2,” and “grade 3” fits, respectively. This means that if the fit to a galaxy was classified as “grade 1,” the (logarithmic) value of the spheroid Sérsic

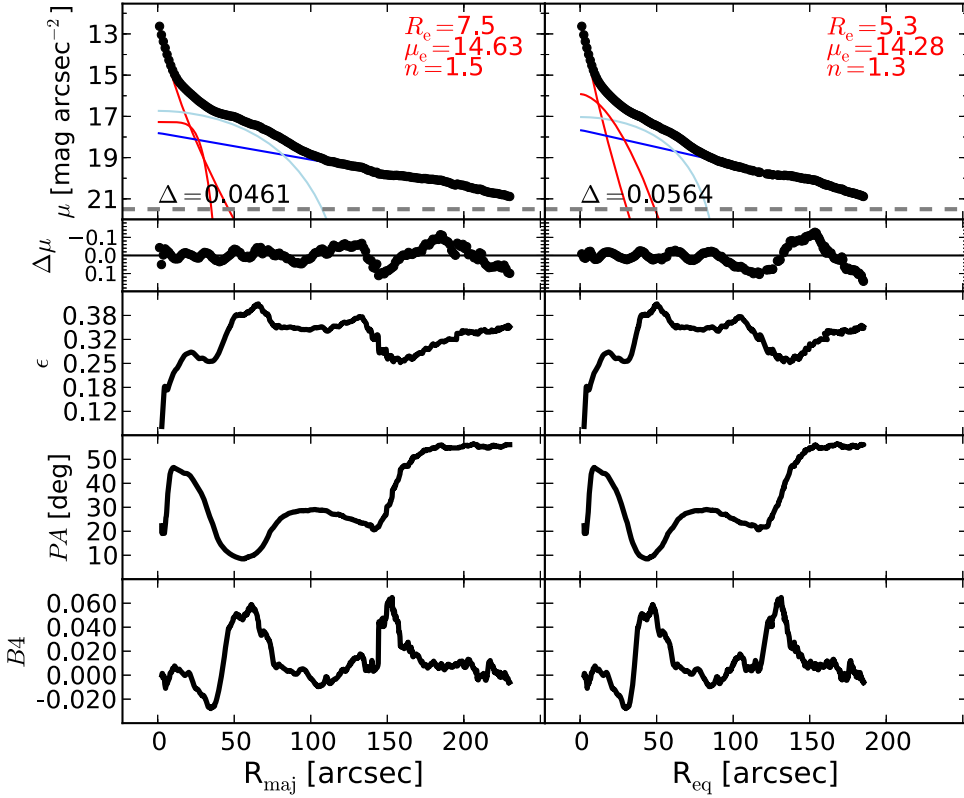


Figure 26. M96: a spiral galaxy with a large-scale bar and no AGN activity (Martini et al. 2003; Nowak et al. 2010). Erwin (2004) observed the presence of two bars in this galaxy. Nowak et al. (2010) reported the presence of a large pseudobulge ($R_{\text{e,sph}} = 1.6''$, $n_{\text{sph}} = 2.3$). However, they came to this conclusion by modeling only the innermost $8''/5$ of the light profile of M96 with a Sérsic-classical bulge and an exponential pseudobulge, but without subtracting the contribution of the large-scale disk and the large-scale bar. They also acknowledged the presence of a secondary inner bar, but did not include it in their fit. M96 has a complex morphology. The large-scale disk does not exhibit a perfect exponential profile, mainly because of wound spiral arms resembling a ring ($R_{\text{maj}} \sim 185''$), which however, are too faint and irregular to be described with a Gaussian ring model. The large-scale bar extends out to $R_{\text{maj}} \lesssim 80''$ and is modeled with a Ferrer function. A peak at $R_{\text{maj}} \sim 25''$ in the ellipticity profile reveals an inner disk component embedded in the bulge, which we model with a low- n Sérsic profile.

index \tilde{n}_{sph} and associated uncertainties would be $\log(\tilde{n}_{\text{sph}})^{+\sigma_1^+}_{-\sigma_1^-} = \log(\tilde{n}_{\text{sph}})^{+0.06}_{-0.08}$; if the fit to that galaxy was classified as “grade 2,” then one would have $\log(\tilde{n}_{\text{sph}})^{+\sigma_2^+}_{-\sigma_2^-} = \log(\tilde{n}_{\text{sph}})^{+0.17}_{-0.21}$; and so on.

4.2.3. Uncertainties on $R_{\text{e,sph}}$

The uncertainties on the spheroid effective radii were computed using the same methodology as employed for the Sérsic indices. However, in Figure 10 we include only major-axis measurements of $R_{\text{e,sph}}$. The associated 1σ uncertainties for our measurements of $\log(R_{\text{e,sph}})$ are $-\sigma_1^- = -0.11$ dex and $+\sigma_1^+ = +0.07$ dex, $-\sigma_2^- = -0.30$ dex and $+\sigma_2^+ = +0.32$ dex, and $-\sigma_3^- = -0.39$ dex and $+\sigma_3^+ = +0.42$ dex.

4.2.4. Uncertainties on m_{sph}

To estimate the uncertainties on the spheroid magnitudes, we compared (see Figure 11) only those literature measurements coming from K -band or $3.6 \mu\text{m}$ observations. To do this, the $3.6 \mu\text{m}$ magnitudes were converted into K -band magnitudes by applying an additive factor of 0.27 mag, which was estimated using the stellar population models of Worthey (1994), assuming a 13 Gyr old single-burst stellar population with solar metallicity. The associated 1σ uncertainties for our measurements of m_{sph} are $-\sigma_1^- = -0.11$ mag and $+\sigma_1^+ =$

+0.18 mag, $-\sigma_2^- = -0.58$ mag and $+\sigma_2^+ = +0.66$ mag, and $-\sigma_3^- = -0.66$ mag and $+\sigma_3^+ = +0.88$ mag.

4.2.5. Uncertainties on $\mu_{\text{e,sph}}$

As for the spheroid magnitudes, we estimated the uncertainties on the spheroid effective surface brightnesses $\mu_{\text{e,sph}}$ by comparing only K -band or $3.6 \mu\text{m}$ measurements (see Figure 12) and accounting for the mean color difference of 0.27 mag. Not explicitly reported in the literature, effective surface brightnesses were calculated by us using

$$\begin{aligned} \mu_{\text{e,sph}} = m_{\text{sph}} + 5 \log & \left(R_{\text{e,sph}}^{\text{maj}} \sqrt{(b/a)_{\text{sph}}} \right) \\ & + 2.5 \log \left[2\pi n_{\text{sph}} e^{b_n} b_n^{-2n_{\text{sph}}} \Gamma(2n_{\text{sph}}) \right], \end{aligned} \quad (3)$$

where b_n and $\Gamma(2n_{\text{sph}})$ are defined in the Appendix and $(b/a)_{\text{sph}}$ is the spheroid axis ratio. While Laurikainen et al. (2010) and Sani et al. (2011) reported their estimates of $(b/a)_{\text{sph}}$, Vika et al. (2012) and Läsker et al. (2014a) did not. For the last two studies, we used the values of $(b/a)_{\text{sph}}$ reported by Sani et al. (2011). The associated 1σ uncertainties for our measurements of $\mu_{\text{e,sph}}$ are $-\sigma_1^- = -0.33$ mag and $+\sigma_1^+ = +0.57$ mag, $-\sigma_2^- = -0.84$ mag and $+\sigma_2^+ = +1.59$ mag, and $-\sigma_3^- = -1.06$ mag and $+\sigma_3^+ = +1.74$ mag.

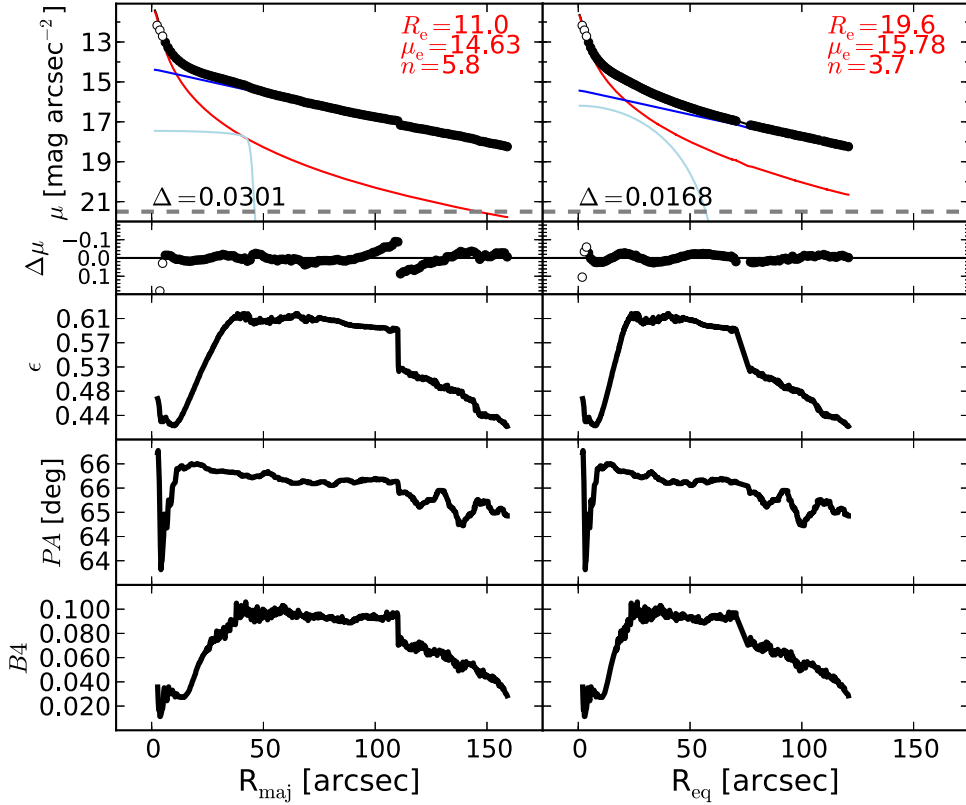


Figure 27. M104: a lenticular/spiral galaxy with a partially depleted core (Jardel et al. 2011). The data within the innermost $6''$ are excluded from the fit, and the most obvious elongated feature of this galaxy is modeled with a Ferrer function. The ellipticity profile indicates that the disk is of intermediate scale (for a thorough analysis of this galaxy, see Gadotti & Sánchez-Janssen 2012).

4.2.6. Uncertainties on $\mu_{0,\text{sph}}$

From the values of $\mu_{e,\text{sph}}$, we derived the central surface brightnesses $\mu_{0,\text{sph}}$ from the equation

$$\mu_{0,\text{sph}} = \mu_{e,\text{sph}} - \frac{2.5b_n}{\ln(10)}. \quad (4)$$

The associated 1σ uncertainties for our measurements of $\mu_{0,\text{sph}}$ are $-\sigma_1^- = -0.20$ mag and $+\sigma_1^+ = +0.64$ mag, $-\sigma_2^- = -0.70$ mag and $+\sigma_2^+ = +1.24$ mag, and $-\sigma_3^- = -1.05$ mag and $+\sigma_3^+ = +1.57$ mag.

5. CONCLUSIONS

The widespread presence of embedded components—in particular intermediate-scale disks—in massive early-type galaxies makes galaxy decomposition an essential tool to properly investigate the scaling relations between black hole masses and host spheroid properties.

Past studies often used different model components for the same galaxy and obtained significantly discrepant results, which led them to draw contrasting conclusions about the black hole–spheroid correlations. These inconsistencies motivated our effort to refine and secure the measure of spheroid properties in a sample of 66 galaxies with a dynamical estimate of the black hole mass. Using $3.6\mu\text{m}$ *Spitzer* satellite images, we performed state-of-the-art galaxy decompositions. The $3.6\mu\text{m}$ band is an excellent tracer of the stellar mass, superior to optical bands and the *K* band. Considerable care has been taken in the data reduction, image mosaicking, sky subtraction, and component model fitting to the galaxy light. We have

compared our best-fit models with those from the literature, to identify and explain discrepancies when present. Our analysis additionally benefited from recourse to kinematical information—not previously used—to aid in the identification of somewhat face-on disks, or the distinction between intermediate-scale disks and large-scale disks, missed in some past investigations and decompositions. Table 3 summarizes the main characteristics of the five past studies that, since 2007, attempted galaxy decompositions in order to derive black hole–spheroid scaling relations, and it highlights, in part, why our endeavor represents a substantial improvement over the past literature.

We reveal that 1D and 2D techniques of galaxy decomposition return the same results when applied to the same galaxy. However, in our practical experience, the failure rate of 2D decompositions is a factor of two higher than the failure rate of 1D decompositions, either because the fit does not converge or because the result is unphysical. A strong limitation of 2D codes is their inability to accommodate the radial gradients of ellipticity and position angle often observed in galaxy spheroids. The interpretation of 1D residual surface brightness profiles is easier than that of 2D residual images. A 1D isophotal analysis was extremely helpful and sometimes even necessary to accurately identify galaxy components. A correct interpretation of the residuals is fundamental to understand and determine the optimal model for a galaxy. Given the level of detail to which each galaxy decomposition was performed, we believe that our analysis cannot be reproduced by current automatic routines. The uncertainties associated with the literature best-fit parameters of the spheroid are dominated by

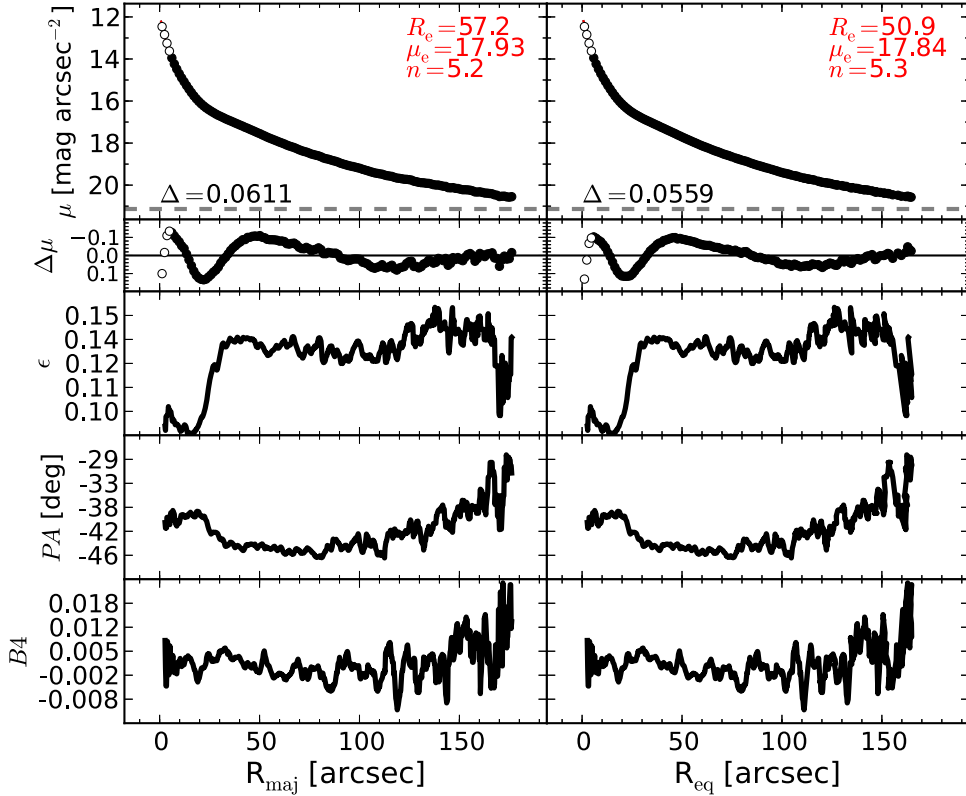


Figure 28. M105: an elliptical galaxy with an unresolved partially depleted core (Rusli et al. 2013a). M105 exhibits a mild isophotal twist and an abrupt change of ellipticity at $R_{\text{maj}} \sim 30''$. The velocity map (ATLAS^{3D}) shows rotation at least within $R_{\text{maj}} \lesssim 30''$, but no embedded disk can be recognized in the unsharp mask, and the ellipticity profile is quite unusual for a spheroidal system with an inner disk. The data within the innermost $6''/1$ are excluded from the fit. A single Sérsic model does not provide a good description of the galaxy light profile. However, the addition of a second function (of any analytic form) to the model does not improve the fit. We conclude that the galaxy may not yet be fully relaxed, and we fit it with a single Sérsic profile.

systematic errors (e.g., incorrect sky subtraction, inaccurate masking of contaminating sources, erroneous choice of model components) and only marginally affected by random errors. For this reason, we developed a method to estimate the uncertainties on the best-fit parameters that takes into account systematic errors (see Figures 9–13).

We will use the results from our 1D galaxy decompositions to obtain improved black hole mass scaling relations. These results will be presented in a series of forthcoming papers.

5.1. Individual Galaxy Decompositions

For each galaxy, we show a figure and a table. The figure illustrates our 1D model and the galaxy isophotal parameters. The left panels refer to the major-axis R_{maj} , while the right panels refer to the equivalent-axis R_{eq} , i.e., the geometric mean of the major (a) and minor (b) axis ($R_{\text{eq}} = \sqrt{ab}$), equivalent to a circularized profile. The top panels display the galaxy surface brightness (μ) radial profiles obtained with a linear sampling. The black points are the observed data used in the fit, and the open points are the observed data excluded from the fit. The colored lines represent the individual (PSF-convolved) model components: red = Sérsic; dark blue = exponential; green = - Gaussian; cyan = Ferrer; gray = Gaussian ring; pink = PSF. The parameters for the Sérsic spheroid model are inset. The total (PSF-convolved) model is shown with a black dashed line. The residual profile ($\text{data} - \text{model}$) is shown as $\Delta\mu$ in the second row. The horizontal gray dashed line corresponds to an intensity equal to three times the rms of the sky background

fluctuations ($3 \times \text{rms}_{\text{sky}}$). Δ denotes the rms scatter of the fit in units of mag arcsec^{-2} . The lower six panels show the ellipticity (ϵ), position angle (PA), and fourth harmonic ($B4$) radial profiles from the ellipse. The tables report a comparison between our results (from both our 1D and 2D decompositions) and those obtained by the following authors: GD07 = Graham & Driver (2007a, who performed 1D fits along the major-axis), L+10 = Laurikainen et al. (2010, who performed 2D fits), S+11 = Sani et al. (2011, who performed 2D fits), B+12 = Beifiori et al. (2012, who performed 2D fits), V+12 = Vika et al. (2012, who performed 2D fits), R+13 = Rusli et al. (2013a, who performed 1D fits along the equivalent axis), and L+14 = Läsker et al. (2014a, who performed 2D fits). Each galaxy model is the sum of its individual components, which are expressed with the following nomenclature: (analytic function)-(physical component). The analytic functions can be: S = Sérsic, e = exponential, G = Gaussian, F = Ferrer, M = Moffat, and PSF. The physical components can be: bul = bulge (or spheroid), d = disk, id = inner disk, bar, n = nucleus, l = lens or oval, r = ring, halo, and spiral arms. When a nuclear component or a partially depleted core has been masked, we signal it as “m-n” or “m-c,” respectively. For example, the model “S-bul + e-d + e-id + m-n + G-r” reads “Sérsic-bulge + exponential-disk + exponential-(inner disk) + mask-nucleus + Gaussian-ring.” The core-Sérsic model used by Rusli et al. (2013a) is always implicitly associated with the galaxy spheroidal component. Graham & Driver excluded the innermost data points when fitting their galaxy light profiles; therefore, their

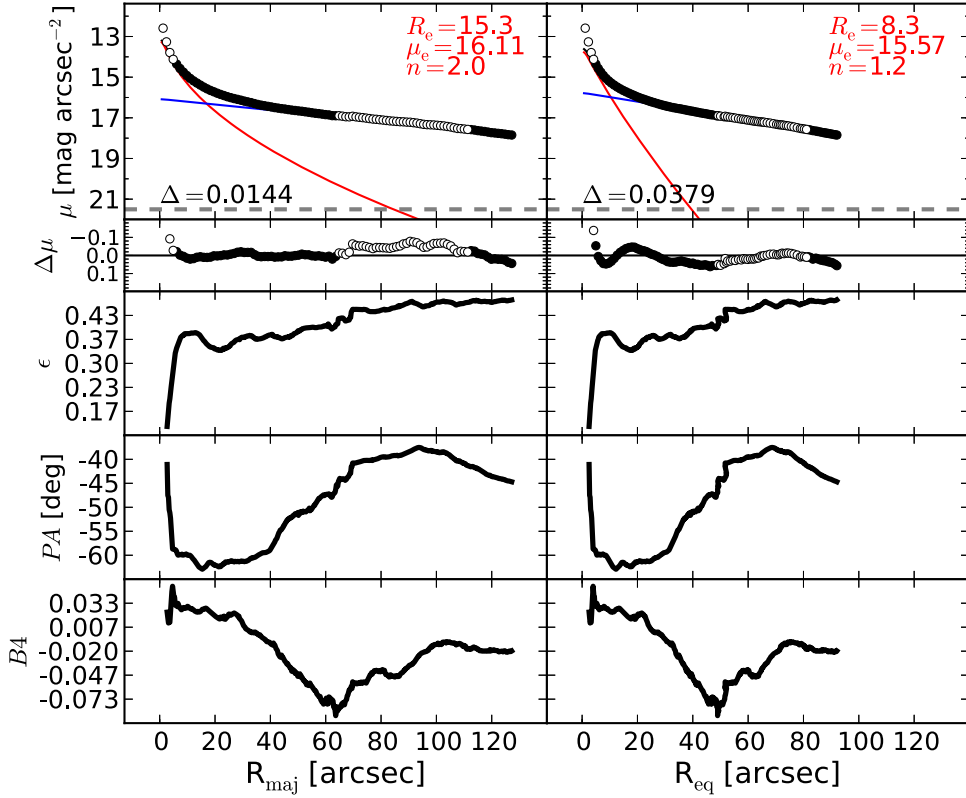


Figure 29. M106: a barred spiral galaxy, harboring a Seyfert AGN (Véron-Cetty & Véron 2006) with circumnuclear dust (Martini et al. 2003). We exclude from the fit the innermost $6''.1$ because it is affected by the AGN emission. The boxy bar, responsible for the minimum in the $B4$ profile at $R_{\text{maj}} \sim 65''$, is fainter than the large-scale disk, and in the light profile it is only detectable as a slight swelling within $65'' \lesssim R_{\text{maj}} \lesssim 110''$. This region is excluded from the fit. A peak in the ellipticity profile at $R_{\text{maj}} \sim 10''$ suggests the presence of a disky component embedded in the bulge, but a model that accounts for this component is degenerate with the other fitted components.

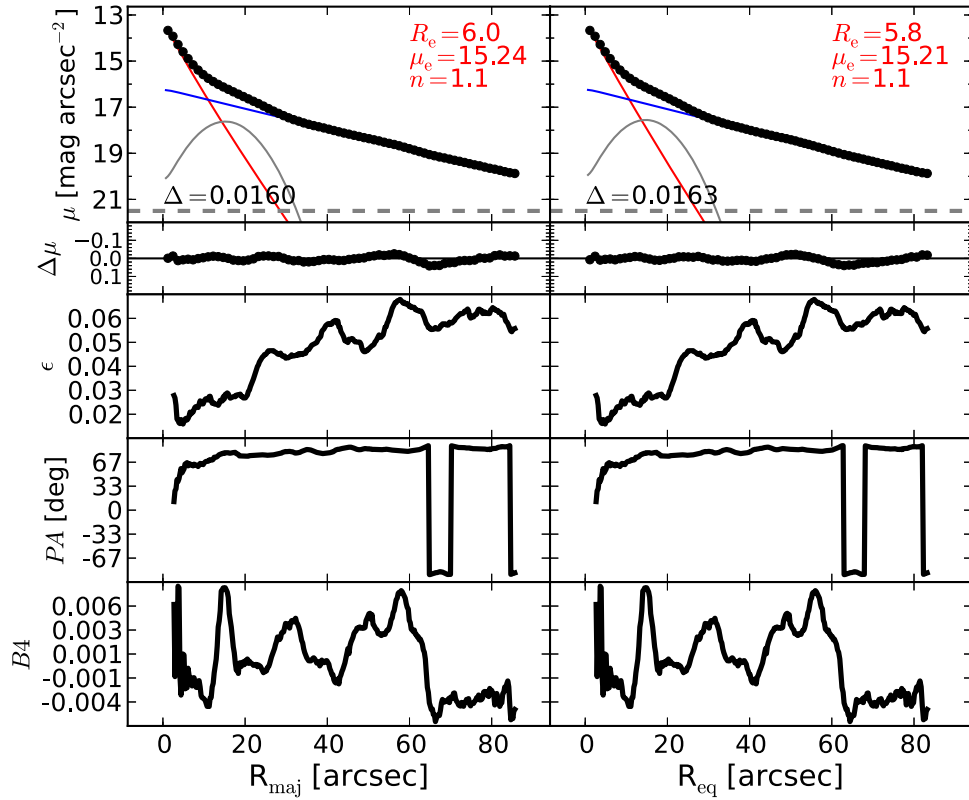


Figure 30. NGC 0524: an unbarred face-on lenticular galaxy. The unsharp mask of NGC 0524 reveals a faint multi-ring structure in the galaxy disk, with a substantial ring peaking at $R_{\text{maj}} \sim 20''$. We account for this brightest ring using a Gaussian ring profile.

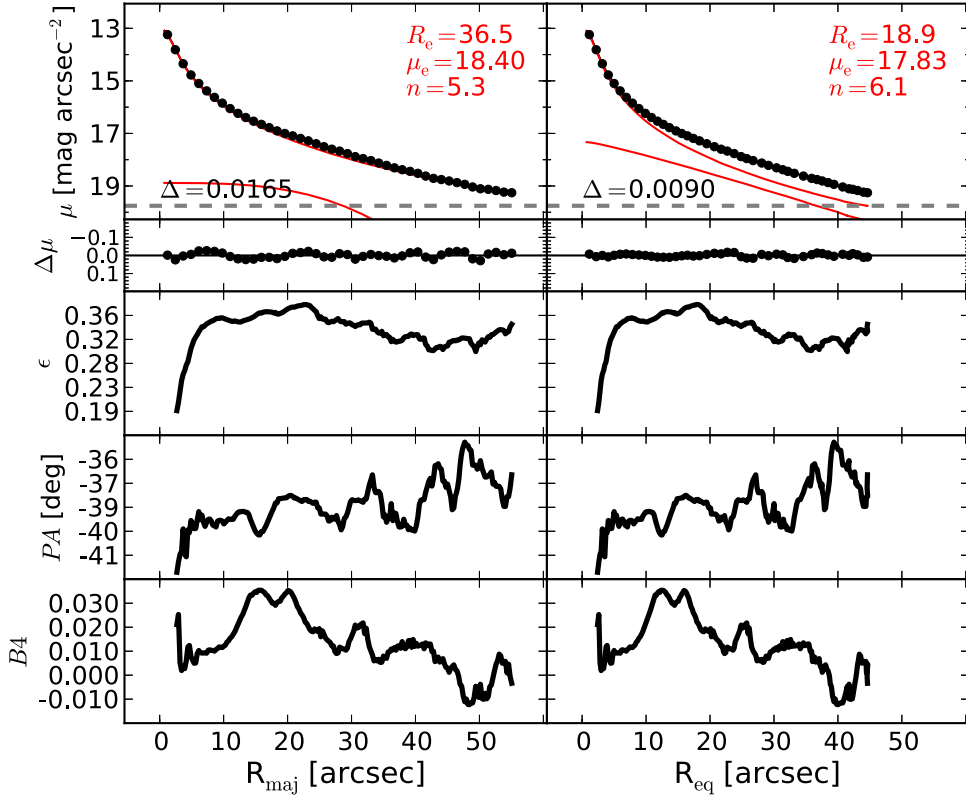


Figure 31. NGC 0821: an elliptical galaxy with an edge-on embedded disk. The ellipticity profile and the velocity map (ATLAS^{3D}, SLUGGS) show the presence of the faint intermediate-scale disk. Given its edge-on inclination, the disk is modeled with a low- n Sérsic function.

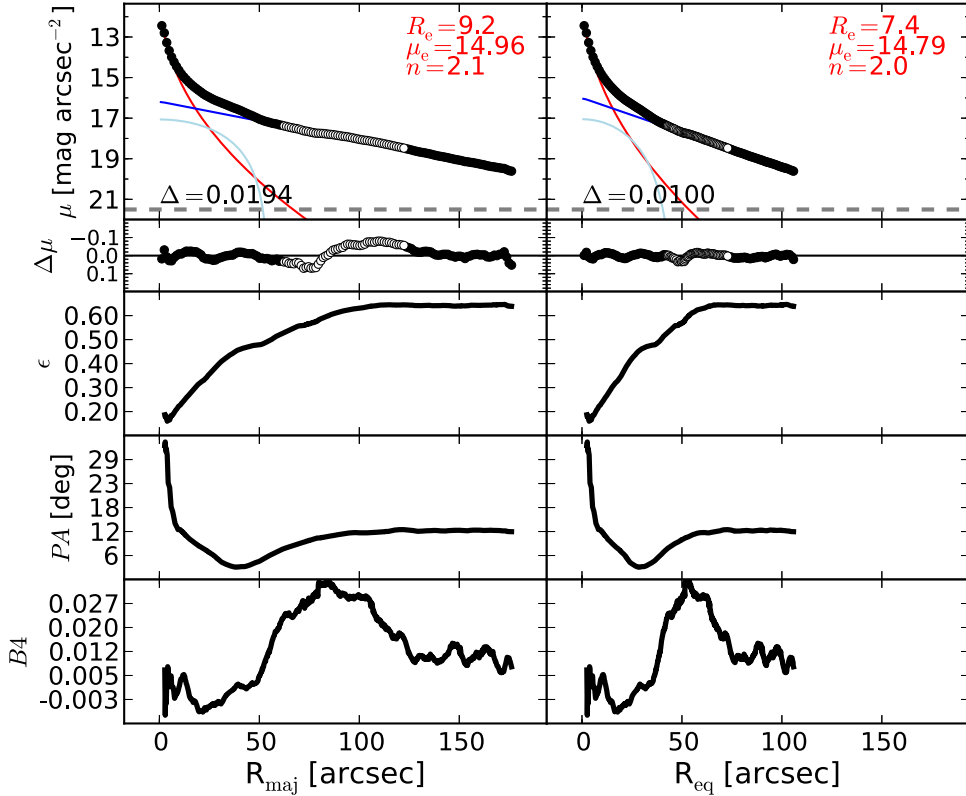


Figure 32. NGC 1023: a barred lenticular galaxy. The bar extends out to $R_{\text{maj}} \lesssim 40''$. Small deviations of the disk from a perfect exponential profile, within $60'' \lesssim R_{\text{maj}} \lesssim 125''$ (the data in this range are excluded from the fit), can be ascribed to faint residual spiral arms, also noticeable in the 2D residual image. The peak at $R_{\text{maj}} \sim 10''$ in the B4 profile signals the presence of an embedded (and faint) disk. The 1D residuals show a structure within $R_{\text{maj}} \lesssim 10''$ caused by this un-subtracted component, as also noted by Läsker et al. (2014a). Our attempts to account for the inner disk by adding a fourth function to the model did not significantly change the bulge best-fit parameters; thus, we elect not to model this embedded disk.

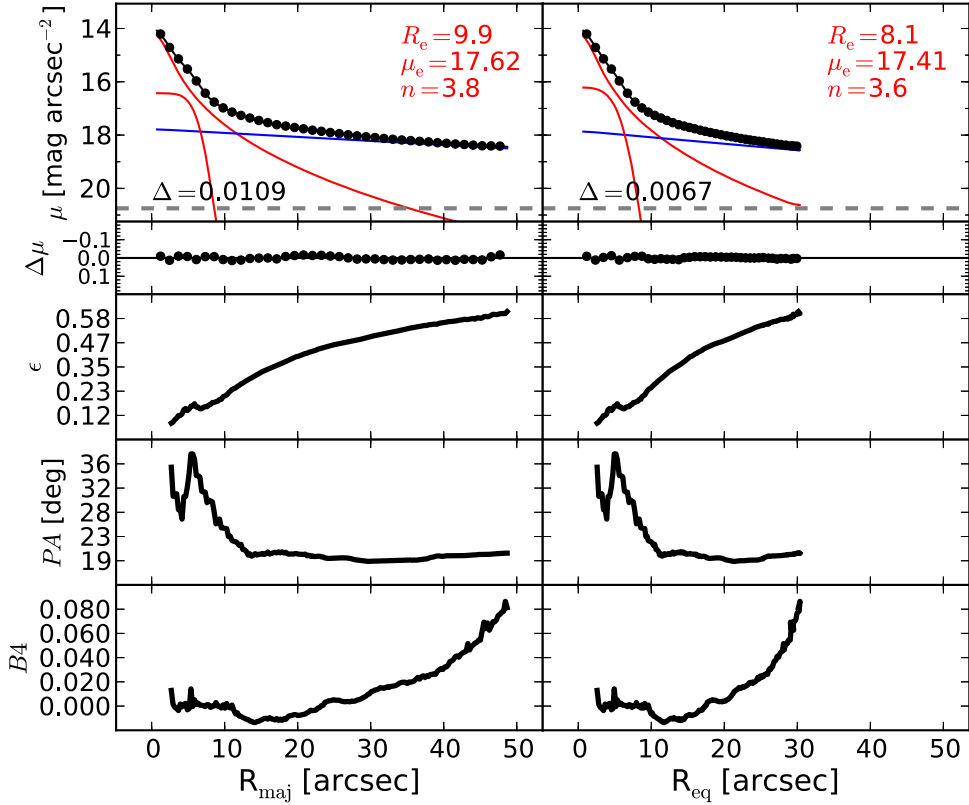


Figure 33. NGC 1300: a face-on, barred spiral galaxy. The morphology of NGC 1300 is quite complex. In addition to a large-scale disk and a bulge, the galaxy is composed of a large-scale bar that extends up to $R_{\text{maj}} \lesssim 90''$, two prominent spiral arms, and an inner disk-like component ($R_{\text{maj}} \lesssim 5''$), disclosed by the peaks in the ellipticity and PA profiles. We truncate the light profile at $R_{\text{maj}} \sim 50''$, and we fit the inner combination of the large-scale bar and the disk as a single component, using an exponential function. The embedded component is described with a low- n Sérsic profile.

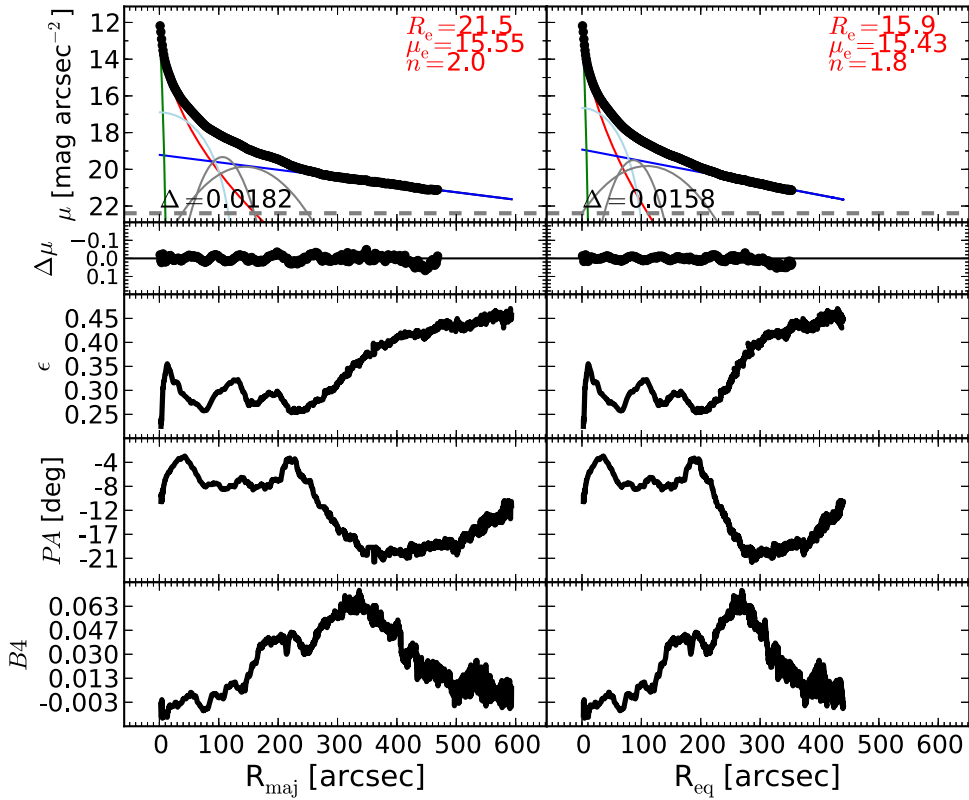


Figure 34. NGC 1316: a merger. The galaxy is composed of a bulge, an elongated structure that can be identified with a bar, two obvious rings, an outer exponential disk or halo, and a bright nuclear component.

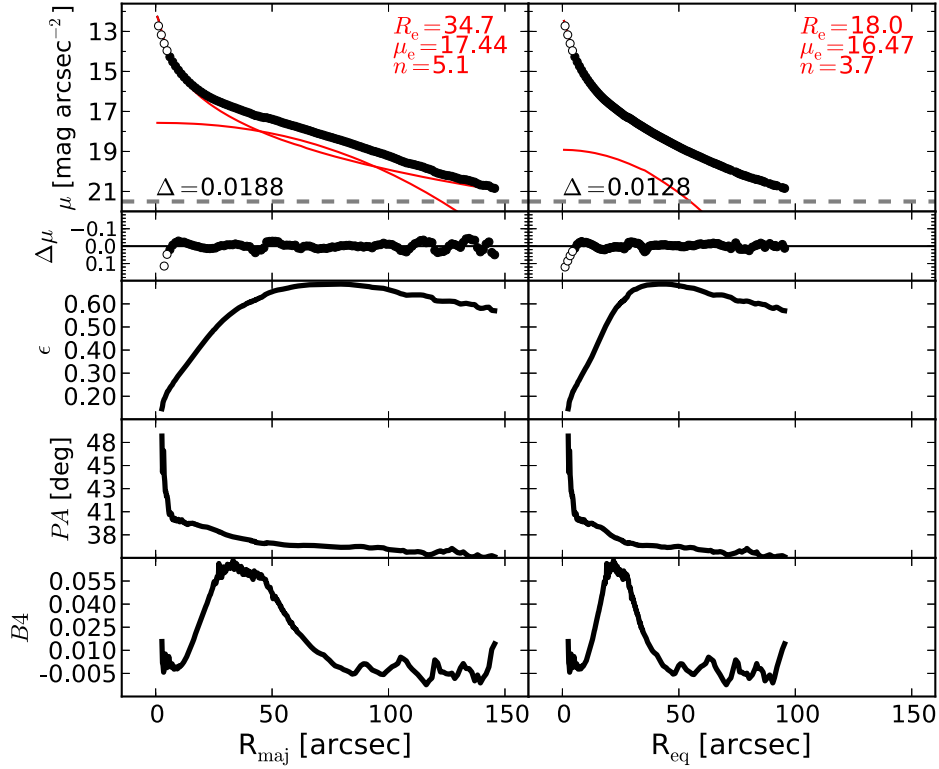


Figure 35. NGC 1332: an edge-on elliptical/lenticular galaxy. The identification of a disk is trivial owing to its edge-on orientation, although a visual inspection of the galaxy image is not enough to establish the radial extent of this disk. The ellipticity profile indicates that the disk is indeed intermediate-sized, i.e., it does not dominate at large radii. Given the edge-on inclination of this disk, we model it with a low- n Sérsic profile. The data within the innermost $6''$ are excluded from the fit. Our equivalent-axis decomposition returns a spheroidal component accounting for 95% of the total light, and an embedded disk accounting for the remaining 5%. In passing, we note that the bulge-disk decomposition performed by Rusli et al. (2011) on NGC 1332 is significantly different from our best-fit model. Rusli et al. (2011) did not identify the intermediate-scale embedded disk, but instead proposed a model featuring a Sérsic bulge ($n_{\text{sph}} \sim 2.3$, $R_{e,\text{sph}} \sim 8''$), accounting for 43% of the total light, and a large-scale exponential disk. This result led them to the conclusion that NGC 1332 is a [disk-dominated](#) lenticular galaxy and is displaced from the $M_{\text{BH}}-L_{K,\text{sph}}$ (black hole mass vs. K -band spheroid luminosity) relation of Marconi & Hunt (2003) by an order of magnitude along the M_{BH} direction. Instead, the galaxy spheroid is a factor of two more luminous than claimed by Rusli et al. (2011), and NGC 1332 is not an outlier in our $M_{\text{BH}}-L_{\text{sph}}$ diagram.

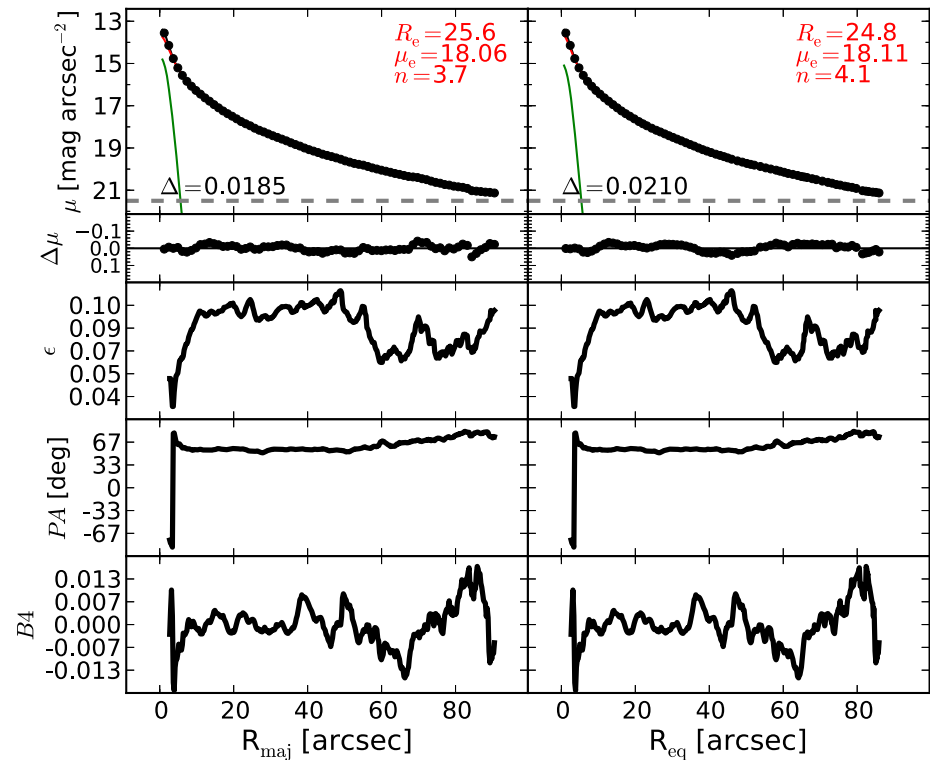


Figure 36. NGC 1374: an elliptical galaxy. A Gaussian function in our model accounts for the relatively faint additional nuclear component.

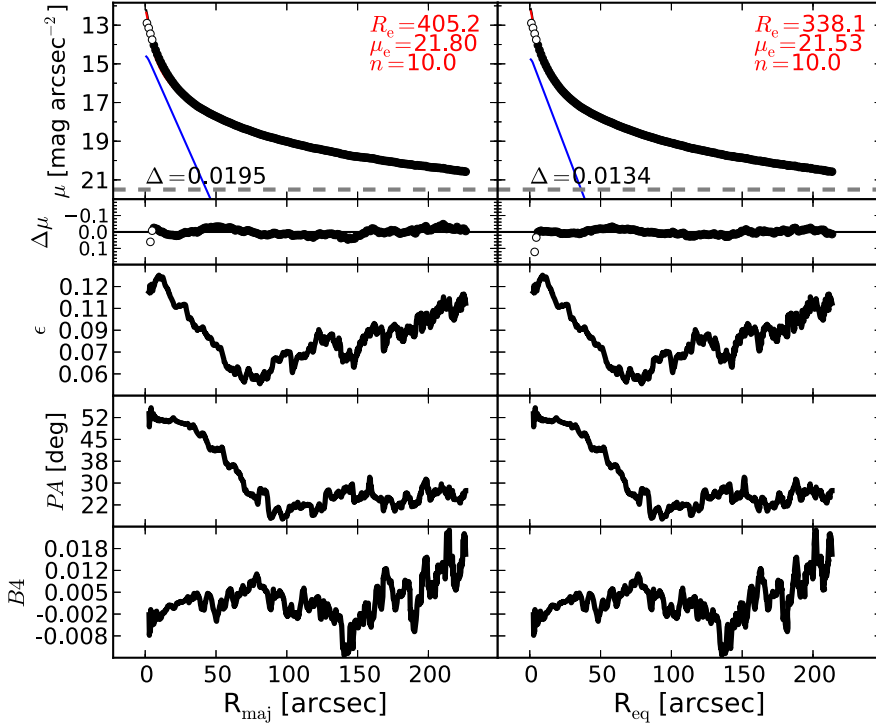


Figure 37. NGC 1399: the central galaxy of the Fornax Cluster, an elliptical galaxy with a slightly resolved partially depleted core (Rusli et al. 2013a; Dullo & Graham 2014). The nuclear activity of NGC 1399 is classified as Seyfert (Véron-Cetty & Véron 2006), but the galaxy lacks dust emission (Tran et al. 2001). The ellipticity and PA profiles display a steep decline with increasing radius within $R_{\text{maj}} \lesssim 60''$, suggesting the presence of an embedded disk. This inner component is also visible, although faint, in the unsharp mask. We note that, after excluding the innermost $6.''1$, a single Sérsic profile is not sufficient to describe the whole galaxy light profile. The addition of an inner exponential function to model the disk notably improves the fit.

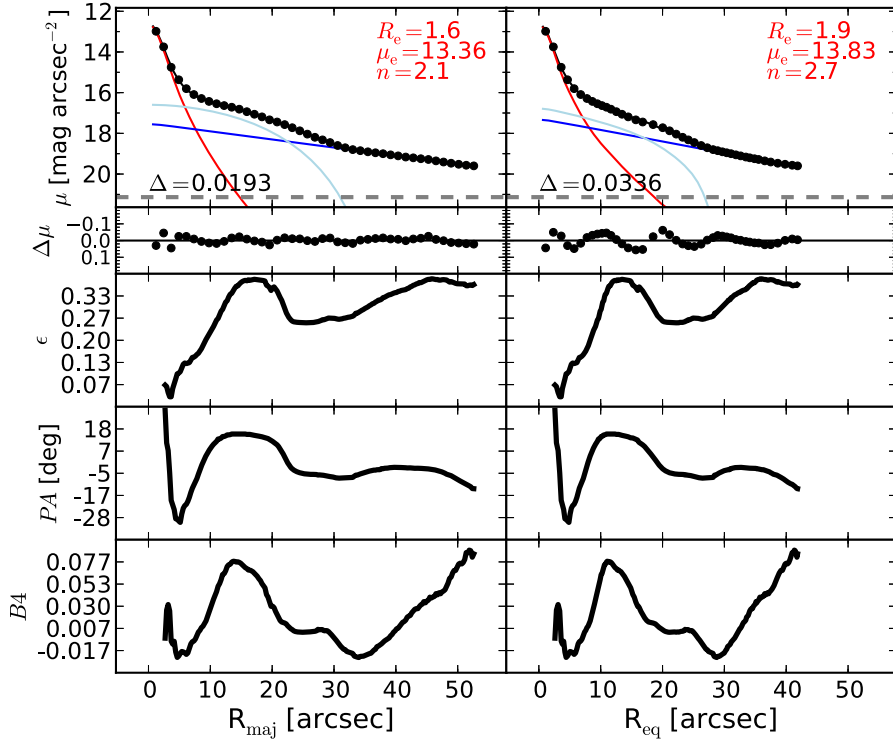


Figure 38. NGC 2273: a barred spiral galaxy with a Seyfert AGN (Contini et al. 1998) and circumnuclear dust (Simões Lopes et al. 2007). Its bar is surrounded by two tightly wound star-forming spiral arms that resemble a ring (Comerón et al. 2010). The bar of NGC 2273 extends out to $R_{\text{maj}} \lesssim 25''$. The pseudoring does not produce any evident swelling in the light profile; therefore, we do not account for it in the galaxy model. The isophotal parameters confirm the presence of a nuclear disk-like component within $R_{\text{maj}} \lesssim 5''$. However, as noted by Laurikainen et al. (2005), any attempt to account for the embedded disk resulted in a degenerate model. This is not surprising if one considers the poor spatial resolution of the galaxy image, with the effective radius of the bulge comparable to the FWHM of the instrumental PSF. Although NGC 2273 hosts an optical AGN and nuclear dust, no central excess of light is observed in the 1D residuals. The addition of a nuclear component to the model does not significantly improve the fit or change the bulge parameters.

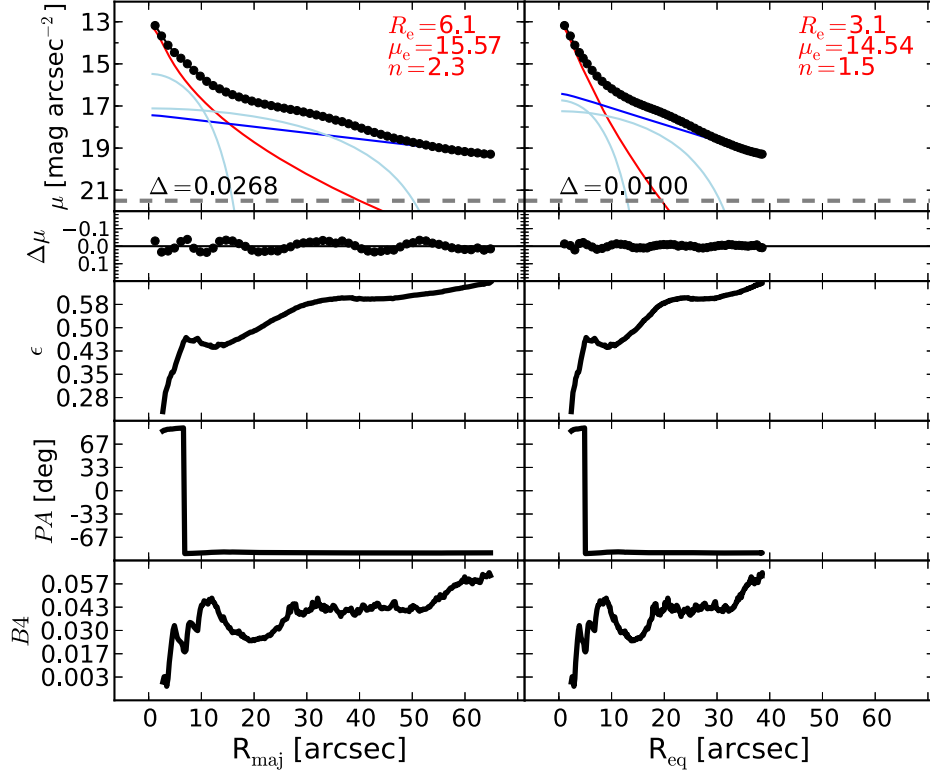


Figure 39. NGC 2549: an edge-on barred lenticular galaxy. Although the edge-on inclination of NGC 2549 complicates the identification of additional embedded components, a large-scale bar ($R_{\text{maj}} \lesssim 45''$) can be recognized in the galaxy image and—more easily—in the light profile. We model the large-scale bar with a Ferrer function. A peak in the ellipticity profile discloses the presence of a disky component embedded in the bulge ($R_{\text{maj}} \lesssim 10''$). This inner component can be spotted also by looking at the velocity map (ATLAS^{3D}), and we fit it with a Ferrer function.

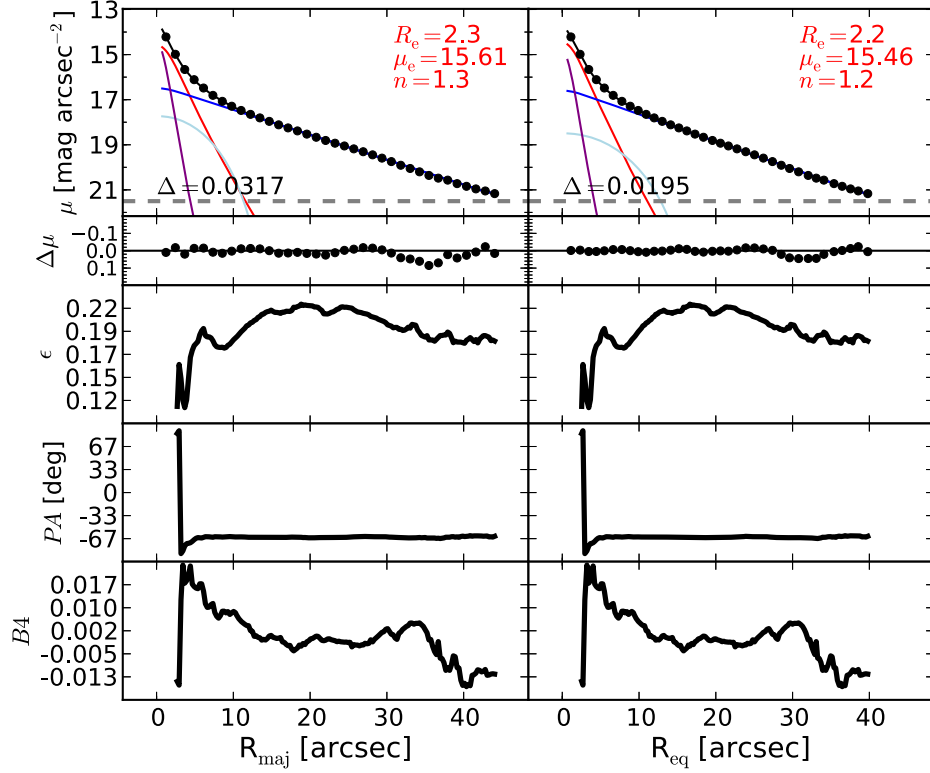


Figure 40. NGC 2778: a face-on lenticular galaxy. The peak in the ellipticity profile at $R_{\text{maj}} \sim 5''$ reveals the existence of a nuclear component embedded in the galaxy bulge. After an inspection of the unsharp mask, we identified this component with a small bar, which we model with a Ferrer function. We also account for some nuclear light excess by adding a PSF component to the model. We note that excluding the PSF component from our model does not significantly change the bulge effective radius, but it does increase the bulge Sérsic index to $n_{\text{sph}} \sim 2$.

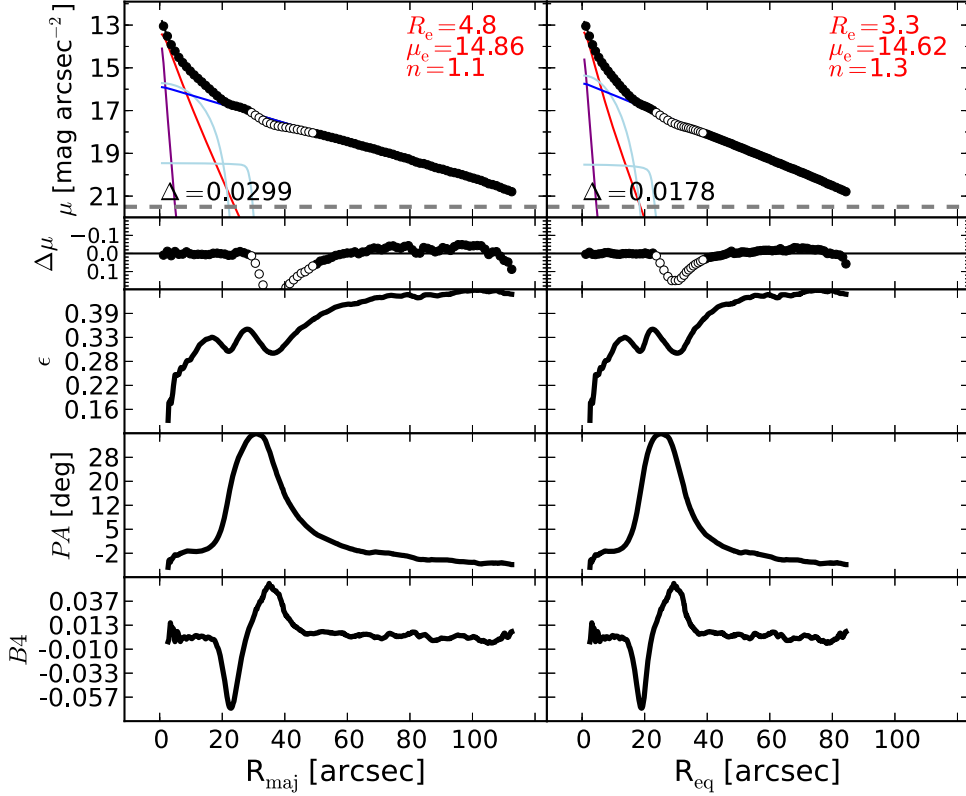


Figure 41. NGC 2787: a barred lenticular galaxy with LINER nuclear activity (Véron-Cetty & Véron 2006). An inner disk is embedded in the bulge of this galaxy (Erwin et al. 2003). NGC 2787 features a spectacular structure of dust rings at its center (Erwin & Sparke 2003) and a nuclear stellar disk (with size $\lesssim 1''.8$; Ledo et al. 2010). NGC 2787 has an undoubtedly complex morphology. This galaxy is composed of a bulge, a large-scale disk, a bar (see the peaks in the ellipticity, PA, and B4 profiles at $R_{\text{maj}} \sim 30''$) with two ansae, an inner disk (or bar?) embedded in the bulge (see the peak in the ellipticity profile at $R_{\text{maj}} \sim 17''$), and a bright nucleus. After masking the data affected by the ansae within $30'' \lesssim R_{\text{maj}} \lesssim 50''$, we use a Ferrer function for the bar, a second Ferrer function for the inner disk (or bar), and a PSF component for the nucleus.

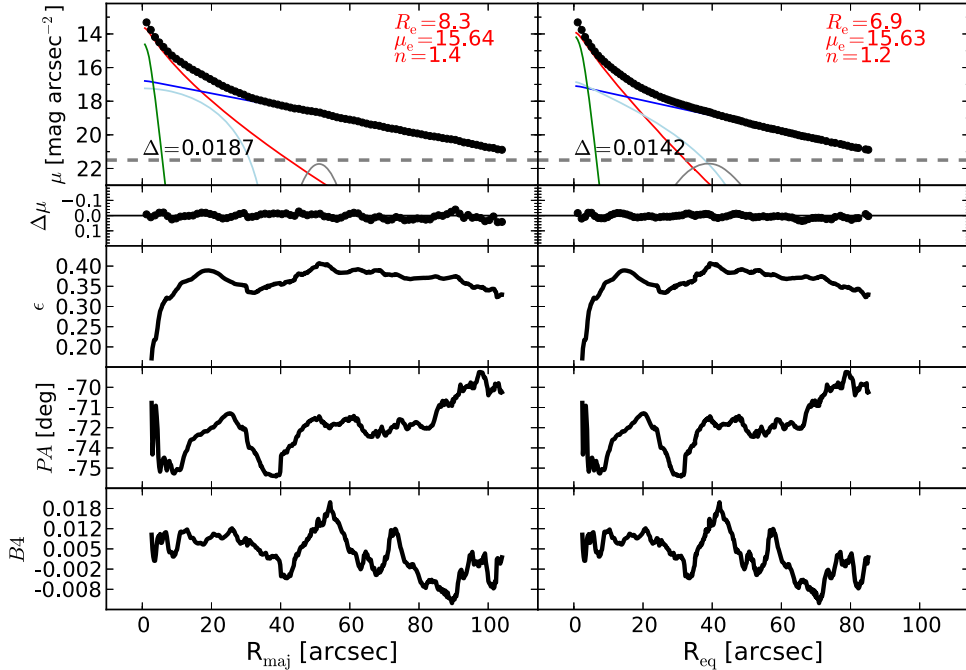


Figure 42. NGC 2974: a spiral galaxy that has been misclassified as an elliptical galaxy in the RC3 catalog. The galaxy hosts a Seyfert AGN (Véron-Cetty & Véron 2006) and filamentary dust in its center (Tran et al. 2001). From an inspection of the unsharp mask, we identified a ring structure at $R_{\text{maj}} \sim 50''$, probably a residual of two tightly wound spiral arms, and an elongated bar-like component within $R_{\text{maj}} \lesssim 30''$, which we fit with a Ferrer function. The pseudoring produces a peak in the B4 profile at $R_{\text{maj}} \sim 50''$, and the bar produces a peak in the ellipticity profile at $R_{\text{maj}} \sim 20''$. Although the ring is extremely faint, it is important to account for it in the galaxy decomposition. A model without the ring component results in a “steeper” exponential disk (i.e., the disk would have a smaller scale length and a brighter central surface brightness) and produces poor residuals within $R_{\text{maj}} \lesssim 40''$. The nuclear component is fit with a Gaussian profile.

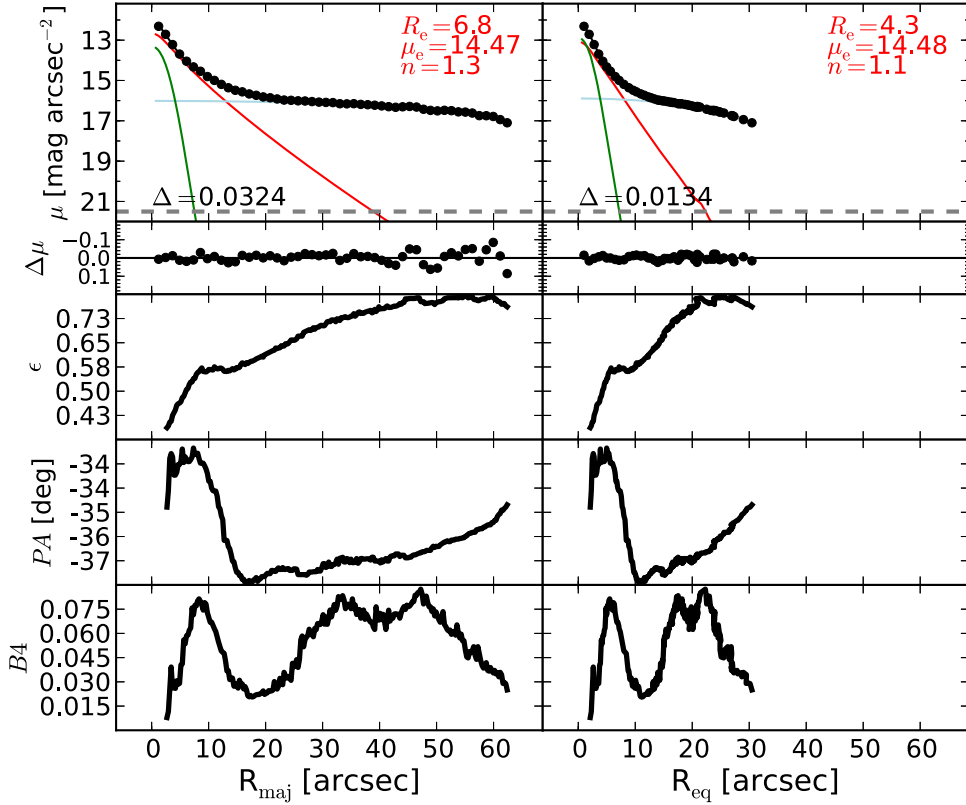


Figure 43. NGC 3079: an edge-on, late-type barred spiral galaxy with a Seyfert AGN (Véron-Cetty & Véron 2006) and circumnuclear dust (Martini et al. 2003). The bar extends out to $R_{\text{maj}} \gtrsim 70''$. We truncate the light profile at $R_{\text{maj}} \sim 65''$, before the “edge” of the bar, and we successfully model the combination of the disk and the bar with a Ferrer function. A Gaussian function accounts for the AGN emission.

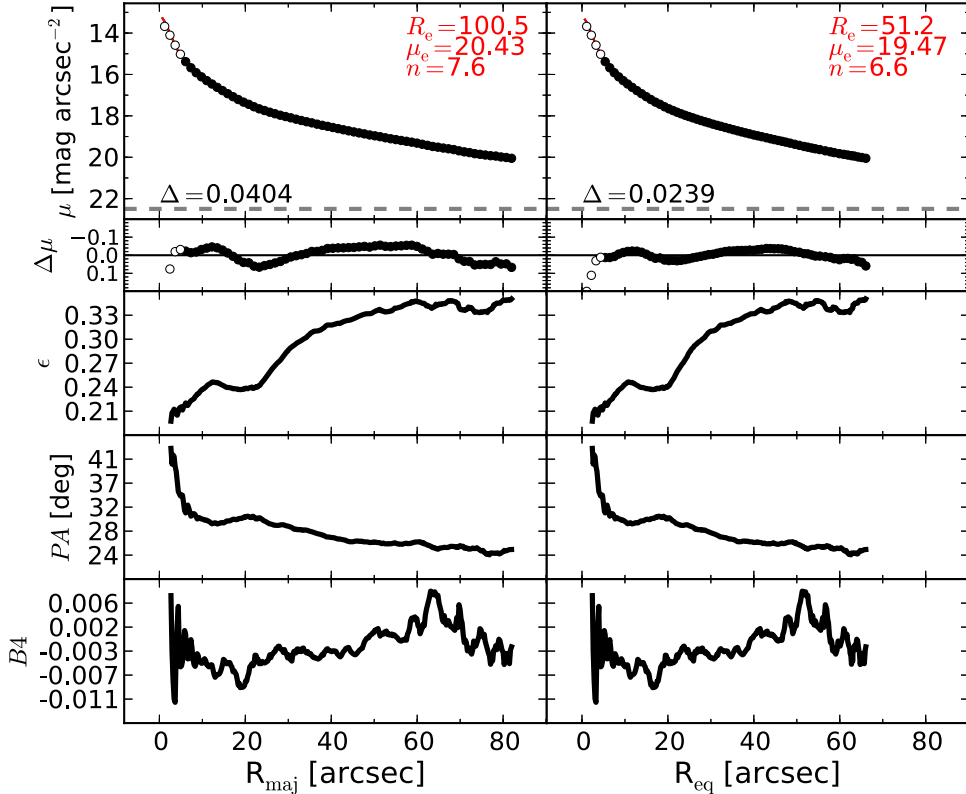


Figure 44. NGC 3091: an elliptical galaxy with an unresolved partially depleted core (Rusli et al. 2013a). The data within the innermost $6.''1$ are excluded from the fit. A faint embedded component ($R_{\text{maj}} \lesssim 10''$) can be recognized in the unsharp mask and has a corresponding peak in the ellipticity profile. This extra component is clearly visible in the residual image obtained by subtracting a 2D Sérsic model from the galaxy image. However, any attempt to account for the embedded component resulted in an unsatisfactory fit and did not significantly change the bulge parameters. We thus elect not to model the inner component.

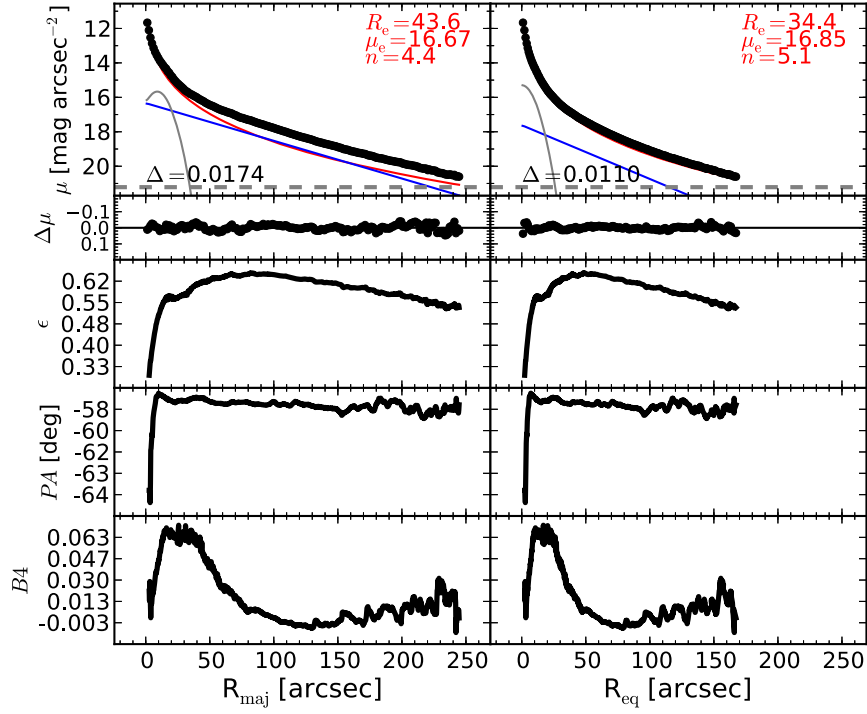


Figure 45. NGC 3115: [an edge-on elliptical/lenticular galaxy](#). This galaxy features an intermediate-scale disk and a nuclear stellar disk (with size $\sim 1''$; Scorz & Bender 1995; Ledo et al. 2010). The presence of the intermediate-scale disk is immediately evident by looking at the ellipticity and B_4 profiles. From the galaxy center to the outskirts, the ellipticity increases until it reaches a maximum ($\epsilon \sim 0.65$) at $R_{\text{maj}} \sim 90''$. After this point, it starts declining, being as low as $\epsilon \sim 0.55$ at $R_{\text{maj}} \sim 240''$. The galaxy isophotes display a positive diskyness within $R_{\text{maj}} \sim 90''$, but become perfect ellipses ($B_4 \sim 0$) beyond that point. Because galaxy disks typically have fixed ellipticity, reflecting their inclination to our line of sight, the previous observations tell us that, going from the galaxy center to the outer regions, the disk of NGC 3115 becomes increasingly important relative to the spheroid light, reaching its maximum at $R \sim 90''$. Beyond $R_{\text{maj}} \gtrsim 90''$, the contribution from the disk light starts declining more rapidly than the spheroid light. This interpretation is supported by the results of Arnold et al. (2011), who found that, within $R_{\text{maj}} \sim 110''$, the bulge of NGC 3115 is flattened and rotates rapidly ($v/\sigma \gtrsim 1.5$), whereas at larger radii the rotation declines dramatically (to $v/\sigma \sim 0.7$), but remains well aligned with the inner regions. From an inspection of the unsharp mask, we identify a faint nuclear edge-on ring ($R_{\text{maj}} \sim 15''$), which produces a corresponding peak in the ellipticity profile. We do not observe any nuclear excess of light in the 1D residuals. The addition of a PSF component to the final model does not significantly change the outcome of the fit.

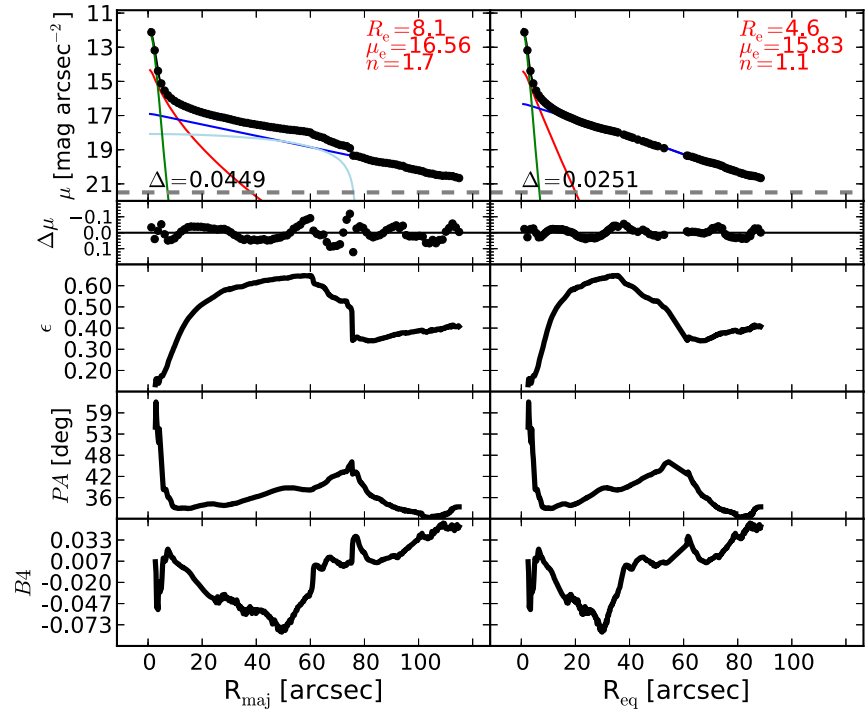


Figure 46. NGC 3227: [a spiral galaxy with a large-scale bar](#). This galaxy hosts a Seyfert AGN (Khachikian & Weedman 1974) and circumnuclear dust (Martini et al. 2003). The large-scale bar produces an evident bump in the major-axis surface brightness profile, which is absent in the equivalent-axis profile. We model the bar with a Ferrer function and the nucleus with a Gaussian function. The Ferrer component is rejected by the equivalent-axis fit.

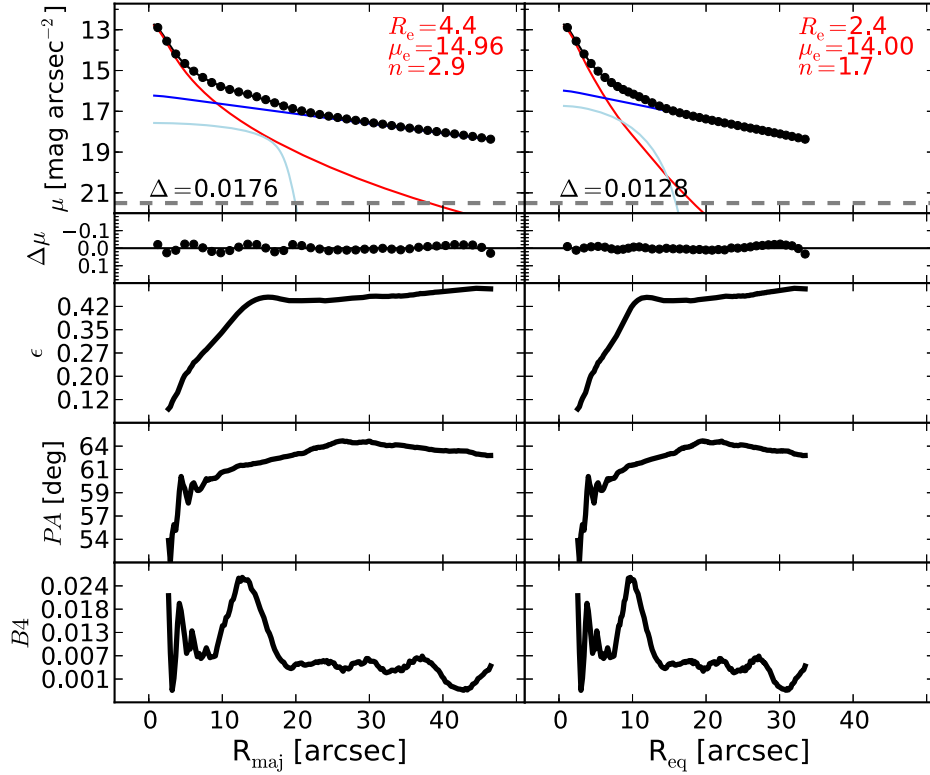


Figure 47. NGC 3245: a lenticular galaxy. The unsharp mask reveals the presence of an embedded disk ($R_{\text{maj}} \lesssim 15''$), confirmed by the corresponding peaks in the ellipticity and $B4$ profiles. We model this inner component with a Ferrer function.

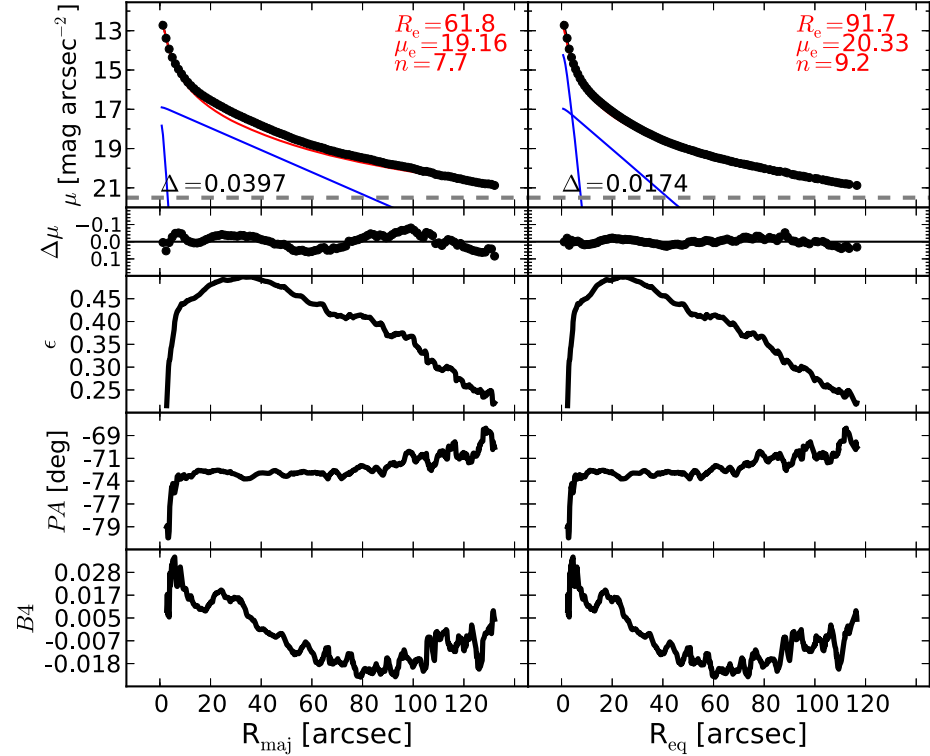


Figure 48. NGC 3377: an elliptical galaxy with an intermediate-scale disk and a nuclear stellar disk (Ledo et al. 2010). For this galaxy, Arnold et al. (2014) reported a strong decline in local specific angular momentum beyond $\sim 35''$, with a disk-to-bulge transition occurring at about $R_{\text{maj}} \sim 50''$. Arnold et al. (2014) attempted a three-component decomposition (accounting for a bulge, an embedded disk, and a central cusp), but unfortunately they fit the spheroidal component with a limited two-parameter $R^{1/4}$ function rather than a three-parameter $R^{1/n}$ Sérsic function. Here we use a surface brightness profile twice as extended as that used by Arnold et al. (2014), and we identify a nuclear disk and an intermediate-scale disk, both embedded in a larger spheroidal component. The presence of the intermediate-scale disk is also evident in the unsharp mask of the image mosaic and also from the ellipticity, which increases with increasing radius until $R_{\text{maj}} \sim 45''$ and then drops at larger radii. The nuclear stellar disk can be spotted from the peak at $R_{\text{maj}} \sim 5''$ in the $B4$ profile. Each of the two disks is modeled with an exponential profile.

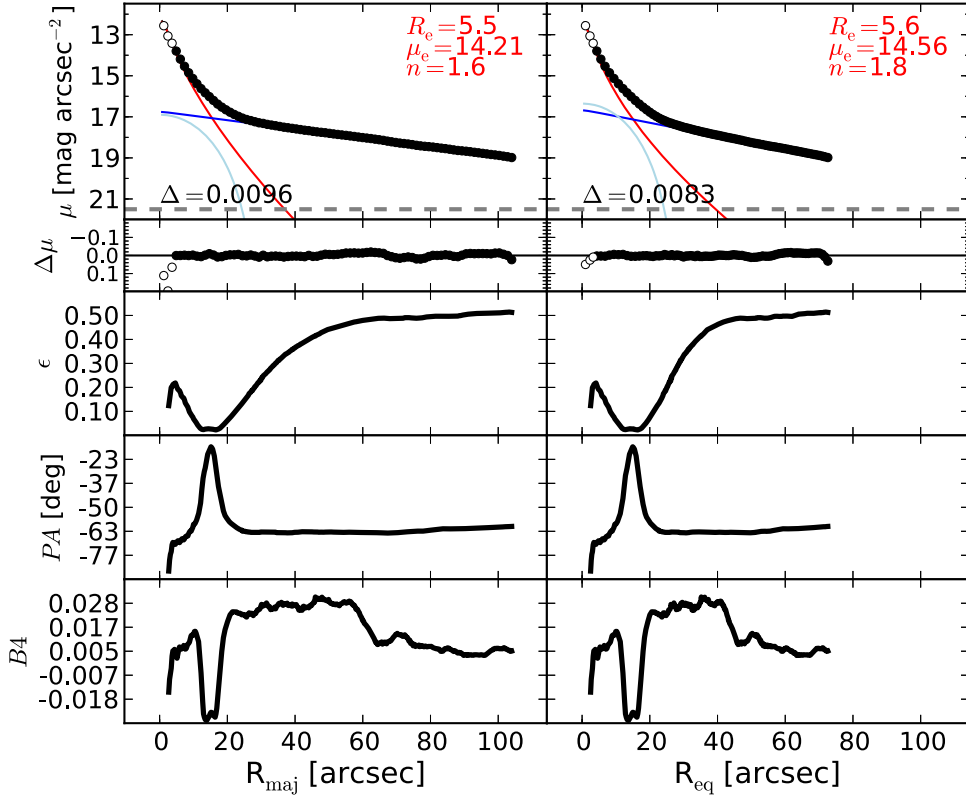


Figure 49. NGC 3384: a barred lenticular galaxy that hosts an embedded disk (with size $\lesssim 11''$; Erwin 2004) and a nuclear stellar disk (with size $\lesssim 0.8''$; Ledo et al. 2010). The isophotal parameters show clearly the presence of a boxy bar that extends out to $R_{\text{maj}} \lesssim 18''$. We model the bar with a Ferrer function. An embedded disk can be seen in the unsharp mask and produces the peak in the ellipticity profile at $R_{\text{maj}} \sim 4''$. However, any attempt to account for this component resulted in a degenerate model. We elect to fit neither the embedded disk nor the nuclear disk, by excluding from the fit the data within $R_{\text{maj}} < 3''$.

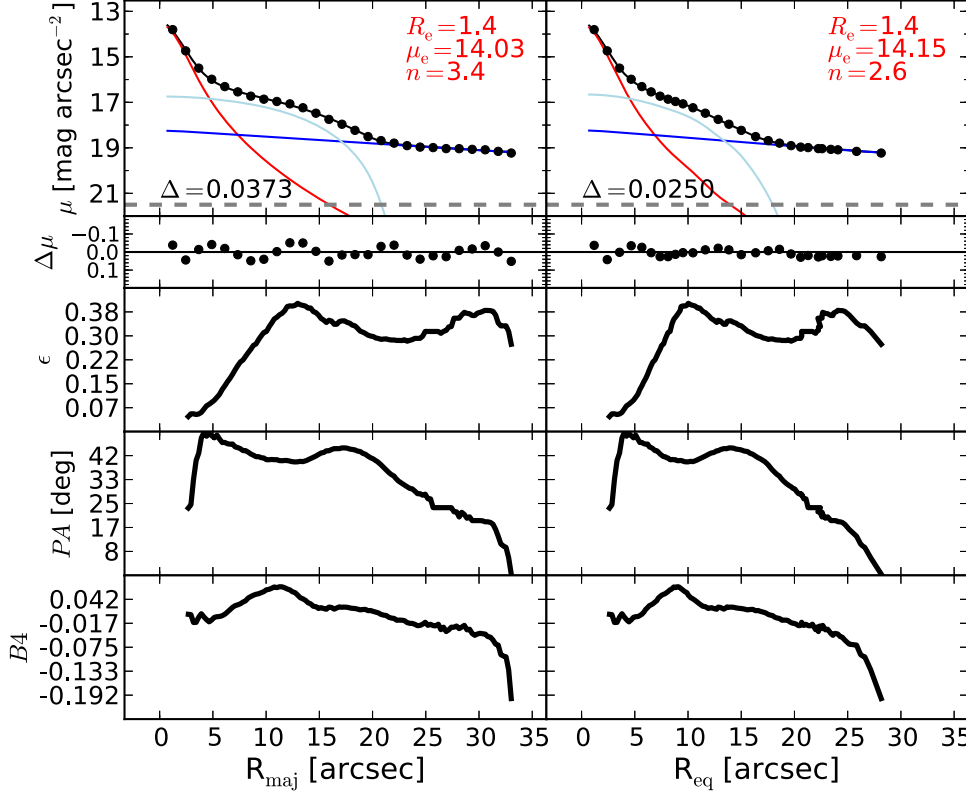


Figure 50. NGC 3393: an edge-on spiral galaxy hosting a Seyfert AGN (Diaz et al. 1988) and circumnuclear dust (Martini et al. 2003). The galaxy has a large-scale bar and a nuclear bar (with size $\lesssim 3''$, Erwin 2004). The large-scale bar ($R_{\text{maj}} \lesssim 20''$) is modeled with a Ferrer function. We do not model the nuclear bar and the AGN component because the poor spatial resolution of the data does not allow us to fit them.

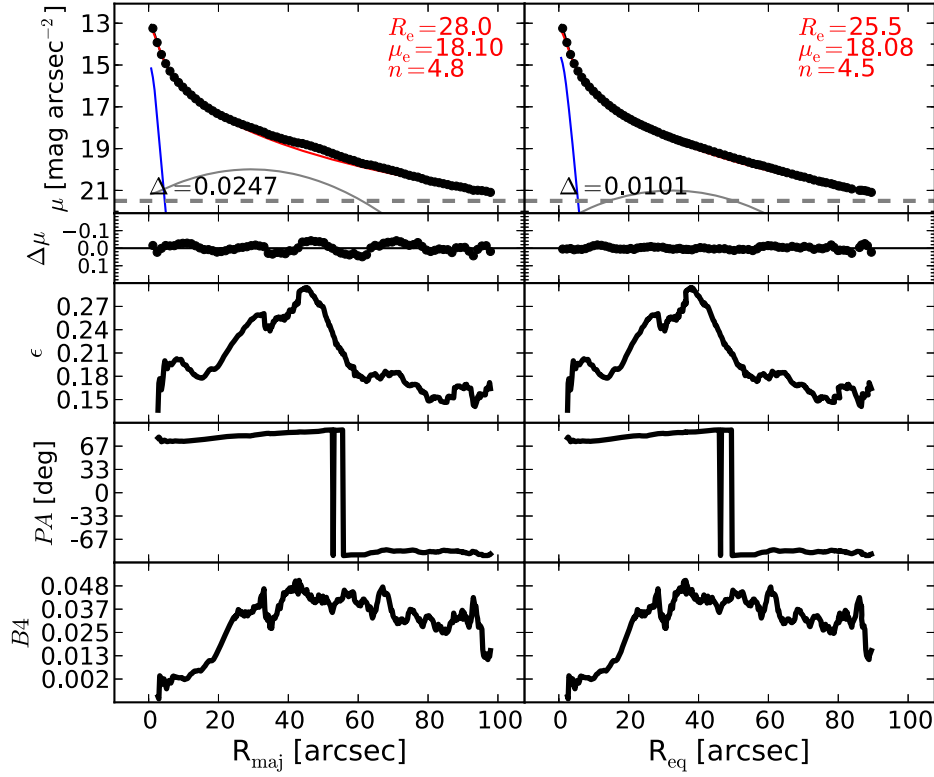


Figure 51. NGC 3414: a peculiar lenticular/elliptical galaxy. Different interpretations have been proposed about the morphology of this galaxy. Whitmore et al. (1990) suggested that NGC 3414 is a spheroidal galaxy with a large-scale edge-on polar ring, rather than a face-on barred lenticular galaxy. Laurikainen et al. (2010) decomposed NGC 3414 as a barred lenticular galaxy, but they cautioned against the uncertainty of their solution owing to the possible misinterpretation of the galaxy morphology. The unsharp mask clearly shows that an embedded component does not extend all the way through the center of the galaxy, but instead it is truncated at $R_{\text{maj}} \sim 20''$. However, an elongated structure in the galaxy center resembles a nuclear edge-on disk ($R_{\text{maj}} \lesssim 5''$). The velocity map (ATLAS^{3D}) shows rotation within $R_{\text{maj}} \lesssim 5''$, no rotation within $5'' \lesssim R_{\text{maj}} \lesssim 15''$, and counterrotation beyond $R_{\text{maj}} \gtrsim 15''$. The velocity pattern is consistent with the galaxy being a spheroidal system containing an edge-on polar ring and an edge-on nuclear disk.

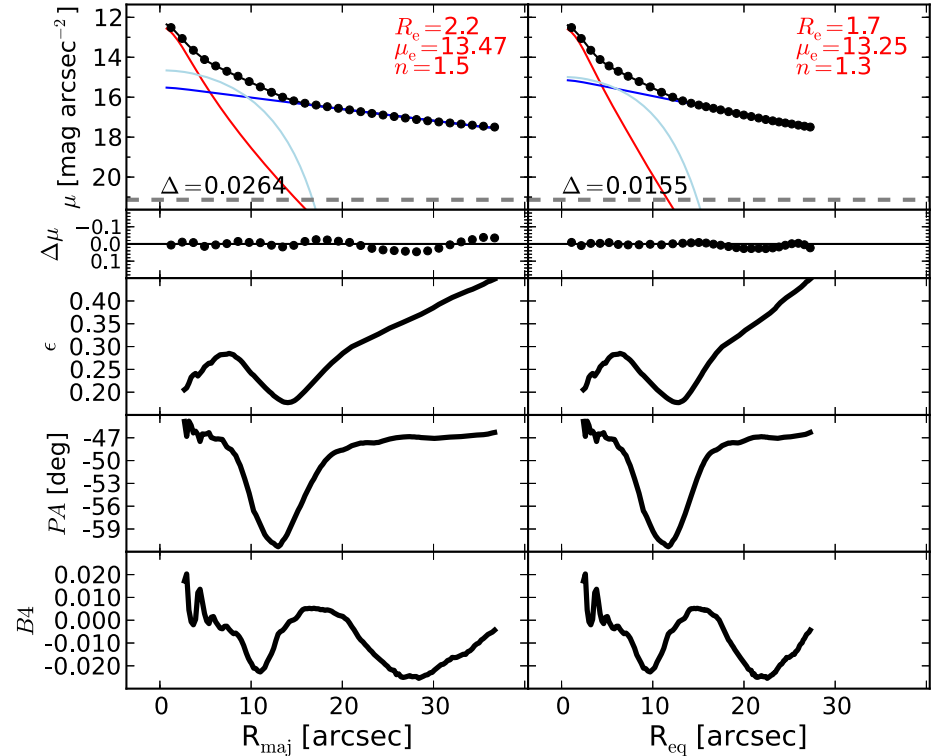


Figure 52. NGC 3489: a barred lenticular galaxy. Its disk has a smooth antitruncation at $R_{\text{maj}} \sim 85''$ (Erwin et al. 2008). The bar is fit with a Ferrer function.

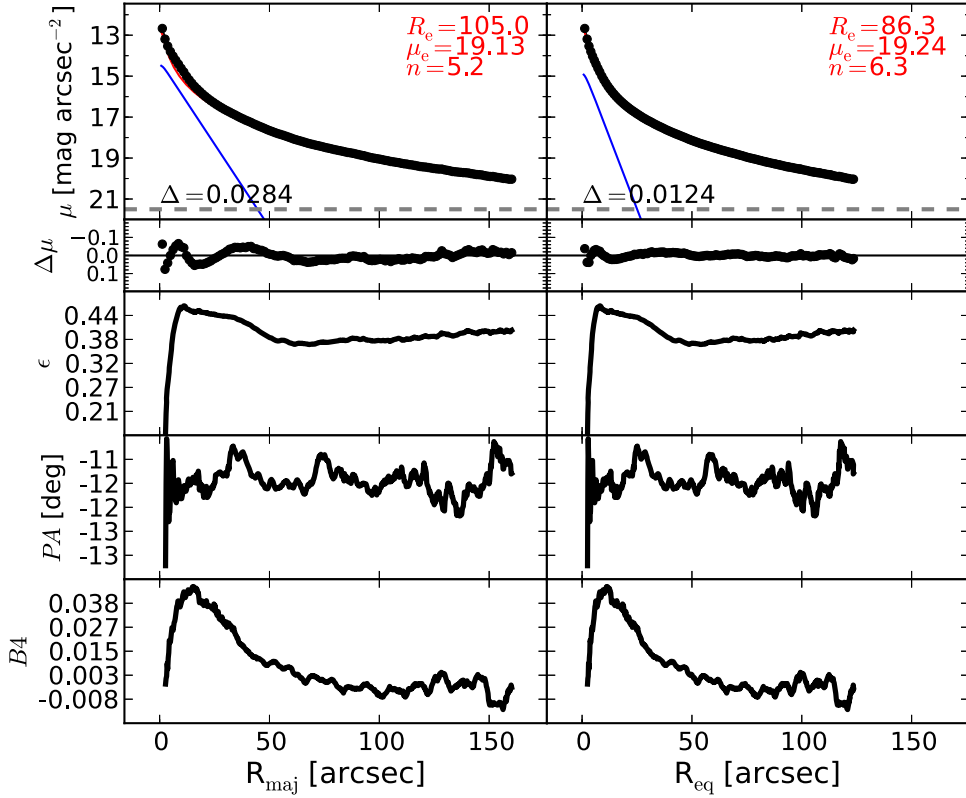


Figure 53. NGC 3585: an elliptical galaxy with an embedded disk (Scorza & Bender 1995). The embedded disk is visible in the unsharp mask and modeled with an exponential function.

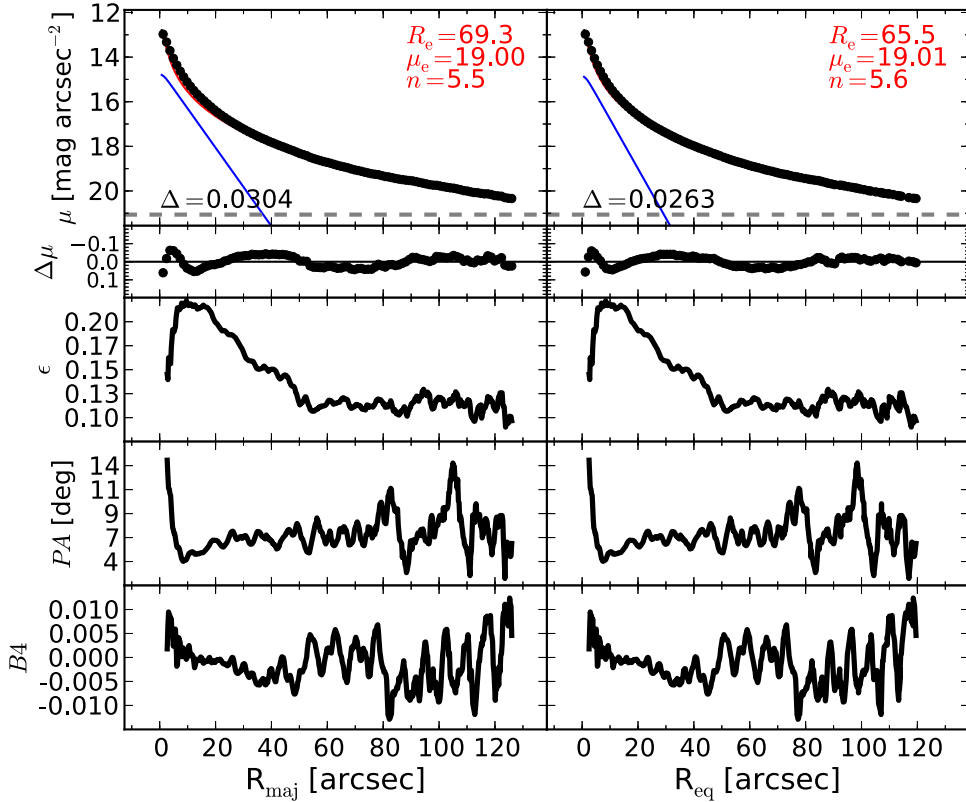


Figure 54. NGC 3607: an elliptical galaxy with an embedded disk. The velocity map (ATLAS^{3D}) shows rotation only within $R_{\text{maj}} \lesssim 20''$.

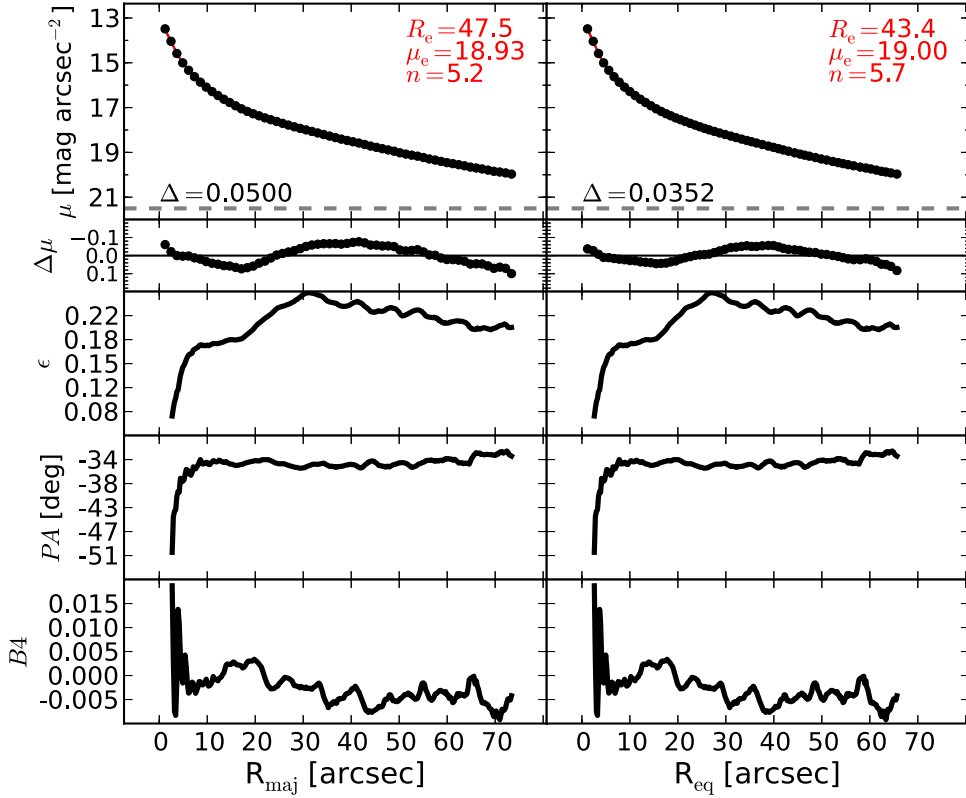


Figure 55. NGC 3608: an elliptical galaxy with an unresolved partially depleted core (Rusli et al. 2013a) and a kinematically decoupled core (ATLAS^{3D}, SLUGGS). We find that masking the nuclear region of this galaxy is unnecessary, and we fit the light profile with a single Sérsic model.

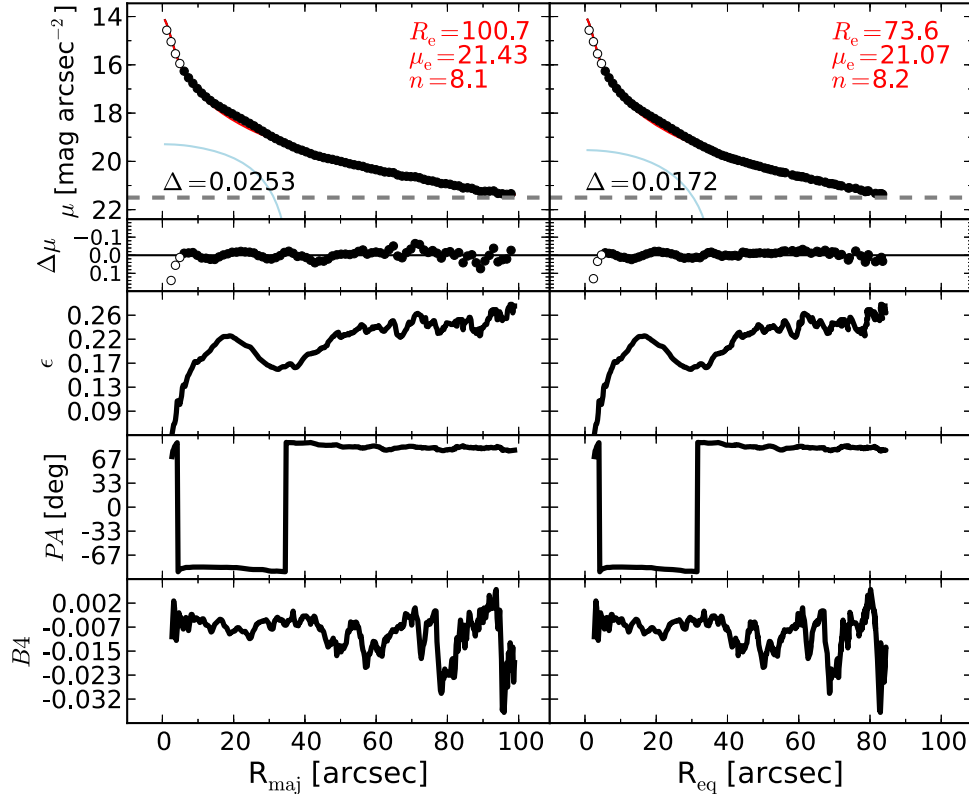


Figure 56. NGC 3842: the brightest member of the Leo Cluster (Abell 1367), an elliptical galaxy with an unresolved partially depleted core (Rusli et al. 2013a; Dullo & Graham 2014). The light profile presents a swelling at $R_{\text{maj}} \sim 20''$, and the ellipticity profile has a peak in the same position. One can also glimpse a faint elongated oval in the unsharp mask. The innermost $6.''1$ are excluded from the fit. A single Sérsic model is not sufficient to provide a good description of the galaxy light profile; therefore, we add a second component (Ferrer function) to account for the embedded lens.

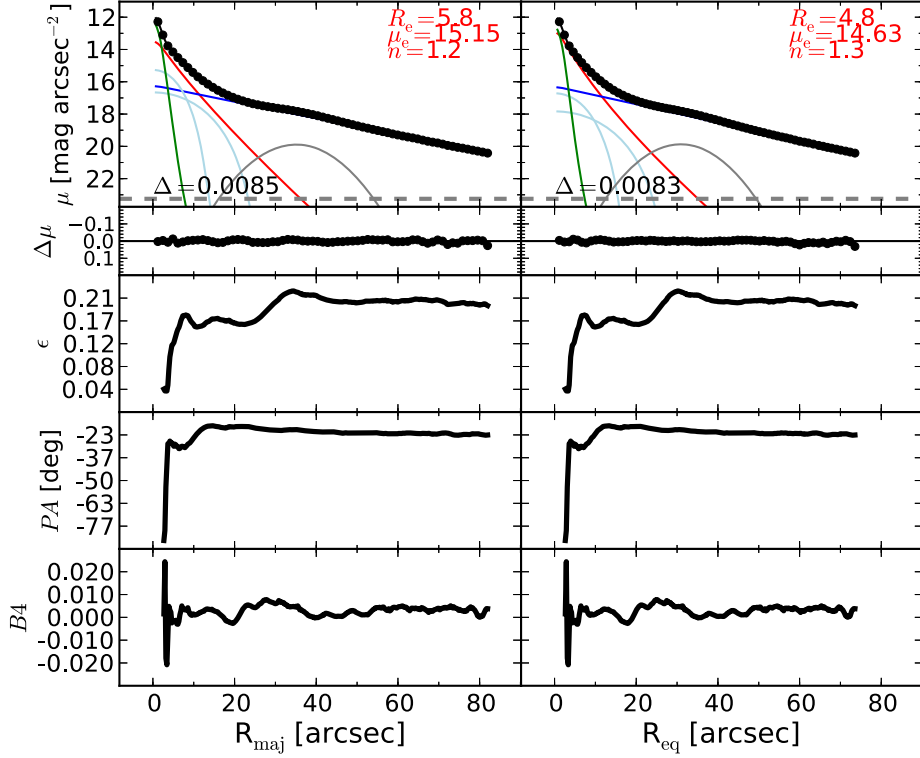


Figure 57. NGC 3998: a barred lenticular galaxy with a Seyfert AGN and nuclear dust (Knapp et al. 1996). Despite its large stellar velocity dispersion, this galaxy does not have a partially depleted core. Gutiérrez et al. (2011) identified a bar at $R_{\text{maj}} \lesssim 8''$, a ring between $30'' \lesssim R_{\text{maj}} \lesssim 50''$, and an antitruncation in the light profile of the disk at $R_{\text{maj}} \sim 122''$. Laurikainen et al. (2010) found that NGC 3998 features a weak bar at $R_{\text{maj}} < 8''$, a bright lens at $R_{\text{maj}} < 15''$, and a weak bump in the surface brightness profile at $R_{\text{maj}} \sim 40''$. We see three distinct peaks in the ellipticity profile. The first two peaks occur at $R_{\text{maj}} \sim 7''$ and $R_{\text{maj}} \sim 15''$, and they correspond to a weak bar and to a faint oval component, respectively. These components are fit with two Ferrer functions. The third peak at $R_{\text{maj}} \sim 35''$ coincides with a bump in the surface brightness profile and is produced by a ring. The AGN component is modeled with a Gaussian profile.

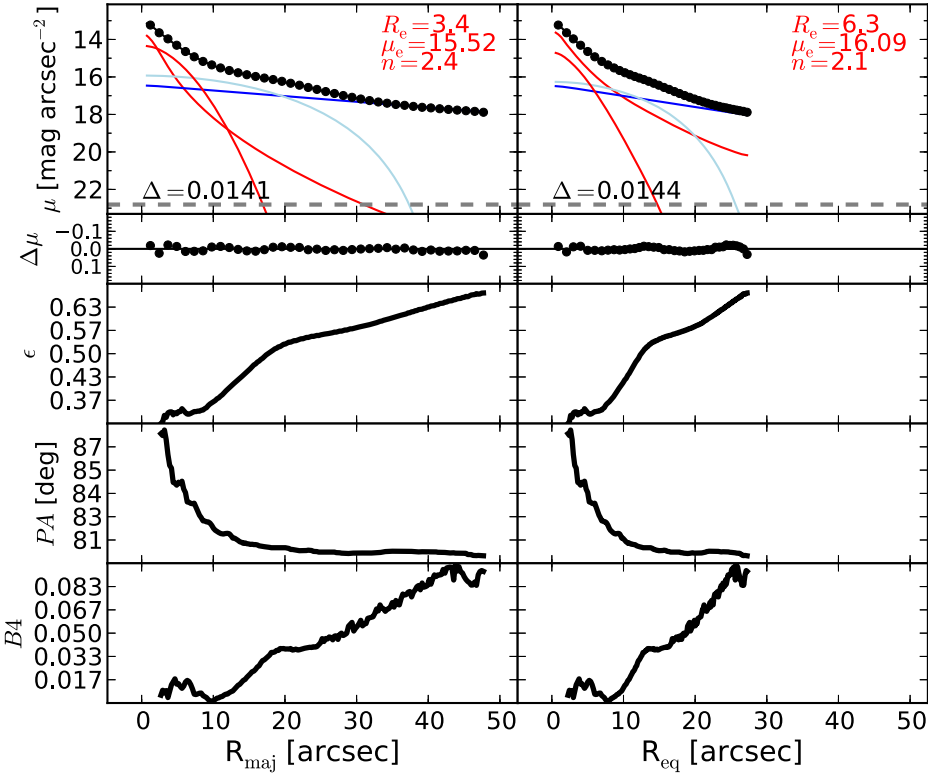


Figure 58. NGC 4026: an edge-on lenticular galaxy with a nuclear stellar disk (with size $\lesssim 0''.5$; Lledo et al. 2010). The unsharp mask reveals the presence of a bar ($R_{\text{maj}} \lesssim 30''$) and a disky component embedded in the bulge that is responsible for the peak at $R_{\text{maj}} \sim 5''$ in the B4 profile. The disky component can also be recognized in the velocity map (ATLAS^{3D}). The bar is fit with a Ferrer function and the inner disk with a low- n Sérsic profile. We do not model the nuclear component to avoid degeneracies.

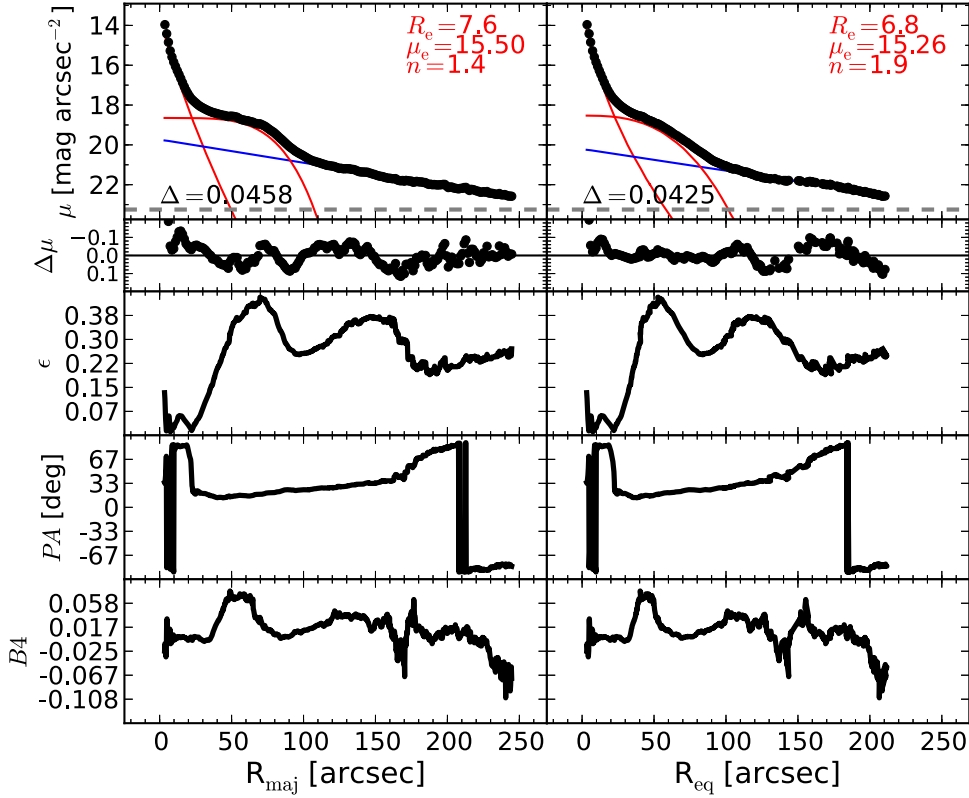


Figure 59. NGC 4151: a face-on barred spiral galaxy that hosts a Seyfert AGN (Véron-Cetty & Véron 2006) and circumnuclear dust (Pott et al. 2010). The nucleus of this galaxy is very bright, and the IRAF task `ellipse` fails at fitting the isophotes within $R_{\text{maj}} < 4''$; thus, our light profile starts at $R_{\text{maj}} \sim 4''$. The bar is fit with a low- n Sérsic profile.

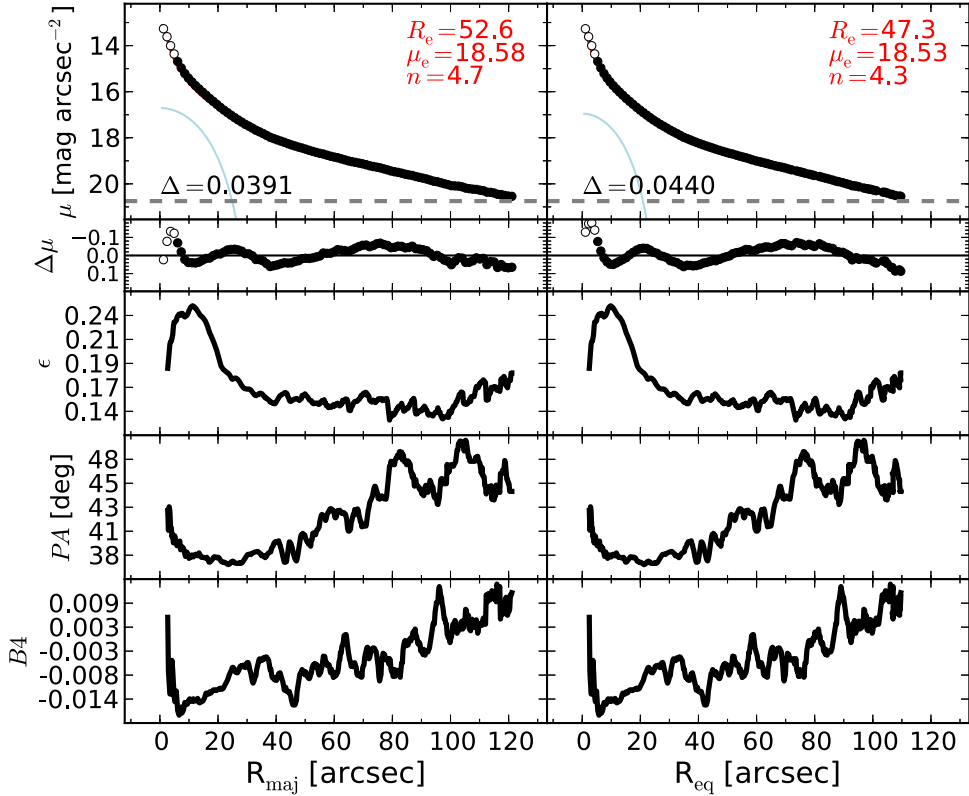


Figure 60. NGC 4261: an elliptical galaxy with a LINER nucleus (Véron-Cetty & Véron 2006) and a dusty nuclear disk (Tran et al. 2001). The galaxy features an unresolved partially depleted core (Rusli et al. 2013a). The ellipticity profile has a peak at $R_{\text{maj}} \sim 10''$, revealing the presence of an embedded component, which we model with a Ferrer function. The data within the innermost $6''$ are excluded from the fit.

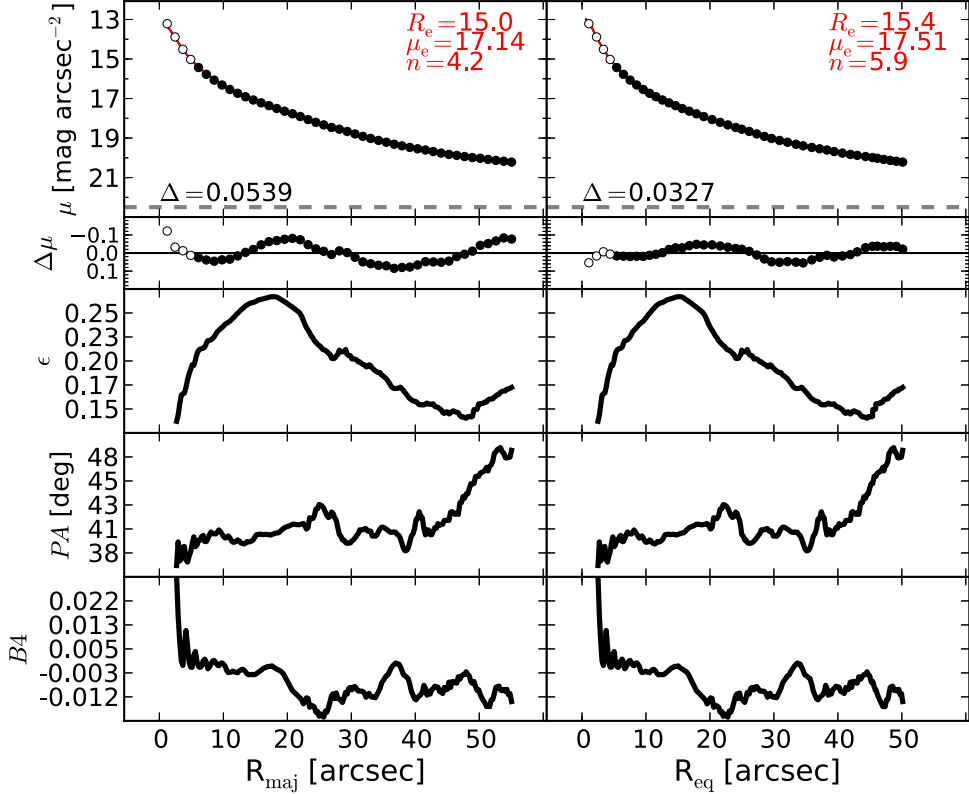


Figure 61. NGC 4291: an elliptical galaxy with an unresolved partially depleted core (Rusli et al. 2013a). After excluding the data within the innermost $6''$ from the fit, we observe that NGC 4291 can be reasonably well modeled with a Sérsic profile.

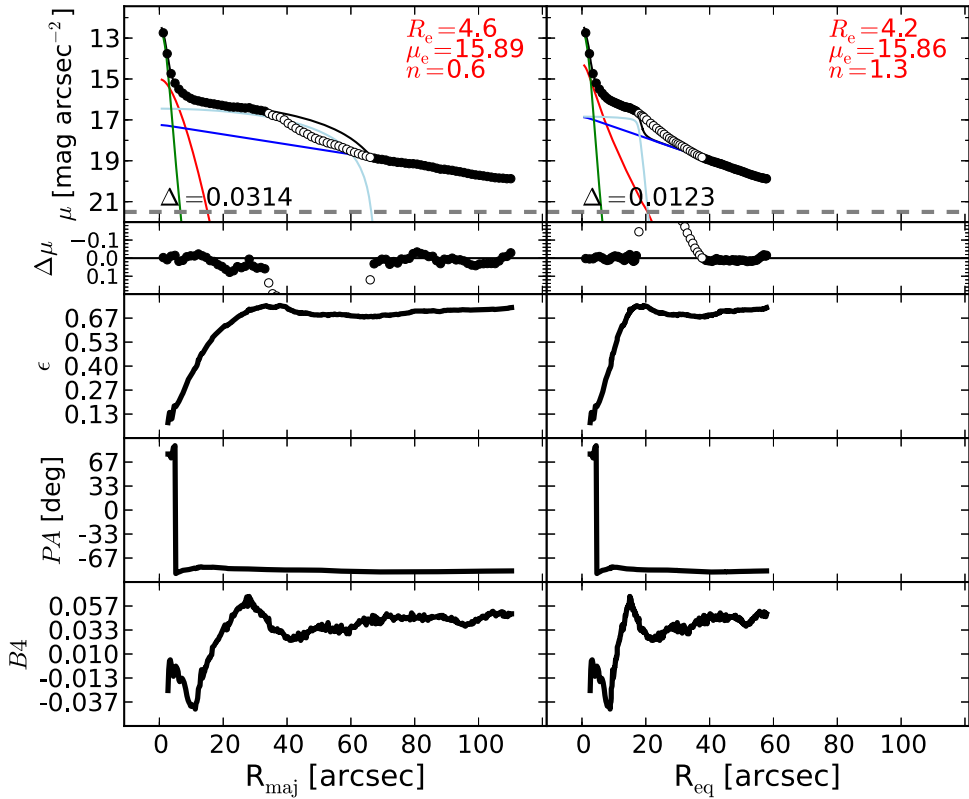


Figure 62. NGC 4388: an edge-on spiral galaxy with a Seyfert AGN (Véron-Cetty & Véron 2006) and copious nuclear dust (Martini et al. 2003). The peaks at $R_{\text{maj}} \sim 30''$ in the ellipticity and $B4$ profiles signal the presence of a bar. The data between $35'' \lesssim R_{\text{maj}} \lesssim 65''$ are excluded from the fit. The AGN component is fit with a Gaussian profile.

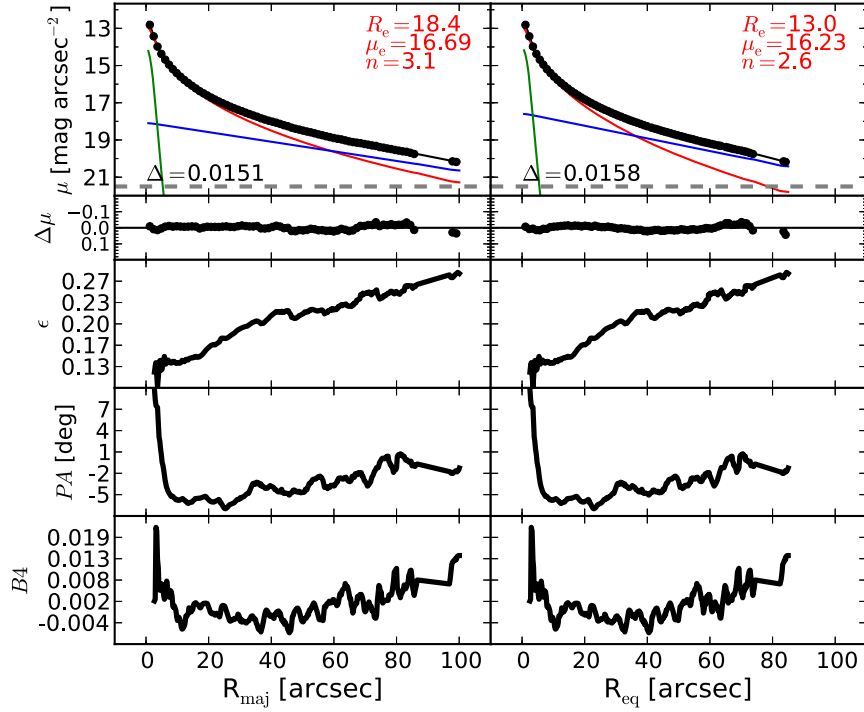


Figure 63. NGC 4459: a lenticular galaxy, whose disk profile has been reported to have an antitruncation at $R_{\text{maj}} \sim 119''$ (Gutiérrez et al. 2011). The ellipticity constantly increases across the entire observed radial range ($R_{\text{maj}} \lesssim 100''$). This is an indication that, going from the galaxy center to the outskirts, the disk component becomes increasingly more important over the spheroidal component. However, the lack of a plateau in the ellipticity profile at large radii implies that at $R_{\text{maj}} \sim 100''$ the contribution from the bulge is still significant compared to that of the disk. We note that the antitruncation reported by Gutiérrez et al. (2011) could be an artificial feature produced by the transition from the Sérsic bulge to the exponential disk. According to their analysis of the surface brightness profile of NGC 4459 (their Figure 14), the contribution from the disk completely overcomes that of the bulge beyond $R_{\text{maj}} \gtrsim 60''$. In the surface brightness profile, they identified two exponential declines with different scale lengths (the first between $60'' \lesssim R_{\text{maj}} \lesssim 110''$, and the second beyond $R_{\text{maj}} \gtrsim 120''$). However, we checked that in the radial range $60'' \lesssim R_{\text{maj}} \lesssim 110''$ the surface brightness profile is not a perfect exponential, but presents a curvature. This can be securely assessed only by fitting the data within the mentioned radial range with a single exponential function and plotting the residuals; if the residuals betray a curvature, the data cannot be accommodated by a single exponential function. According to our decomposition, the disk of NGC 4459 starts dominating beyond $R_{\text{maj}} \gtrsim 100''$. The exponential function of our model seems to nicely match the “second” exponential decline identified by Gutiérrez et al. (2011). We do not find evidence for any embedded components in our data. A nuclear light excess is modeled with a Gaussian profile.

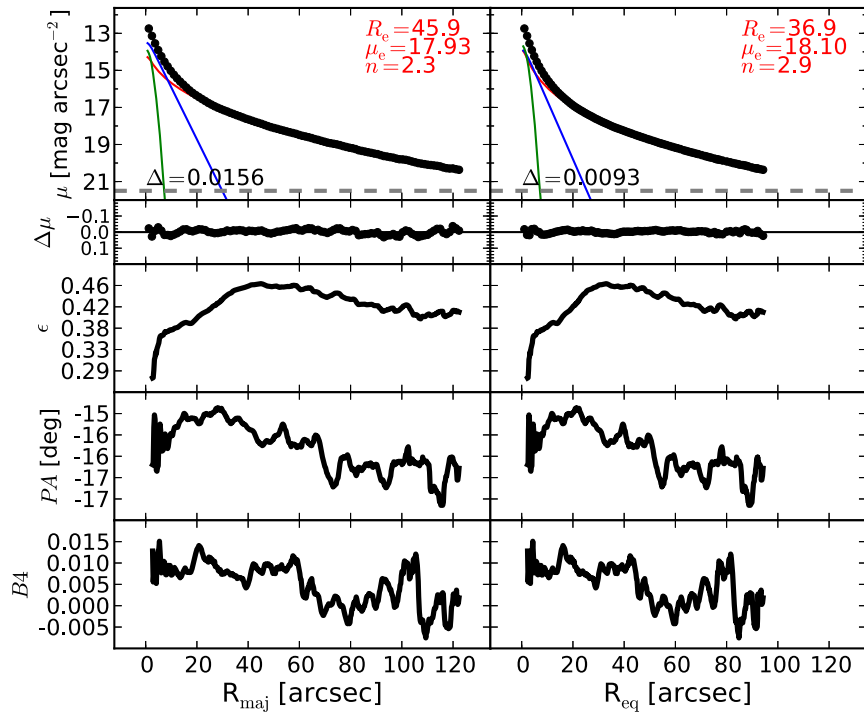


Figure 64. NGC 4473: an elliptical galaxy with an embedded disk (Ledo et al. 2010). The disk is clearly visible in the velocity map (ATLAS^{3D}, SLUGGS). We account for a nuclear excess of light by adding a narrow Gaussian function to the model.

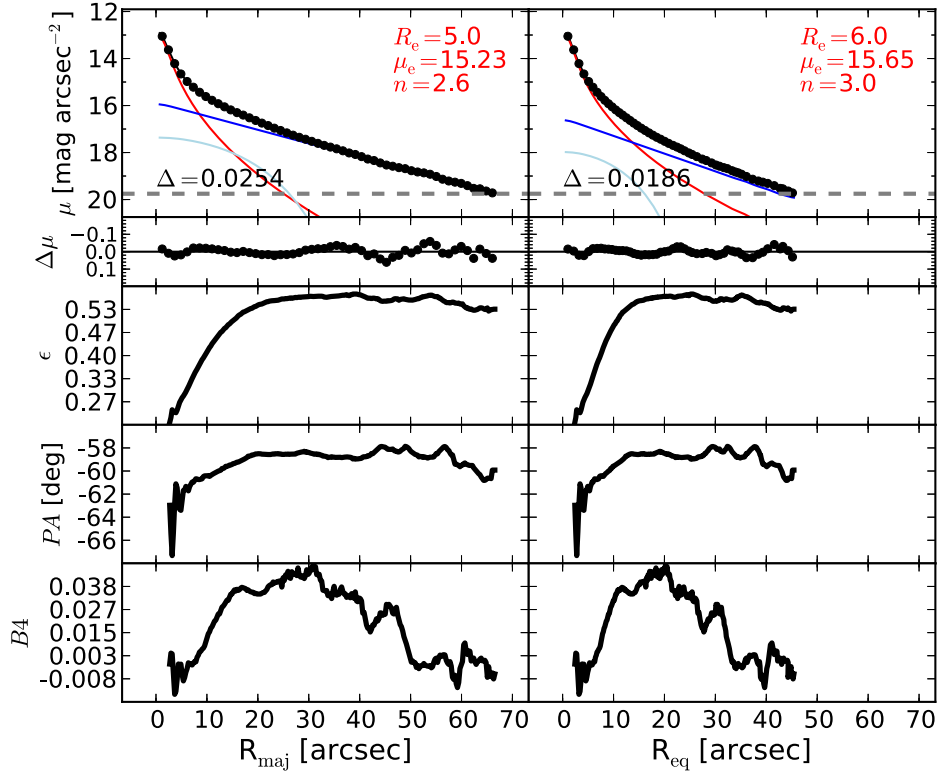


Figure 65. NGC 4564: an edge-on lenticular galaxy. In the unsharp mask, one can glimpse an oval structure extending out to $R_{\text{maj}} \lesssim 15''$ (see the peak in the $B4$ profile). Fitting NGC 4564 with a Sérsic + exponential model produces poor residuals. However, the addition of a Ferrer function to the model dramatically improves the fit and smoothes the residuals.

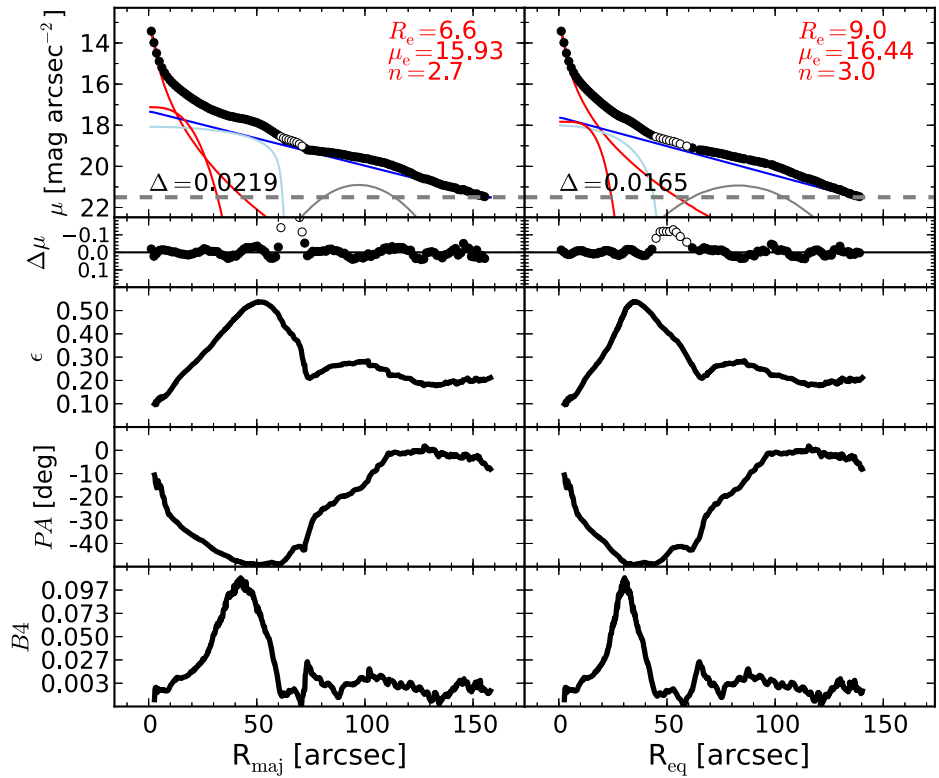


Figure 66. NGC 4596: an edge-on barred lenticular galaxy. The morphology of this galaxy is quite complex. The bar extends out to $R_{\text{maj}} \lesssim 50''$ and concludes in two evident ansae. The large-scale disk features a wide ring that is responsible for the curvature in the light profile observed within $60'' \lesssim R_{\text{maj}} \lesssim 130''$ (see also Comerón et al. 2014). An additional embedded disk component ($R_{\text{maj}} \lesssim 15''$) can be recognized in the $B4$ profile and in the velocity map. The bump in the light profile within $60'' \lesssim R_{\text{maj}} \lesssim 70''$ corresponds to the ansae of the bar, and this data range is therefore excluded from the fit. The large-scale bar is fit with a Ferrer function and the inner disk with a low- n Sérsic profile.

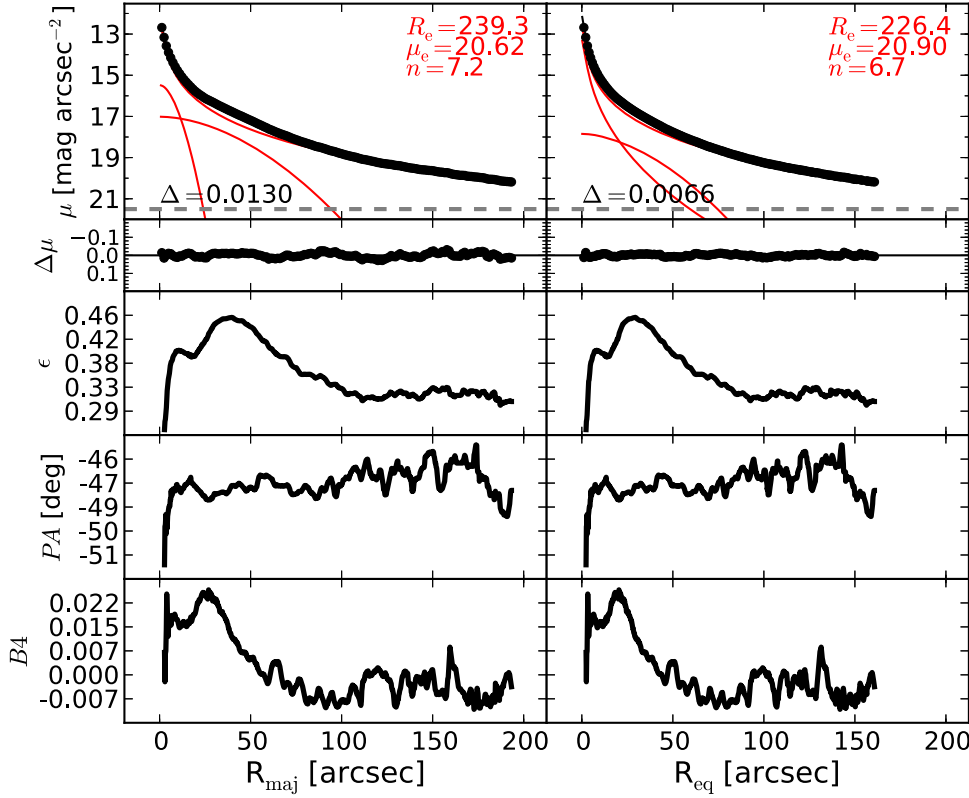


Figure 67. NGC 4697: an elliptical galaxy with an embedded disk (Scorza & Bender 1995). The velocity map (ATLAS^{3D}, SLUGGS) and the unsharp mask of NGC 4697 clearly show the presence of an intermediate-size disk embedded in the galaxy's spheroidal component. However, the ellipticity profile presents two peaks. The peak at $R_{\text{maj}} \sim 40''$ corresponds to the intermediate-size embedded disk just mentioned, while the peak at $R_{\text{maj}} \sim 10''$ pertains to a smaller inner disk. After testing different decomposition models, in which we fit the two embedded disks with different functions (exponential, Sérsic, Ferrer), while always describing the main spheroidal component with a Sérsic profile, we noticed that the spheroid parameters do not significantly vary among the various decompositions. Our preferred model for NGC 4697 consists of a Sérsic bulge + two Sérsic inner disks.

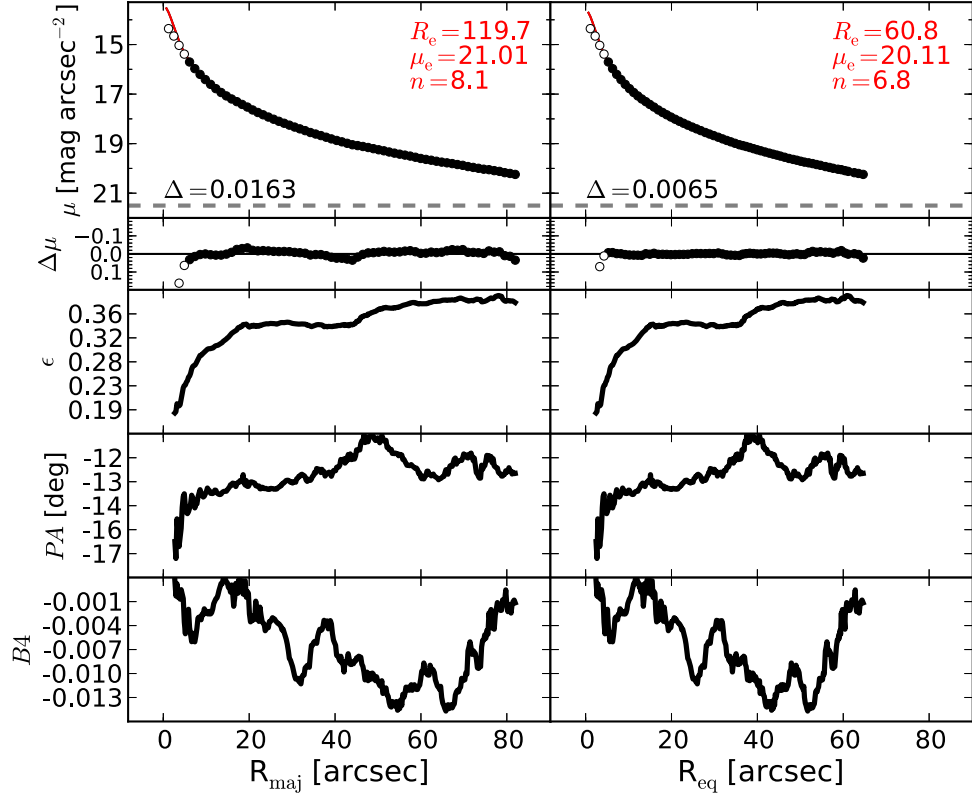


Figure 68. NGC 4889: the brightest member of the Coma Cluster, an elliptical galaxy with an unresolved partially depleted core (Rusli et al. 2013a). We exclude the innermost $6''$ from the fit and successfully model the galaxy with a single Sérsic profile.

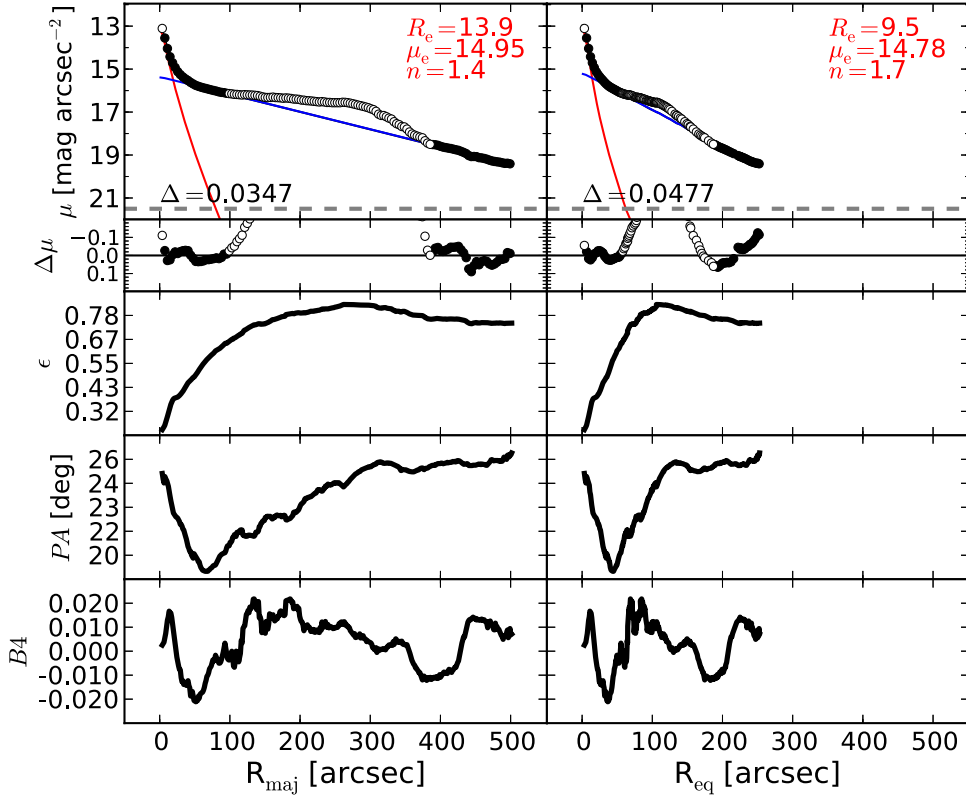


Figure 69. NGC 4945: an edge-on, dusty spiral galaxy that hosts a Seyfert AGN (Lin et al. 2011). The light profile has an obvious bump that can be ascribed to the bar. This bump cannot be easily modeled with a Ferrer function or with a Sérsic profile; thus, we exclude the data in the range $100'' \lesssim R_{\text{maj}} \sim 400''$ from the fit. We also exclude the data within the innermost $6''.4$ owing to the contribution from the AGN.

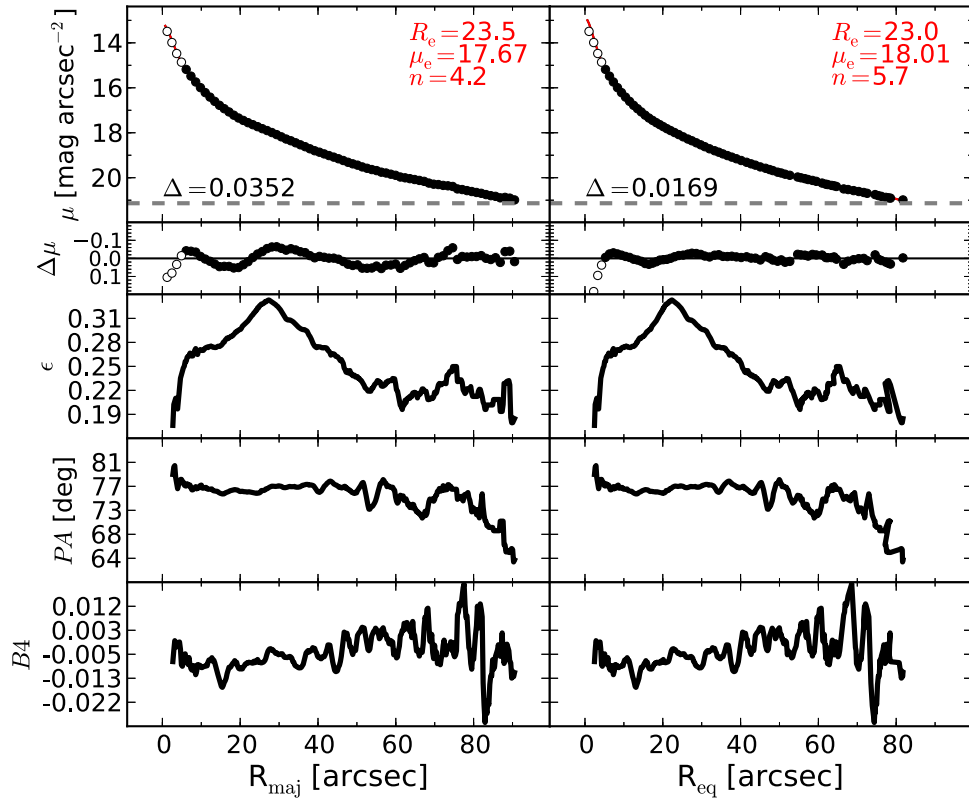


Figure 70. NGC 5077: an elliptical galaxy with an unresolved partially depleted core (Trujillo et al. 2004). We mask the data within the innermost $6''.1$ and fit the galaxy with a Sérsic profile.

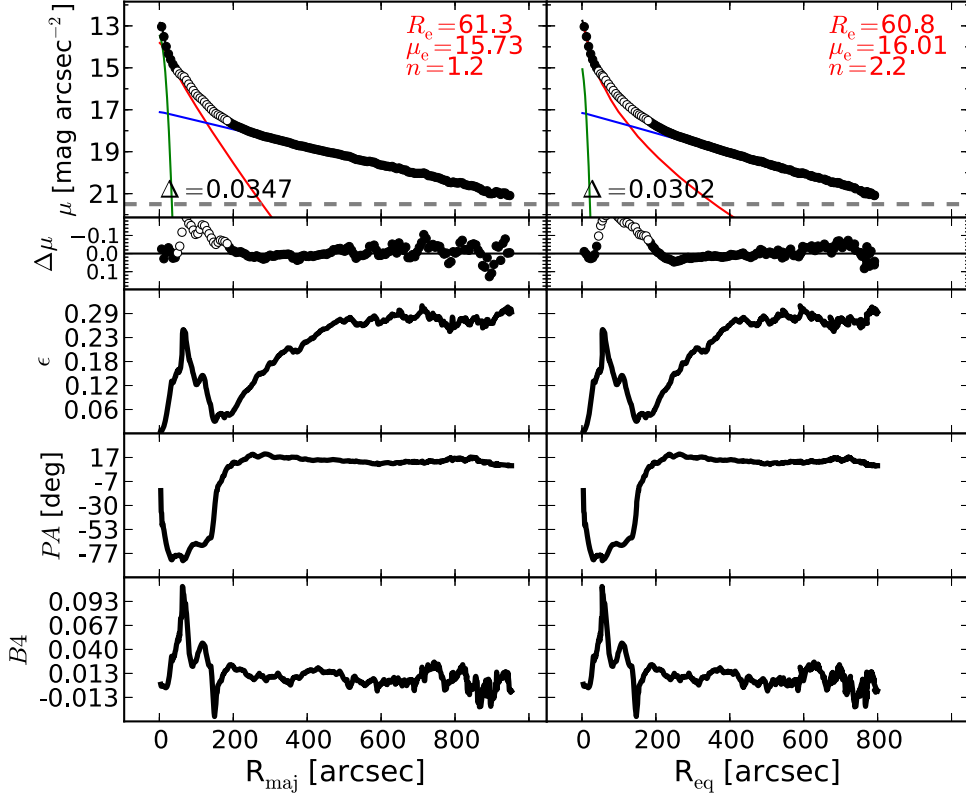


Figure 71. NGC 5128: a merging system. The data within $50'' \lesssim R_{\text{maj}} \lesssim 200''$ are excluded from the fit.

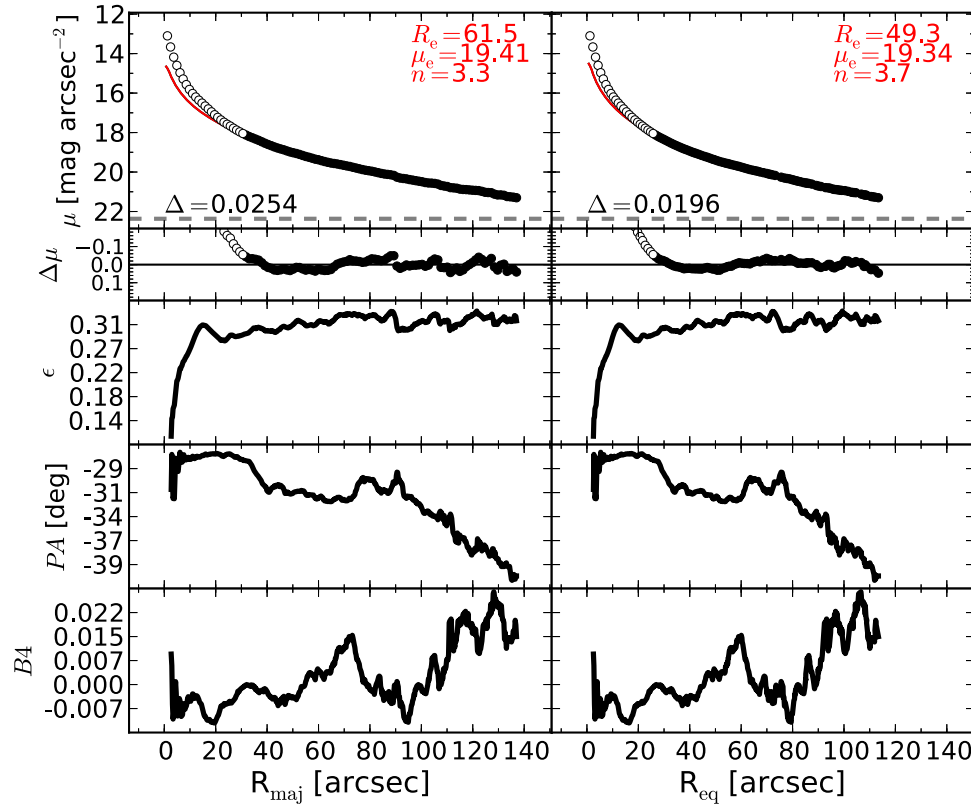


Figure 72. NGC 5576: an elliptical galaxy with a disturbed morphology. The isophotal parameters suggest the presence of an embedded disk ($R_{\text{maj}} \lesssim 20''$), but attempts to account for such a component were unsuccessful. The data within $R_{\text{maj}} \lesssim 36''$ are excluded from the fit, and the galaxy is modeled with a Sérsic profile.

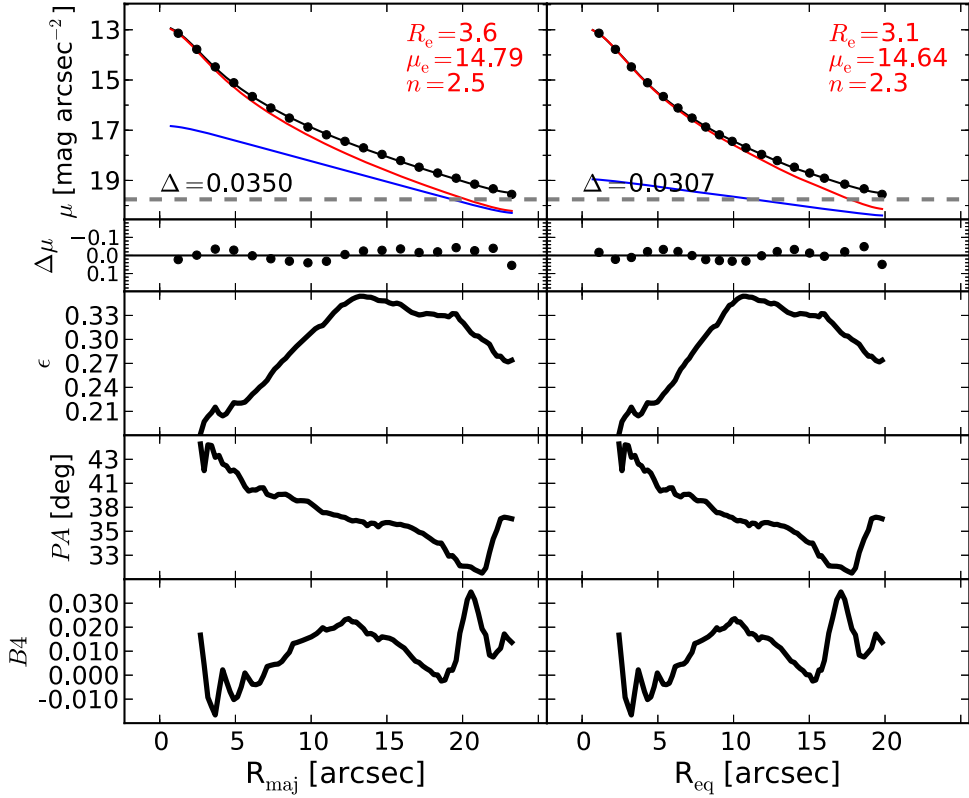


Figure 73. NGC 5845: **a** lenticular galaxy. From the unsharp mask and the velocity map (ATLAS^{3D}), we identify a disk, but it is not clear whether the disk is **large scale** or **intermediate scale**. The ellipticity profile has a peak at $R_{\text{maj}} \sim 13''$, which suggests that the disk is indeed **intermediate scale**, i.e., it does not dominate at large radii.

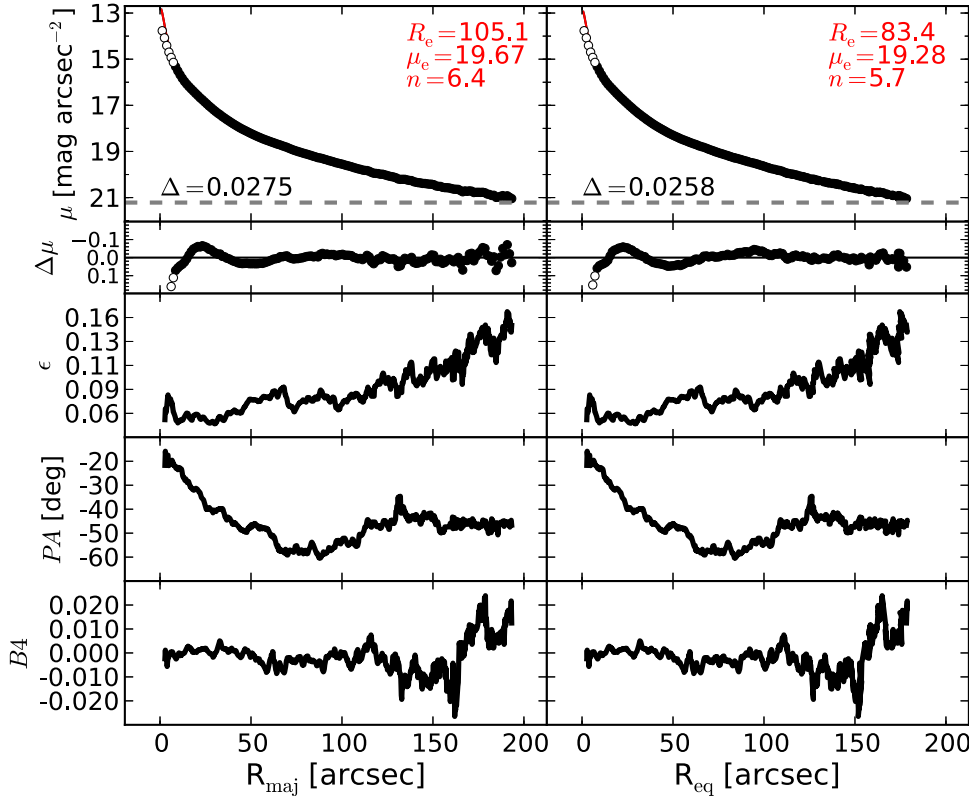


Figure 74. NGC 5846: **a**n elliptical galaxy with an unresolved partially depleted core (Rusli et al. 2013a). This galaxy has a LINER nucleus (Carrillo et al. 1999) and filamentary nuclear dust (Tran et al. 2001). It also displays a strong isophotal twist between its center and $R_{\text{maj}} \sim 70''$. The light profile presents a slight bump at $R_{\text{maj}} \sim 20''$. However, the isophotal parameters, the unsharp mask, and the velocity map (ATLAS^{3D}) lack clear evidence for an embedded component. We thus model NGC 5846 with a single Sérsic profile, after masking the data within the innermost $6''$.

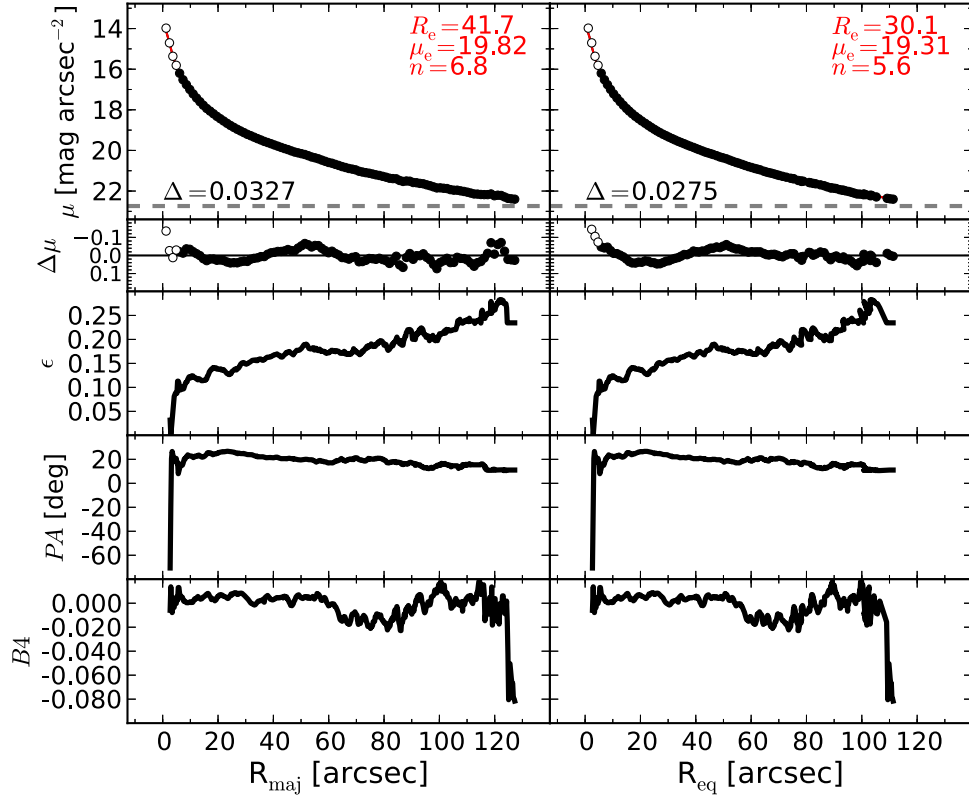


Figure 75. NGC 6251: an elliptical galaxy. Its large stellar velocity dispersion suggests the presence of a partially depleted core. The galaxy features a nuclear disk of dust (Ferrarese & Ford 1999) and a Seyfert AGN (Panessa & Bassani 2002). We mask the data within the innermost $6''$.1. A single Sérsic profile provides a good description of this galaxy.

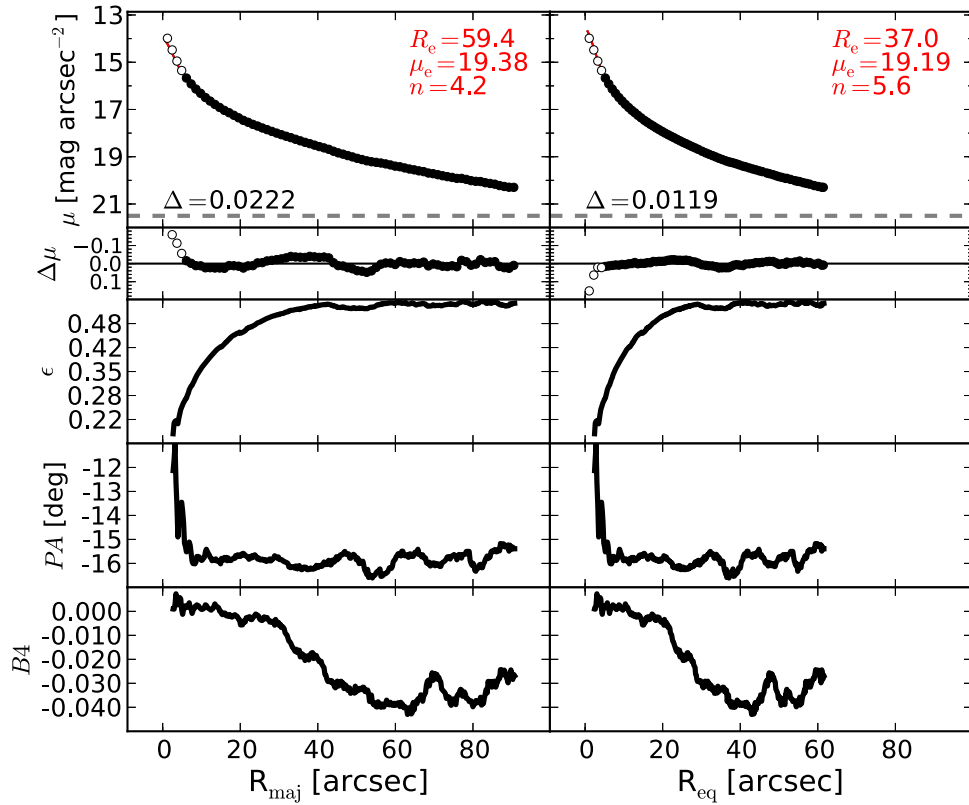


Figure 76. NGC 7052: an elliptical galaxy with an unresolved partially depleted core (Quillen et al. 2000). We mask the data within the innermost $6''$.1 and model the galaxy with a single Sérsic profile.

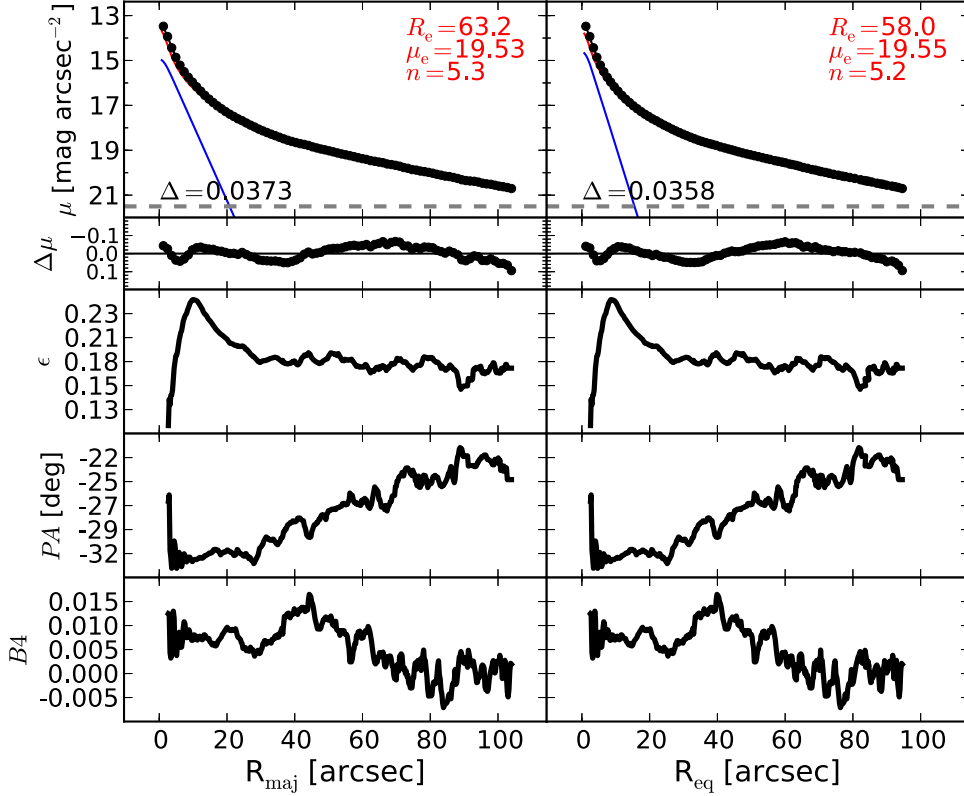


Figure 77. NGC 7619: an elliptical galaxy with an unresolved partially depleted core (Rusli et al. 2013a). We identified an embedded disk signaled by the peak at $R_{\text{maj}} \sim 10''$ in the ellipticity profile. The velocity map of this galaxy confirms the presence of a fast-rotating component (Falcon-Barroso 2015, private communication). We note that the residuals obtained from our bulge + inner-disk model do not suggest the presence of a partially depleted core.

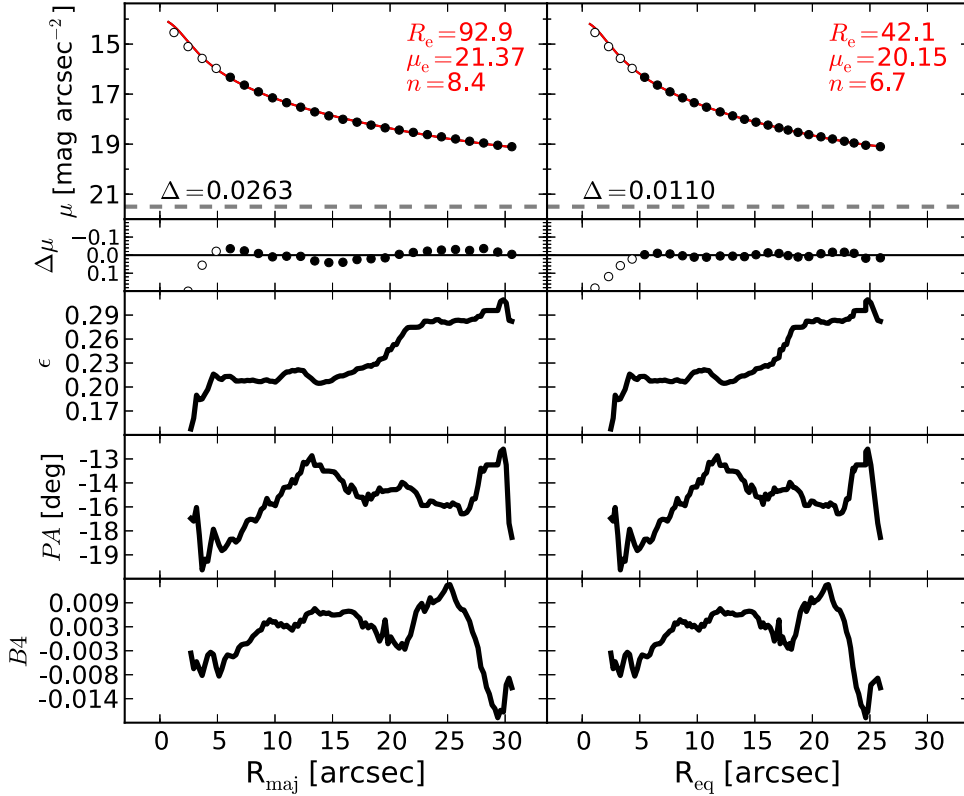


Figure 78. NGC 7768: an elliptical galaxy with an unresolved partially depleted core (Rusli et al. 2013a). The image of NGC 7768 is corrupted by a saturated star, which lies close to the galaxy. The sky background is not constant across the image. To be safe, we fit only the data within the innermost $R_{\text{maj}} \lesssim 30''$, where the contribution from the background is negligible. The data within $R_{\text{maj}} < 6.1''$ are excluded from the fit.

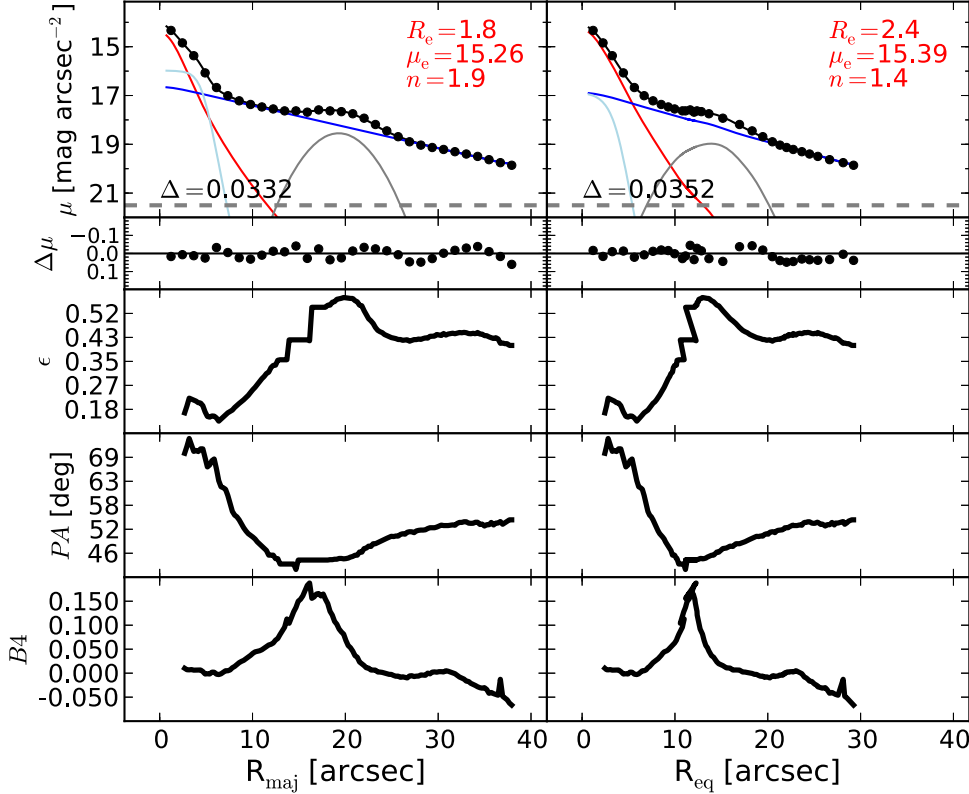


Figure 79. UGC 03789: a face-on spiral galaxy, featuring a ring ($R_{\text{maj}} \sim 20''$) and a nuclear bar ($R_{\text{maj}} \lesssim 4''$), which can be seen in the unsharp mask and produces corresponding peaks in the ellipticity and PA profiles. The bar is fit with a Ferrer function.

models implicitly include “m-n” or “m-c.” In the table caption, we comment on the most significant discrepancies between our results and those obtained by the other studies.

G.S. acknowledges the invaluable support received from Alessandro Marconi, Eleonora Sani, and Leslie Hunt in the early stages of this research. G.S. warmly thanks Chieng Peng, Peter Erwin, Luca Cortese, Giuseppe Gavazzi, Bililign Dullo, Paolo Bonfini, Elisabete Lima Da Cunha, and Gonzalo Diaz for useful discussion. We thank the anonymous referee for their thorough review and highly appreciate the comments and suggestions, which significantly contributed to improving the quality of the publication. This research was supported by Australian Research Council funding through grants DP110103509 and FT110100263. This work is based on observations made with the IRAC instrument (Fazio et al. 2004) on board the *Spitzer Space Telescope*, which is operated by the Jet Propulsion Laboratory, California Institute of Technology, under a contract with NASA. This research has made use of the GOLDMine database (Gavazzi et al. 2003) and the NASA/IPAC Extragalactic Database (NED), which is operated by the Jet Propulsion Laboratory, California Institute of Technology, under contract with the National Aeronautics and Space Administration.

APPENDIX 1D ANALYTICAL FUNCTIONS

Here we provide the mathematical expressions of the analytical functions used to model the observed surface brightness profiles, $\mu(R)$, of galaxies. The projected galactic

radius, R , corresponds to the distance of the isophotes from the galaxy center (along either the major or equivalent axis).

The Sérsic (1963, 1968) model is a three-parameter function of the following form:

$$\mu_{\text{Sérsic}}(\mu_e, R_e, n; R) = \mu_e + \frac{2.5 b_n}{\ln(10)} \left[\left(\frac{R}{R_e} \right)^{1/n} - 1 \right], \quad (5)$$

(Caon et al. 1993; Andredakis et al. 1995; Graham & Driver 2005), where μ_e is the surface brightness at the effective radius R_e that encloses half of the total light from the model. The Sérsic index n is the parameter that measures the curvature of the radial light profile, and b_n is a scalar value defined in terms of the Sérsic index n such that

$$\Gamma(2n) = 2\gamma(2n, b_n), \quad (6)$$

where Γ is the complete gamma function (Ciotti 1991) and γ is the incomplete gamma function defined by

$$\gamma(2n, x) = \int_0^x e^{-t} t^{2n-1} dt. \quad (7)$$

The exponential model is a special case ($n = 1$) of the Sérsic model. It can therefore be written as a two-parameter function such that

$$\mu_{\text{exponential}}(\mu_0, h; R) = \mu_0 + \frac{2.5}{\ln(10)} \left(\frac{R}{h} \right), \quad (8)$$

where μ_0 is the central surface brightness and h is the scale length equal to $R_e/1.678$.

The Gaussian model is another special case ($n = 0.5$) of the Sérsic model, and thus also a two-parameter function of the

following form:

$$\mu_{\text{Gaussian}}(\mu_0, \text{FWHM}; R) = \mu_0 + \frac{2.5}{\ln(10)} \left[\frac{R^2}{2(\text{FWHM}/2.355)^2} \right], \quad (9)$$

where μ_0 is the central surface brightness and FWHM is the full width at half-maximum of the Gaussian profile.

The Moffat (1969) model is a three-parameter function that can be expressed as

$$\mu_{\text{Moffat}}(\mu_0, \alpha, \beta; R) = \mu_0 - 2.5 \log \left[1 + \left(\frac{R}{\alpha} \right)^2 \right]^{-\beta}, \quad (10)$$

where μ_0 is the central surface brightness, α is related to the FWHM through

$$\text{FWHM} = 2\alpha\sqrt{2^{1/\beta} - 1}, \quad (11)$$

and β regulates the shape of the profile at large radii.

The Ferrer model is a four-parameter function defined as

$$\begin{aligned} \mu_{\text{Ferrer}}(\mu_0, R_{\text{out}}, \alpha, \beta; R) \\ = \begin{cases} \mu_0 - 2.5 \log \left[1 - \left(\frac{R}{R_{\text{out}}} \right)^{2-\beta} \right]^{\alpha} & \text{for } R < R_{\text{out}}, \\ +\infty & \text{for } R \geq R_{\text{out}} \end{cases} \end{aligned} \quad (12)$$

where μ_0 is the central surface brightness, α controls the sharpness of the truncation, β is related to the central slope, and R_{out} is the outer radial limit within which the function is defined.

The symmetric Gaussian ring is a three-parameter function of the following form:

$$\begin{aligned} \mu_{\text{Gaussian}}(\mu_0, R_0, \text{FWHM}; R) \\ = \mu_0 + \frac{2.5}{\ln(10)} \left[\frac{(R - R_0)^2}{2(\text{FWHM}/2.355)^2} \right], \end{aligned} \quad (13)$$

where μ_0 and FWHM have the same meaning as in Equation (9), and R_0 is the radius at which the Gaussian profile is centered.

Q4

REFERENCES

- Andredakis, Y. C., Peletier, R. F., & Balcells, M. 1995, *MNRAS*, 275, 874
 Arnold, J. A., Romanowsky, A. J., Brodie, J. P., et al. 2011, *ApJL*, 736, L26
 Arnold, J. A., Romanowsky, A. J., Brodie, J. P., et al. 2014, *ApJ*, 791, 80
 Athanassoula, E., & Beaton, R. L. 2006, *MNRAS*, 370, 1499
 Beaton, R. L., Majewski, S. R., Guhathakurta, P., et al. 2007, *ApJL*, 658, L91
 Beifiori, A., Courteau, S., Corsini, E. M., & Zhu, Y. 2012, *MNRAS*, 419, 2497
 Bender, R. 1990, *A&A*, 229, 441
 Caon, N., Capaccioli, M., & D'Onofrio, M. 1993, *MNRAS*, 265, 1013
 Capaccioli, M. 1987, in IAU Symp. 127, Structure and Dynamics of Elliptical Galaxies, ed. P. T. de Zeeuw, 47
 Cappellari, M., Emsellem, E., Krajnović, D., et al. 2011, *MNRAS*, 413, 813
 Cappellari, M., Verolme, E. K., van der Marel, R. P., et al. 2002, *ApJ*, 578, 787
 Carrillo, R., Masegosa, J., Dultzin-Hacyan, D., & Ordoñez, R. 1999, *RMxAA*, 35, 187
 Carter, D. 1987, *ApJ*, 312, 514
 Ciambur, B. C. 2015, arXiv:1507.02691
 Ciotti, L. 1991, *A&A*, 249, 99
 Comastri, A., Gilli, R., Marconi, A., Risaliti, G., & Salvati, M. 2015, arXiv:1501.03620
 Comerón, S., Elmegreen, B. G., Salo, H., et al. 2012, *ApJ*, 759, 98
 Comerón, S., Knapen, J. H., Beckman, J. E., et al. 2010, *MNRAS*, 402, 2462
 Comerón, S., Salo, H., Laurikainen, E., et al. 2014, *A&A*, 562, A121
 Contini, T., Consideré, S., & Davoust, E. 1998, *A&AS*, 130, 285
 de Vaucouleurs, G., de Vaucouleurs, A., Corwin, H. G., Jr., et al. 1991, Third Reference Catalogue of Bright Galaxies. Vol. I: Explanations and References. Vol. II: Data for Galaxies Between 0^h and 12^h. Vol. III: Data for Galaxies Between 12^h and 24^h
 Diaz, A. I., Prieto, M. A., & Wamsteker, W. 1988, *A&A*, 195, 53
 D'Onofrio, M., Zaggia, S. R., Longo, G., Caon, N., & Capaccioli, M. 1995, *A&A*, 296, 319
 Dressler, A. 1989, in IAU Symp. 134, Active Galactic Nuclei, ed. D. E. Osterbrock, & J. S. Miller, 217
 Dullo, B. T., & Graham, A. W. 2013, arXiv:1310.5867
 Dullo, B. T., & Graham, A. W. 2014, *MNRAS*, 444, 2700
 Elmegreen, B. G., & Elmegreen, D. M. 1985, *ApJ*, 288, 438
 Elmegreen, D. M., Chromey, F. R., & Johnson, C. O. 1995, *AJ*, 110, 2102
 Elmegreen, D. M., Elmegreen, B. G., & Eberwein, K. S. 2002, *ApJ*, 564, 234
 Emsellem, E., Cappellari, M., Krajnović, D., et al. 2011, *MNRAS*, 414, 888
 Erwin, P. 2004, *A&A*, 415, 941
 Erwin, P. 2015, *ApJ*, 799, 226
 Erwin, P., Beckman, J. E., & Pohlen, M. 2005, *ApJL*, 626, L81
 Erwin, P., Beltrán, J. C. V., Graham, A. W., & Beckman, J. E. 2003, *ApJ*, 597, 929
 Erwin, P., & Debattista, V. P. 2013, *MNRAS*, 431, 3060
 Erwin, P., & Gadotti, D. A. 2012, *AdAst*, 2012, 4
 Erwin, P., Gutiérrez, L., & Beckman, J. E. 2012, *ApJL*, 744, L11
 Erwin, P., Pohlen, M., & Beckman, J. E. 2008, *AJ*, 135, 20
 Erwin, P., & Sparke, L. S. 2003, *ApJS*, 146, 299
 Fazio, G. G., Hora, J. L., Allen, L. E., et al. 2004, *ApJS*, 154, 10
 Ferrarese, L., Côté, P., Jordán, A., et al. 2006, *ApJS*, 164, 334
 Ferrarese, L., & Ford, H. C. 1999, *ApJ*, 515, 583
 Ferrarese, L., & Merritt, D. 2000, *ApJL*, 539, L9
 Fisher, D. B., & Drory, N. 2010, *ApJ*, 716, 942
 Fontanot, F., Monaco, P., & Shankar, F. 2015, *MNRAS*, 453, 4112
 Forbes, D. A., Brodie, J. P., & Huchra, J. 1997, *AJ*, 113, 887
 Forbes, D. A., Franx, M., & Illingworth, G. D. 1994, *ApJL*, 428, L49
 Franx, M., & Illingworth, G. D. 1988, *ApJL*, 327, L55
 Gadotti, D. A. 2008, *MNRAS*, 384, 420
 Gadotti, D. A., & de Souza, R. E. 2006, *ApJS*, 163, 270
 Gadotti, D. A., & Sánchez-Janssen, R. 2012, *MNRAS*, 423, 877
 Gavazzi, G., Boselli, A., Donati, A., Franzetti, P., & Scodéglio, M. 2003, *A&A*, 400, 451
 Gebhardt, K., Bender, R., Bower, G., et al. 2000, *ApJL*, 539, L13
 Graham, A. W. 2015, arXiv:1501.02937
 Graham, A. W., Colless, M. M., Busarello, G., Zaggia, S., & Longo, G. 1998, *A&AS*, 133, 325
 Graham, A. W., & Driver, S. P. 2005, *PASA*, 22, 118
 Graham, A. W., & Driver, S. P. 2007a, *ApJ*, 655, 77
 Graham, A. W., & Driver, S. P. 2007b, *MNRAS*, 380, L15
 Graham, A. W., Driver, S. P., Allen, P. D., & Liske, J. 2007, *MNRAS*, 378, 198
 Graham, A. W., Dullo, B. T., & Savorgnan, G. A. D. 2015, *ApJ*, 804, 32
 Graham, A. W., Erwin, P., Caon, N., & Trujillo, I. 2001, *ApJL*, 563, L11
 Graham, A. W., Erwin, P., Trujillo, I., & Asensio Ramos, A. 2003, *AJ*, 125, 2951
 Graham, A. W., & Guzmán, R. 2003, *AJ*, 125, 2936
 Graham, A. W., & Scott, N. 2013, *ApJ*, 764, 151
 Graham, A. W., & Scott, N. 2015, *ApJ*, 798, 54
 Greenhill, L. J., Booth, R. S., Ellingsen, S. P., et al. 2003, *ApJ*, 590, 162
 Grillmair, C. J., Faber, S. M., Lauer, T. R., et al. 1994, *AJ*, 108, 102
 Gutiérrez, L., Erwin, P., Aladro, R., & Beckman, J. E. 2011, *AJ*, 142, 145
 Häring, N., & Rix, H.-W. 2004, *ApJL*, 604, L89
 Haynes, M. P., Giovanelli, R., Sälzer, J. J., et al. 1999, *AJ*, 117, 1668
 Jardel, J. R., Gebhardt, K., Shen, J., et al. 2011, *ApJ*, 739, 21
 Jedrzejewski, R. I. 1987, *MNRAS*, 226, 747
 Jun, H. D., & Im, M. 2008, *ApJL*, 678, L97
 Khachikian, E. Y., & Weedman, D. W. 1974, *ApJ*, 192, 581
 Kim, T., Gadotti, D. A., Sheth, K., et al. 2014, *ApJ*, 782, 64
 Kim, T., Sheth, K., Gadotti, D. A., et al. 2015, *ApJ*, 799, 99
 King, I. R., & Minkowski, R. 1966, *ApJ*, 143, 1002
 Knapp, G. R., Rupen, M. P., Fich, M., Harper, D. A., & Wynn-Williams, C. G. 1996, *A&A*, 315, L75
 Kormendy, J., & Gebhardt, K. 2001, in AIP Conf. Ser. 586, 20th Texas Symp. on Relativistic Astrophysics, ed. J. C. Wheeler, & H. Martel (Melville, NY: AIP), 363

- Kormendy, J., & Richstone, D. 1995, *ARA&A*, **33**, 581
- Krajnović, D., Alatalo, K., Blitz, L., et al. 2013, *MNRAS*, **432**, 1768
- Krajnović, D., Emsellem, E., Cappellari, M., et al. 2011, *MNRAS*, **414**, 2923
- Laor, A., Fiore, F., Elvis, M., Wilkes, B. J., & McDowell, J. C. 1997, *ApJ*, **477**, 93
- Läske, R., Ferrarese, L., & van de Ven, G. 2014a, *ApJ*, arXiv:1311.1530
- Läske, R., Ferrarese, L., van de Ven, G., & Shankar, F. 2014b, *ApJ*, arXiv:1311.1531
- Laurikainen, E., Salo, H., & Buta, R. 2005, *MNRAS*, **362**, 1319
- Laurikainen, E., Salo, H., Buta, R., Knapen, J. H., & Comerón, S. 2010, *MNRAS*, **405**, 1089
- Ledo, H. R., Sarzi, M., Dotti, M., Khochfar, S., & Morelli, L. 2010, *MNRAS*, **407**, 969
- Lin, L.-H., Taam, R. E., Yen, D. C. C., Muller, S., & Lim, J. 2011, *ApJ*, **731**, 15
- Magorrian, J., Tremaine, S., Richstone, D., et al. 1998, *AJ*, **115**, 2285
- Makovoz, D., & Marleau, F. R. 2005, *PASP*, **117**, 1113
- Marconi, A., & Hunt, L. K. 2003, *ApJL*, **589**, L21
- Martini, P., Regan, M. W., Mulchaey, J. S., & Pogge, R. W. 2003, *ApJS*, **146**, 353
- Moffat, A. F. J. 1969, *A&A*, **3**, 455
- Morrison, H., Caldwell, N., Schiavon, R. P., et al. 2011, *ApJL*, **726**, L9
- Muñoz-Mateos, J. C., Sheth, K., Gil de Paz, A., et al. 2013, *ApJ*, **771**, 59
- Munoz-Tunon, C., Prieto, M., Beckman, J., & Cepa, J. 1989, *Ap&SS*, **156**, 301
- Nieto, J.-L., Bender, R., Arnaud, J., & Surma, P. 1991, *A&A*, **244**, L25
- Nowak, N., Thomas, J., Erwin, P., et al. 2010, *MNRAS*, **403**, 646
- Panessa, F., & Bassani, L. 2002, *A&A*, **394**, 435
- Pastrav, B. A., Popescu, C. C., Tuffs, R. J., & Sansom, A. E. 2013a, *A&A*, **553**, A80
- Pastrav, B. A., Popescu, C. C., Tuffs, R. J., & Sansom, A. E. 2013b, *A&A*, **557**, A137
- Peeples, M. S., & Martini, P. 2006, *ApJ*, **652**, 1097
- Peng, C. Y., Ho, L. C., Impey, C. D., & Rix, H.-W. 2002, *AJ*, **124**, 266
- Peng, C. Y., Ho, L. C., Impey, C. D., & Rix, H.-W. 2010, *AJ*, **139**, 2097
- Pott, J.-U., Malkan, M. A., Elitzur, M., et al. 2010, *ApJ*, **715**, 736
- Quillen, A. C., Bower, G. A., & Stritzinger, M. 2000, *ApJS*, **128**, 85
- Ravindranath, S., Ho, L. C., Peng, C. Y., Filippenko, A. V., & Sargent, W. L. W. 2001, *AJ*, **122**, 653
- Richings, A. J., Uttley, P., & Körding, E. 2011, *MNRAS*, **415**, 2158
- Richstone, D., Ajhar, E. A., Bender, R., et al. 1998, *Natur*, **395**, A14
- Rix, H.-W., & White, S. D. M. 1990, *ApJ*, **362**, 52
- Rix, H.-W., & White, S. D. M. 1992, *MNRAS*, **254**, 389
- Rusli, S. P., Erwin, P., Saglia, R. P., et al. 2013a, *AJ*, **146**, 160
- Rusli, S. P., Thomas, J., Erwin, P., et al. 2011, *MNRAS*, **410**, 1223
- Rusli, S. P., Thomas, J., Saglia, R. P., et al. 2013b, *AJ*, **146**, 45
- Salucci, P., Szuszkiewicz, E., Monaco, P., & Danese, L. 1999, *MNRAS*, **307**, 637
- Sani, E., Marconi, A., Hunt, L. K., & Risaliti, G. 2011, *MNRAS*, **413**, 1479
- Savorgnan, G., Graham, A. W., Marconi, A., et al. 2013, *MNRAS*, **434**, 387
- Savorgnan, G. A. D., & Graham, A. W. 2015a, *MNRAS*, submitted
- Savorgnan, G. A. D., & Graham, A. W. 2015b, *MNRAS*, **446**, 2330
- Schaye, J., Crain, R. A., Bower, R. G., et al. 2015, *MNRAS*, **446**, 521
- Scorza, C., & Bender, R. 1990, *A&A*, **235**, 49
- Scorza, C., & Bender, R. 1995, *A&A*, **293**, 20
- Scott, N., Davies, R. L., Houghton, R. C. W., et al. 2014, *MNRAS*, **441**, 274
- Sérsic, J. L. 1963, BAAA, **6**, 41
- Sérsic, J. L. 1968, Atlas de *Galaxias Australes*
- Shankar, F. 2009, *NewAR*, **53**, 57
- Shankar, F. 2013, *CQGra*, **30**, 244001
- Sheth, K., Regan, M., Hinz, J. L., et al. 2010, *PASP*, **122**, 1397
- Simões Lopes, R. D., Storchi-Bergmann, T., de Fátima Saraiva, M., & Martini, P. 2007, *ApJ*, **655**, 718
- Tran, H. D., Tsvetanov, Z., Ford, H. C., et al. 2001, *AJ*, **121**, 2928
- Trujillo, I., Erwin, P., Asensio Ramos, A., & Graham, A. W. 2004, *AJ*, **127**, 1917
- Trujillo, I., Graham, A. W., & Caon, N. 2001, *MNRAS*, **326**, 869
- Véron-Cetty, M.-P., & Véron, P. 2006, *A&A*, **455**, 773
- Vika, M., Driver, S. P., Cameron, E., Kelvin, L., & Robotham, A. 2012, *MNRAS*, **419**, 2264
- Wadadekar, Y., Robbason, B., & Kembhavi, A. 1999, *AJ*, **117**, 1219
- Whitmore, B. C., Lucas, R. A., McElroy, D. B., et al. 1990, *AJ*, **100**, 1489
- Worley, G. 1994, *ApJS*, **95**, 107
- Yee, H. K. C. 1992, in *ASP Conf. Ser. 31*, Relationships between Active Galactic Nuclei and Starburst Galaxies, ed. A. V. Filippenko (San Francisco, CA: ASP), 417

Q6

QUERY FORM

JOURNAL: The Astrophysical Journal Supplement Series

AUTHOR: Savorgnan & Graham

TITLE: SUPERMASSIVE BLACK HOLES AND THEIR HOST SPHEROIDS. I. DISASSEMBLING GALAXIES

ARTICLE ID: apjs522040

The layout of this article has not yet been finalized. This proof may contain columns that are not fully balanced/matched or other typographical imperfections; these issues will be resolved once the final corrections have been incorporated.

Page 29

Q1

Please cite Tables 4–69 in text (in numerical order).

Page 30

Q2

Please cite Figures 14–79 in text (in numerical order).

Page 55

Q3

Please provide the initials for the author [Falcon-Barroso] in reference [Falcon-Barroso 2015, private communication].

Page 57

Q4

Please check the details for any journal references that do not have a pale purple link (CrossRef doi) or a blue link (NASA ADS or arXiv e-print) in the two-column proof (article-style layout). A journal reference with no links may contain some incorrect information.

Page 57

Q5

Please provide the publisher details in references [Capaccioli 1987, de Vaucouleurs et al. 1991, Dressler 1989, Sérsic 1968].

Page 58

Q6

Please provide the publication to where reference [Savorgnan & Graham 2015a] has been submitted. Please also update, if possible.
